The Energy Spectrum of Very High Energy Gamma Rays from the Crab Nebula as Measured by the H.E.S.S. Array

DISSERTATION

zur Erlangung des akademischen Grades
doctor rerum naturalium
(Dr. rer. nat.)
im Fach Physik

eingereicht an der
Mathematisch-Naturwissenschaftlichen Fakultät I
Humboldt-Universität zu Berlin

von
Frau M.Sc. Tülün Ergin
geboren am 29.04.1975 in Wuppertal

Präsident der Humboldt-Universität zu Berlin:
Prof. Dr. Dr. Jürgen Mlynek

Dekan der Mathematisch-Naturwissenschaftlichen Fakultät I:
Prof. Dr. Thomas Buckhout

Gutachter:

1. Prof. Dr. Thomas Lohse
2. Priv.-Doz. Dr. Nikolaj Pavel
3. Prof. Dr. Stefan Wagner

eingereicht am: 1 Dezember 2004
Tag der mündlichen Prüfung: 3 März 2005

Abstract

The goal of this thesis is to implement the methods developed for the HEGRA experiment to reconstruct the geometry and energy of the airshowers induced by the cosmic high-energy gamma rays into the software environment of the H.E.S.S. experiment. Furthermore, using the implemented algorithms, a search for the unpulsed emission is aimed in the energy range between 300 GeV and 20 TeV from the Crab Nebula using the first stereoscopic data taken during October and November 2003 with the 3 telescope configuration of the H.E.S.S. array in Phase-I. The Phase-I of the H.E.S.S. array was completed in December 2003 by the addition of the fourth telescope.

By testing the reconstruction algorithms of a complete Phase-I H.E.S.S. array with Monte Carlo simulations, it is found that the resolution of the reconstructed direction and energy of a γ-ray event from a zenith angle of $45°$ is around $0.15°$ and 14%, respectively.

The data on the Crab Nebula including runs with wobble offset of $\pm0.5°$ and $\pm1.0°$ is collected at zenith angles from $45°$ to $50°$ for a total of 4 hours and gives a background subtracted signal of about 50 standard deviations. The differential energy spectrum of the unpulsed γ-ray emission from the Crab Nebula is found to be $d\Phi/dE = (3.37 \pm 0.47) \times 10^{-11} \ E^{-2.59\pm0.12} \ \mathrm{cm}^{-2}$ $\mathrm{s}^{-1}\mathrm{TeV}^{-1}$ between 450 GeV and 20 TeV after all cuts. The integral flux above 1 TeV is $(2.11 \pm 0.29) \times 10^{-11}\mathrm{cm}^{-2}\mathrm{s}^{-1}$. These results are consistent with the results published by other experiments, in particular HEGRA and Whipple. The results agree well with the expectation from synchrotron self-Compton models for TeV emission range. The magnetic field in the region, where TeV γ rays are produced, is found to be 0.18 ± 0.01 mG. This result agrees with the magnetic field values deduced by the models. The results obtained for the Crab Nebula in this thesis demonstrate the performance of the H.E.S.S. array.

Zusammenfassung

Das Thema dieser Arbeit ist die für das HEGRA Experiment entwickelte Rekonstruktions-Algoritmen, die Geometry und Energie von hochenergetischen kosmischen Gamma-Strahlen zu rekonstruieren, in die H.E.S.S. software Umgebung zu implementieren und das nicht-gepulste Energie-Spektrum des Krebsnebels zwischen Energien von 300 GeV und 20 TeV zu bestimmen. Dafür wurden die ersten stereoskopischen Daten von Oktober und November 2003 mit einer 3 Teleskope-Konfiguration des H.E.S.S. Systems der Phase-I verwendet. Die Phase-I des H.E.S.S. Systems wurde im Dezember 2003 fertiggestellt, nachdem das vierte Teleskop in Betrieb genommen wurde.

Die Rekonstruktionsalgorithmen wurden mit Monte Carlo Simulationen für die vollständige Phase-I des Teleskop-Systems getestet. Die Auflösung für die rekonstruierte Richtung und Energie der einzelnen γ-Ereignisse sind $0.15°$ und 14% bei 45° Zenitwinkel.

Die Daten des Krebsnebels, die eine Wobble-Versetzung von $\pm 0.5°$ and $\pm 1.0°$ haben und die im Zenitwinkel-Bereich von 45° bis 50° für 4 Stunden beobachtet wurden, geben ein Signal von 50 Standardabweichungen. Das differentielle Energiespektrum des Krebsnebels zwischen 450 GeV und 20 TeV nach den Schnitten ist $d\Phi/dE = (3.37 \pm 0.47) \times 10^{-11}\ E^{-2.59\pm0.12}$ cm^{-2}s^{-1} TeV^{-1}. Der integrierte Fluss oberhalb 1 TeV ist $(2.11 \pm 0.29) \times 10^{-11}$ cm^{-2}s^{-1}. Diese Resultate sind konsistent mit Messungen anderer Experimente, speziell von HEGRA und Whipple. Die Resultate stimmen mit den Erwartungen der *synchroton self-Compton* Modelle für den TeV Emissionbereich überein. Das magnetische Feld in der Region, wo die TeV γ-Strahlen vermutlich entstehen, wird zu 0.18±0.01 mG bestimmt. Die Resultate dieser Arbeit zeigen die Leistungsfähigkeit des H.E.S.S. Teleskop-Systems.

Inhaltsverzeichnis

Abbildungsverzeichnis

Tabellenverzeichnis

Introduction

In recent two decades very high energy (VHE) gamma(γ)-ray astronomy, which utilizes ground-based Cherenkov detectors, has contributed substantially to our understanding of high energetic processes of the non-thermal Universe. A firm detection of TeV photons from a number of galactic and extragalactic sources has enabled detailed studies of intrinsic features of various astrophysical objects.

Research results described in this thesis are mainly associated with the observations of the Crab Nebula and in particular the determination of the energy spectrum of γ-ray emission above 300 GeV from this object derived from the stereoscopic data taken with three of four imaging atmospheric Cherenkov telescopes (IACT) of the High Energy Stereoscopic System - H.E.S.S..

Chapter 1 gives an overall description of cosmic rays and continues to describe γ-ray astronomy. At present there are several models explaining the production of the high-energy γ rays in supernova remnants (SNRs) like the Crab Nebula. In Chapter 2 most plausible mechanisms of the production of high-energy γ rays in SNRs are summarized. In Chapter 3 the development of extensive atmospheric showers induced by charged cosmic and γ rays is reviewed and in addition the current detection technique is explained. This is followed by a detailed description of the H.E.S.S. experiment (Chapter 4). The Monte Carlo simulations, which are used in the evaluation of the γ-ray energy spectrum of the Crab Nebula, are briefly summarized in Chapter 5. The introduction to the stereoscopic analysis with the system of Cherenkov telescopes of H.E.S.S. is also given in Chapter 5. Results on the γ-ray energy spectrum of the Crab Nebula above 300 GeV as well as its comparison with other measurements and theoretical expectations are presented in Chapter 6. At the end basic conclusions out of present studies are summarized.

In the following section a brief review on the current status of ongoing research in physics of cosmic rays and ground-based astronomy of very high energy γ rays is given.

Kapitel 1

Cosmic Rays and Gamma-ray Astronomy

1.1 The Non-thermal Universe

The Universe is filled with blackbody radiation, which is generated in hot objects such as stars, hot gases and galaxies with temperatures in a range between 3000 and 10000 K [119]. Under extreme conditions (i.e. extremely high temperatures), thermal radiation can reach even into the keV energy range and beyond. However, some processes like localized matter outflows etc. in the Universe exhibit energy distributions that have no characteristic scale attributable to a temperature. This means that this component is determined by non-thermal, collective processes rather than by two-body interactions. In fact non-thermal processes are present in all regions of the Universe except in the dense interiors of stars and planets [4].

The collective acceleration mechanisms for particles of TeV energies and beyond are subject of theoretical work. The present and future observations aim to identify those sources of acceleration mechanisms in the Universe. Thus the primary rationale of observations with H.E.S.S. the array is the further understanding of the acceleration, propagation and interactions of such non-thermal particles.

The best-known example of a non-thermal particle population is cosmic rays. Their spectrum shows no indication of a characteristic (temperature) scale and their energies - up to 10^{20} eV and above - are well beyond the capabilities of any conceivable thermal emission mechanism.

1.2 Cosmic Rays

In 1912 Victor Francis Hess discovered through manned balloon ascents that radiation of very high penetration power was entering the atmosphere [86], which were named by Millikan as *cosmic rays*. Bothe and Kolhörster showed that the cosmic rays contain charged particles [35]. These cosmic rays have named as the secondary cosmic rays, which propagate from the production sites to the Earth and throughout their way to the Earth decay or interact with other cosmic rays. The primary cosmic rays are the cosmic rays at the production site.

Most of the cosmic rays observed at the Earth's surface are secondary or higher products, which are the so-called secondary particles, of very high energy secondary cosmic rays impinging on the atmosphere. In 1938 Pierre Auger found that the radiation (secondary particles) reaching the ground was correlated over large distances over 300 meters at short timescales like $1\mu s$ [13]. This was the discovery of extensive air showers, which are discussed in Chapter 3.1 in detail.

The cosmic ray (CR) spectrum spans roughly 11 decades of energy (see Figure 1.1). Sophisticated equipment on high altitude balloons and installations on the Earth's surface encompass a flux that goes down from 10^4 m^{-2}s^{-1} at $\sim 10^9$ eV to 10^{-2} km^{-2}yr^{-1} at $\sim 10^{20}$ eV. Its shape is remarkably featureless with little deviation from a constant power-law across this large energy range. The small change in slope from $\propto E^{-2.7}$ to $\propto E^{-3.0}$ near $10^{15.5}$ eV is known as the "knee". The spectrum steepens further to $E^{-3.3}$ above the "dipät $\sim 10^{17.7}$ eV and then flattens to $E^{-2.7}$ at the änkle", which is at $\sim 10^{19}$ eV. The statistical uncertainty of the current observations above 10^{20} eV is so large that no direct conclusion on the upper end of spectrum can be drawn [131].

The chemical composition of cosmic rays may substantially change through such a broad energy range of secondary cosmic rays and it is, in fact, not yet well-established. Below the knee it consists basically of 87% protons, 12% Helium, and 1% heavier elements up to iron [170]. The measured energy spectra of the individual hadronic components of cosmic rays obey the power-law in energy

$$dN(E)/dE \propto (E/1 \; TeV)^{-\alpha} \; \mathrm{m}^{-2} \; \mathrm{sec}^{-1} \; \mathrm{sr}^{-1} \; \mathrm{GeV}^{-1} \;\; ,$$

where α is the spectral index in the range of 2.5 - 2.8. The distribution of arrival directions of charged cosmic rays is supposedly isotropic. However, cosmic rays having energies equal or above 10^{20} eV may yield information on sources of their origin [28, 47]. Due to high rigidity the deflection of their trajectories propagating through the intergalactic and galactic magnetic fields can be
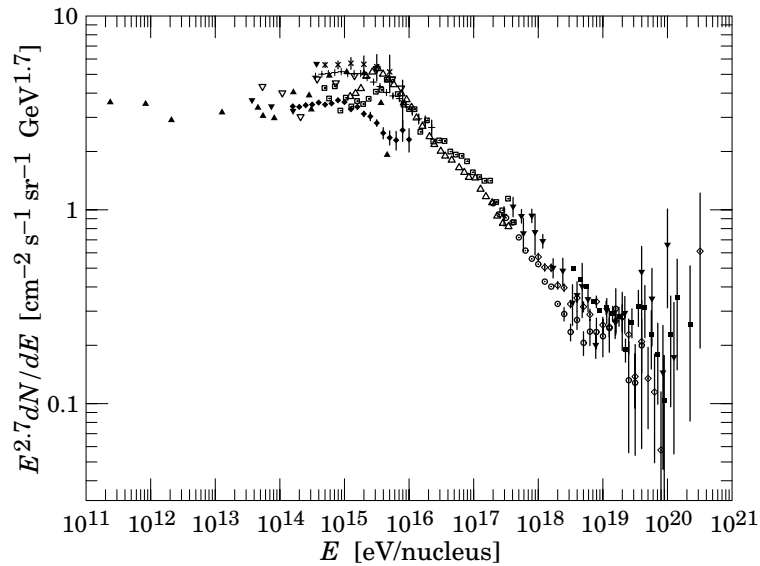
Abbildung 1.1: Energy spectrum of cosmic rays, multiplied by $E^{2.7}$ in order to magnify the *knee*-region.

neglected. The distribution of arrival directions is perhaps the most helpful observable in yielding clues about the CR origin. Studying the directional alignment of such ultra high energy cosmic rays (UHECR) with powerful compact objects one can be able to associate them with isolated sources in the sky. Furthermore, it is not expected that these rare cosmic rays may come from distances farther than 50 Mpc, because they are interacting with the 2.7 K cosmic microwave background radiation (CMBR), which limits their mean free path on their way to the Earth. Thus there should be a cutoff in the observed CR-spectrum. The production and acceleration mechanisms of these cosmic rays is one of the most exciting subjects of current astrophysics research.

Photons, neutrinos, electrons, positrons, and anti-nuclei, which make up a very small fraction of cosmic radiation, are all plausibly produced by interactions of the hadronic cosmic rays with the interstellar medium (ISM), but they may also be produced in discrete sources and accelerated in their environment [66].

1.3 Gamma-ray Astronomy

The charged hadronic cosmic rays with energy below 10^{17} eV are deflected by the magnetic field of our galaxy, which is approximately 2 μG, and

Tabelle 1.1: Nomenclature for γ-ray astronomy and cosmic rays, [95].

Energy Range [eV]	Classification	Detection
10^7 - $3 \cdot 10^7$	medium	space-based
$3 \cdot 10^7$ - $3 \cdot 10^{10}$	high (HE)	space-based
$3 \cdot 10^{10}$ - $3 \cdot 10^{13}$	very high (VHE)	ground-based
$3 \cdot 10^{13}$ - $3 \cdot 10^{16}$	ultra high (UHE)	ground-based
$3 \cdot 10^{16}$ - and up	extremely high (EHE)	ground-based

consequently the initial information on the source direction is lost. On the other hand, primary or secondary cosmic γ rays produced in hadronic or electromagnetic processes may arrive at the Earth without any disturbances. Therefore, the detection of the cosmic γ rays can give information about their production site. This was first mentioned by P. Morrison in 1958 ([129]). After the detection of Cherenkov radiation from cosmic rays (see Section 3.2) in 1959 G. Cocconi ([46]) predicted the detection of VHE γ rays for telescopes consisting of arrays of particle detectors.

The detection of γ rays started before the concept of *γ-ray astronomy* was raised, because the interaction cross sections of γ rays were large and the detection of the dominant interaction of γ rays with matter (i.e. the pair-production interaction) above a few MeV was easily recognizable, [167]. In 60's first attempts to measure the HE cosmic γ rays were made by balloon experiments. However, the sensitivity of these measurements were low due to the large background of charged cosmic rays. The detection of the Crab pulsar was the first firm detection, which motivated the development of new techniques. The extension of dynamic energy range of space-born detectors for X-ray astronomy upward in early 70's enabled a detection of a number of discrete sources of 100-MeV photons. This advances are followed by the launch of two γ-ray satellites SAS-2 in 1972 and COS-B in 1975 (see Section 1.3.3).

Particle detector arrays measuring the secondary particles produced by VHE γ rays in the atmosphere are used in 60's to search for point-source anomalies in the cosmic ray arrival direction, which were not successful, because their energy thresholds were too high. The first detection of VHE γ rays came in 1989 after the development of detectors, which make use of the imaging atmospheric Cherenkov technique (see Sections 1.3.3). Table 1.1 shows the γ-ray nomenclature.

1.3.1 Various Classes of Gamma-ray Sources

Supernova Remnants

Supernova Remnants (SNRs) are expanding shells formed after violent explosions, called *supernovae*, of massive stars at the end of their life. Supernova explosions play an important role in acceleration of cosmic rays through shock waves. If SNRs are the actual sites of cosmic ray production, interaction between accelerated particles and the local interstellar matter must occur. The expected TeV γ-ray fluxes from SNR calculated in a model of diffusive shock acceleration and π°-production of secondary γ rays by charged CRs interacting with the local swept-up interstellar matter are sufficiently high to be detectable using conventional imaging atmospheric Cherenkov telescopes. A complete discussion on mechanisms of γ-ray production in SNRs is given in Chapter 2.

Pulsars

Pulsars are rotating neutron stars, which were first discovered at radio wavelengths [89]. A typical neutron star has a very strong magnetic field, a maximum mass of ~ 3 solar masses, and a radius of about 10 km. 30 years after the discovery, about 1500 sources are today on the list of detected radio pulsars.

There are two major classes of pulsars: single isolated pulsars and millisecond pulsars. It is generally believed that an isolated pulsar is formed after the core collapse of a massive star (> 8 solar masses) through a supernova explosion. The creation rate of such pulsars in the Galaxy is one every 100 years. So, their population is large in the Galaxy. Rotation periods of pulsars vary in a range from a few milliseconds up to a few seconds. The rotation period of all pulsars is gradually increasing which is consistent with their loss of rotation energy. Therefore, the younger pulsars have shorter periods, e.g. Crab pulsar has a period of 33 ms. The magnetic fields of old pulsars is around 10^{10} G and for younger pulsars it is about 10^{12} G.

The other fraction of the observed pulsars are the so-called millisecond pulsars, which have periods in the range of 1.5 and 25 ms and very low slow-down rates. Therefore, the previous relationship between the age of the pulsar since its formation by a supernova and the slow down rate is different. It is also observed that they have comparatively weaker magnetic fields ($\sim 10^8$) showing that they have passed the normal age span of activity of a pulsar. This pulsars are explained by a spin-up process of the millisecond pulsars by accretion of matter from a companion, which provides both thermal energy and angular momentum increasing the rotation speed. Consequently, All
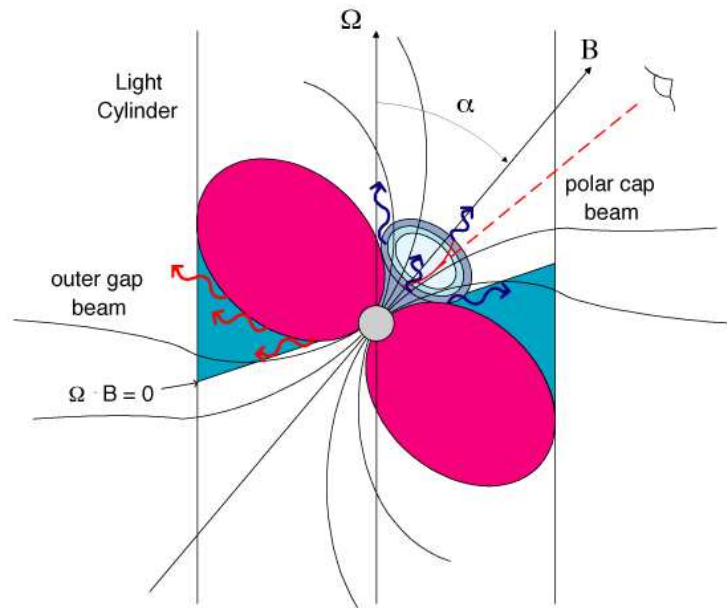
Abbildung 1.2: Sketch of the vicinity of a pulsar illustrating the polar cap and outer gap (blue regions), which are the basis γ-ray emission models.

millisecond pulsars have an orbiting companion. Presently, about 7% of all known pulsars are members of binary systems. The orbiting companions are usually white dwarfs (see Section 2.1.2), main sequence stars (see Section 2.1.2), or other neutron stars. Pulsed high energy γ-ray emission has been observed from seven pulsars with the EGRET space-born experiment (Section 1.3.3). The γ-ray emitting pulsars are all isolated pulsars, most of which are young pulsars.

There are two basic models, namely *the Polar Cap model* [157, 147] and *Outer Gap model* [43, 44, 144], which can partly explain the light curves and spectrum observed at GeV energies. The so-called *polar cap* is the region above the neutron star, which embraces the magnetic field lines (Figure 1.2). In this region the electrons (and positrons) are continuously pulled out from the surface and accelerated along the magnetic field lines. Some of those electrons produce photons by curvature radiation. These photons give rise to pair-production cascades, which can be seen at radio and X-ray wavelengths as well as in the γ-ray domain. *Outer gaps* are vacuum gaps that occur between the open field lines and the null charge surface of the charge separated magnetosphere (Figure 1.2). These gaps are places, where particles may radiate γ rays at TeV energies by inverse Compton scattering (see Section 2.2.2) or curvature radiation (see Section 2.2.1).

Active Galactic Nuclei

The nuclei of galaxies that totally outshines the rest of the galaxy by a factor of 1000 are called Active Galactic Nuclei (AGN). About 3% of all galaxies have active nuclei inside. From the observational point of view, there are several different types of AGN. These AGN types were selected according to the behavior observed in the IR, radio, X-ray, and γ-ray wavelength bands. However, this variety of multi-frequency spectra of AGN can be well described by a *unified AGN model* [18, 163]. Figure 1.3 illustrates schematically our current general view of the AGN environment. The central engine of an AGN is a super massive black hole of $M_{BH} \approx 10^7 - 10^{10}$ solar masses. There is an accretion disc around the black hole surrounded by a torus, which consists of dust lying in the equatorial plane of the black hole. There exist also two well collimated jets, which coincide with the major axis of the torus. The plasma flowing out with relativistic speed, and radiation emitted inside reaches the observer with a Doppler shift. The variety of AGN can be explained with the *unified model* by an apparent difference in the choice of basic parameters of the model, i.e. mass and spin of the torus, type of host galaxy, the accretion rate of matter into the nucleus, and the orientation of the axis of AGN with respect to our line of sight. If the jet of an AGN directly points to the observer, the object is called a *blazar*. Fewer than 1% of all AGN are blazars and a subset of these are BL Lacs (BL Lacertae). Those strongly variable sources have very faint, often vanishing, emission spectrum with a number of broad lines in it. Almost all of the established extragalactic sources that have been detected at VHE γ rays appear to be BL Lacs.

There are two major models proposed to explain a mechanism of VHE γ-ray production in the AGN jets: first the so-called *inverse Compton model* (ICM) [141] and secondly the *proton-initiated cascade model* (PIC) [140, 122]. The details on processes of γ-ray production are explained in Chapter 2, so these models are only briefly summarized here.

In the ICM, electrons are accelerated in the jets and scatter low energy target photons up to very high energies. This model is further classified depending on the place of acceleration in the jet (inhomogeneous models), or the type of the target photon in the source synchrotron self-Compton scattering (SSC) or external Compton scattering (EC). For the SSC model, the target photons are generated by the electrons themselves through synchrotron radiation, whereas in EC models the low energy photons come from outside the jet. In the PIC model protons are accelerated at the shock up to energies of 10^{19} eV. These protons interact with the ambient photon field, producing pions, which in turn decay into γ-quanta, which induce electromagnetic cascades.
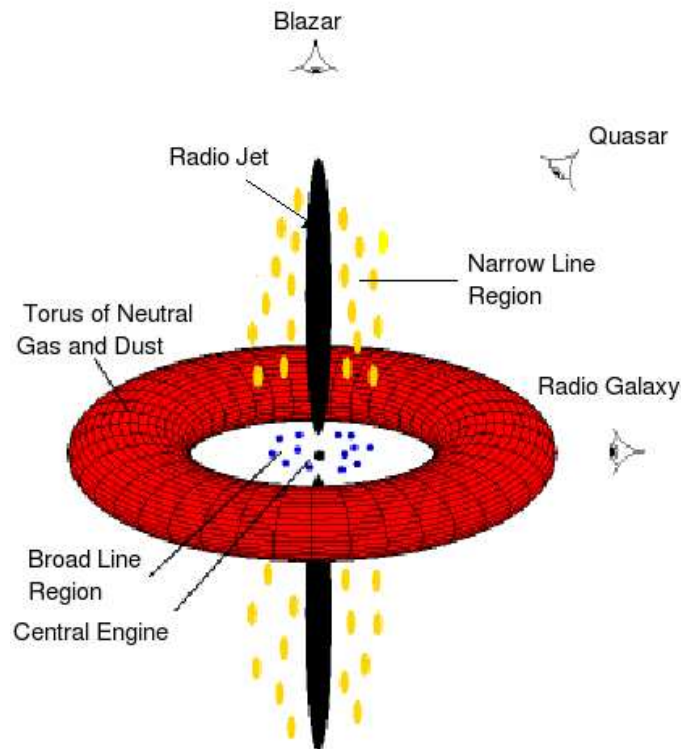
Abbildung 1.3: Illustration of the *unified AGN model.*

Other Sources

In addition to the supernova remnants, pulsars and AGN, which are discussed above, there are a number of other potential sources of VHE γ-ray emission, e.g. γ-ray bursts, microquasars, starburst galaxies etc. Further discussion of the physics of those sources is beyond the scope of this thesis, and can be found elsewhere ([150],[121]).

1.3.2 Gamma-ray Absorption

γ rays emitted in distant sources undergo absorption over the large distances in the intergalactic space.

The main absorption process is the interaction of γ rays with the cosmic microwave background radiation (CMBR) and the starlight (infrared background radiation) causing an electron-positron pair (Figure 1.4). The absorption of γ rays through interactions with the starlight becomes significant at γ-ray energies above ∼30 GeV and limits the horizon of γ rays to 500 Mpc at 1 TeV. Beyond 1 TeV up to 1 PeV the interaction of γ rays with the
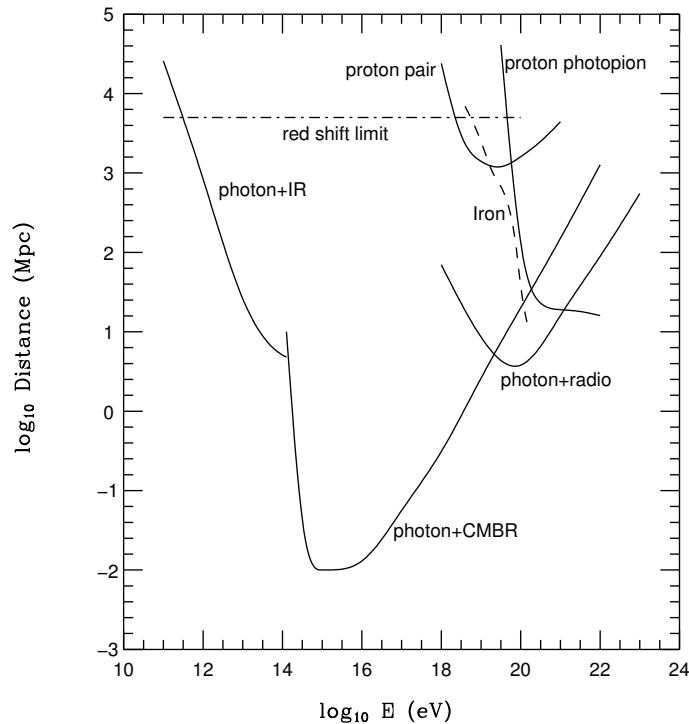
Abbildung 1.4: Absorption length of γ rays.

CMBR dominates so that the mean free path of γ rays is reduced to some kpc. Beyond 1 PeV the photon-photon pair production produces high-energy charged particles, which Inverse Compton scatter on the target photons and redistribute the high-energy γ-ray energy to lower energies. These γ rays produce the diffuse-cosmic continuum spsectrum in the form of a power-law with a spectral index of 2.

1.3.3 Gamma-ray Detectors in Space and on the Ground

The Earth's atmosphere is opaque to high-energy photons, because the integrated matter density is ~ 1000 g cm^{-2}, where the mass attenuation coefficient for air at 1 MeV is ~ 0.00642 g cm^{-2} giving an absorption probability for 1 MeV γ rays of $> 99.8\%$, [148]. Therefore, the probability that a γ-ray reaches even the highest mountains without interaction is very small (i.e. the operation height is at least at altitudes above ~ 40 km). Therefore, only space-born detectors can detect the primary γ rays directly.

- **Space-based γ-ray Detectors**

Space-born γ-ray detectors use tracking detectors and calorimeters, which measure the direction and the energy of the primary high-energy γ rays having energies ≥ 20 MeV. Tracking detectors are usually spark chambers, where the dominant interaction process for high-energy γ rays ($\gtrsim 30$ MeV) is the electron-positron pair-production. In the pair-production process the photon converts its complete energy into an electron-positron pair. The conversion layer is composed of a stack of thin metal layers. The spark chamber is filled with gas. Below the spark chamber scintillator plates are placed and they are viewed by photomultipliers. The created electron-positron pairs travel through the pair-tracking device and ionize the gas along the flight path. Then they penetrate into the scintillator plates, where photons are produced and registered by the photmultiplier tubes. A trigger pulse is produced, which fires the spark chamber by applying a high voltage to its plates and wires. This causes a spark to break through along the flight path. This can be recorded by an optical camera or an electronic readout, [148]. In this way the direction of the γ rays and the angular resolution of the detector can be determined.

SAS-II (Small Astronomy Satellite-II) pair-tracking telescope, launched on 1972 and survived only half a year due to a failure of the power supply. The energy range of this detector was 20 MeV - 1 GeV. It demonstrated for the first time the possibility to detect high-energy cosmic γ rays. For more details refer to [58].

COS-B (COsmic ray Satellite-B) provided the first complete map of the γ-ray universe. Launched on 1975, COS-B was originally projected to last two years, but it operated successfully for 6 years and 8 months until 1982. In this time about 2200 counts were detected from point sources on the axis. This was one of the pair-tracking telescopes designed to detect γ rays at energies in the range 2 keV - 5 GeV. It had a wide field of view (~ 2 sr). The energy resolution was $\sim 10\%$ for 100 MeV and $\sim 100\%$ at 1 GeV. The angular resolution was from $\sim 10°$ at 30 MeV to $\sim 2.5°$ at 2 GeV. More details can be found in [27].

CGRO (Compton Gamma Ray Observatory) was launched on April 5 1991. This mission remained in orbit until July 2000 and collected a huge amount of information about γ-ray sources. It carried four scientific instruments on board, which were BATSE ([136]), OSSE ([100]), COMPTEL ([150]), and EGRET.

- **EGRET** was the most sensitive space-born high-energy γ-ray telescope so far. It was aboard CGRO, and its energy range for de-
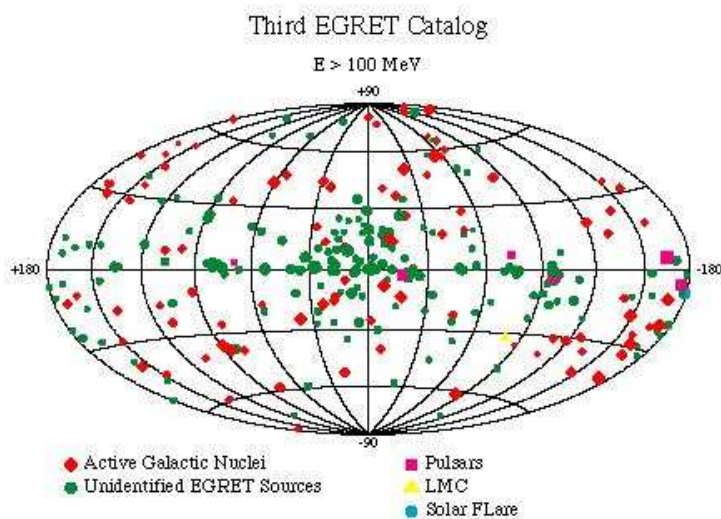
Abbildung 1.5: Sources listed in the third EGRET catalog, [81].

tection was from 20 MeV to ≈30 GeV [160, 80]. One of the successes of EGRET was a detection of about 90 extragalactic sources, most of which are blazars. In addition 6 pulsars were identified above ≈5 GeV. γ rays were detected from the Magellanic clouds. GeV emission from solar flares was observed. EGRET detected 170 unidentified sources [81], which still remain an enigma and strongly motivate further astrophysics research in this field. Figure 1.5 shows the sky in γ rays at energies above 100 MeV after EGRET. A full description of EGRET is given in [104].

AGILE (Astro-rivelatore Gamma a Immagini LEggero)(Light Imaging Detector for Gamma-ray Astronomy) in operation since 2003, and was designed for observations in the 10 - 40 keV band as well as between 20 MeV and 50 GeV [15].

GLAST (Gamma-ray Large Area Space Telescope) is a major next generation space telescope, designed to detect γ rays between 20 MeV and 300 GeV. GLAST is scheduled to be launched in 2006. It consists of 2 main detectors, the Large Area Telescope (LAT), which is the main instrument designed as a wide field detector, and the Gamma-ray Burst Monitor (GRM), which will alert GLAST to γ-ray bursts. More information on GLAST can be found in [67].

Table 1.2 summarizes basic physical parameters of the former, current, and next generation space γ-ray missions. The space-born detectors are limited in their effective areas, due to launch constraints, which in turn

Tabelle 1.2: Past and future space-based γ-ray detectors [68].

	EGRET	AGILE	GLAST
Energy range	20MeV - 30GeV	30MeV - 50GeV	20MeV - 300GeV
Energy resolution ($\Delta E / E$)	0.1	1	0.1
Effective area (peak) [cm^2]	1500	700	12000
Field of view [sr]	0.5	≈ 3	2.5
Angular resolution [deg] @ 100 MeV @ 10 GeV	5.8 0.5	4.7 0.2	3.5 0.1
Sensitivity ($\gtrsim 100 MeV$) [$cm^{-2}\ s^{-1}$]	10^{-7}	$5 \cdot 10^{-8}$	$2 \cdot 10^{-9}$
Mass [kg]	1810	60	2000
Lifetime	1991 - 1997	2003 - 2005	2006 - 2010

limit their energy range, since the flux of the high-energy γ rays decrease rapidly with energy. However, for energies above 100 GeV the atmosphere itself turns into a detector. Through the interactions of these primary photons with the atmosphere, large particle showers develop. The development of these air-showers and the formation of Cherenkov light will be explained in detail in Section 3.1 and Section 3.2. Ground-based telescopes are used for the detection of this Cherenkov light, and therefore high-energy γ rays.

- **Ground-based Gamma-ray Detectors**

  At very high energies γ-ray observations are possible from the ground with e.g. atmospheric Cherenkov telescopes (ACT). These experiments can be grouped according to the technique they use to detect the Cherenkov light from the primary γ-rays: *Wave Front* detectors (*Solar Plants*) and the *Imaging Atmospheric Cherenkov Telescopes (IACT)*.

  The energy range between 10 GeV and 200 GeV is important, because most of the pulsars have cutoffs in this energy regime, as well as distant AGN. This region has not been covered by space-born detectors or ground-based IACTs. *Solar Plants* operate at lower energies up to 50 GeV. The threshold energies of space-born detectors and the IACTs can be compared from Tables 1.2 and 1.3. The recent *Solar Plant* experiments are STACEE ([155], [172]), and CELESTE ([138]).

  The second technique, IACT, was suggested by Weekes and Turver, [169], who aimed to increase the angular resolution of the ACT by ta-

king images of the air-shower. These experiments use detectors which focus the Cherenkov light from the atmospheric showers onto a very fast imaging camera, which consists of a group of photomultiplier tubes (PMTs). This technique is improved by increasing the number of telescopes, which enable to get an improved flux sensitivity. This means that weaker sources can be detected in shorter time scales. Furthermore, variable sources can be studied on shorter time scales.

Table 1.3 gives a summary for major IACT experiments that have been operational, or which are being under construction now. More information on detection technique is given in Section 3.3.

Tabelle 1.3: Some of the ground-based Cherenkov telescope arrays.

Experiment	Location	Number of Telescopes	Aperture [m]	Number of Pixels	Pixel Size [deg]	FoV [deg]	Threshold [GeV]
no longer operational							
HEGRA [52]	La Palma, Spain	5	3	271	0.25	4.6	500
CAT [16]	French Pyrenees	1	4	600	0.12	3	250
Durham [12]	Narrabi, Australia	3	7	109	0.25	4	250
operational							
Whipple [168]	Arizona, USA	1	10	490	0.25	3	250
CANGAROO [79]	Woomera, Australia	1	10	256	0.12	3	400
H.E.S.S. [96, 97]	Khomas Highland, Namibia	4	12	960	0.16	5	100
MAGIC [17]	La Palma, Spain	1	17	>800	0.1 - 0.2	4	30
under construction							
VERITAS [37]	Arizona, USA	7	10	499	0.15	3.5	80

Showers that reach the ground due to their high energies (> 50 TeV) reach the ground and they can be detected by large arrays of ground-based particle detectors, e.g. *Tibet Air Shower Array* ([11]). The energy threshold also depends on the altitude of the experiment. The energy threshold of the Tibet Air Shower array is 10 TeV. The directional information is obtained from timing information of the individual detectors, which is usually not good enough to detect single sources.
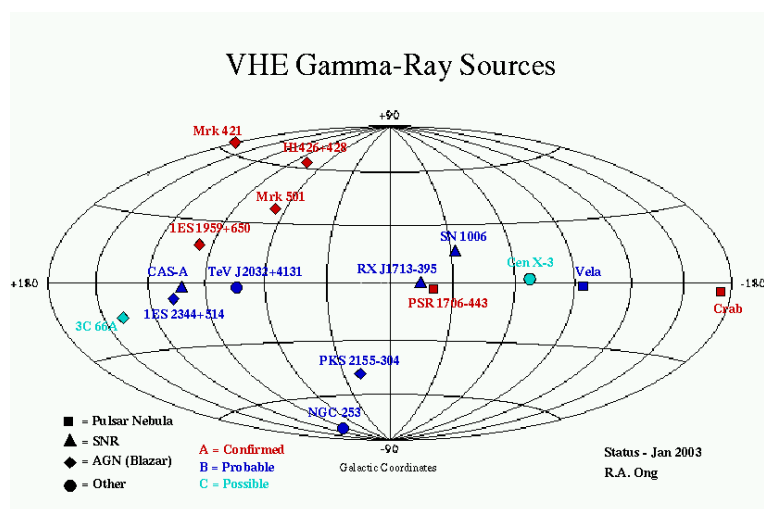
Abbildung 1.6: The sky observed in TeV γ rays by the ground-based Cherenkov detectors until 2003, [133].

1.3.4 TeV Gamma-ray Sky

The number of TeV *gamma*-ray sources has increased in the past decade with the progress in the IACT technique. Figure 1.6 shows all the detected galactic and extragalactic sources.

The galactic sources detected so far are the Crab Nebula, SNR/PSR B1706-44, Vela, which are plerion type SNRs, and SN1006, RXJ 1713.7-394 ([48]), Cassiopeia A (Cas A), which are shell type SNR, Cen X-3 (high mass X-ray binary), TeV J2032+4130 (not identified yet), PSR B1259-63 (binary pulsar with a Be-star companion) ([152]), and the Galactic center ([87]). All of these sources are confirmed by other experiments apart from Cas-A, Cen X-3 and TeV J2032+4130. The status of the past and present observations of SNR are summarized in the next Chapter.

The detected extragalactic sources are Mkn421, Mkn501, PKS2155-304 ([49]), 1ES2344-514, H1426+428, 1ES1959+650, 3C66A. Among these sources 1ES2344-514 and 3C66A still needs to be confirmed by other independent γ-ray telescopes.

Kapitel 2

Production Mechanisms of Cosmic Gamma Rays in Supernova Remnants

2.1 Evolution of Stars and Supernova Explosions

2.1.1 Birth of a Star

The general theory about the birth of a star is that it evolves through the gravitational collapse of nebulae or so-called giant molecular clouds (GMC), which basically consist of gas (mostly hydrogen) and dust. These clouds are cold (T $\simeq$ 10 - 30 K), and their density is 10^{20} times smaller than that of a star. Although the GMC are held up by internal pressure and magnetic fields, they may collapse when e.g. two of them collide, or when a star explodes nearby. Therefore, the disturbed GMC fragments into many clumps, where new stars might originate. Finally 10 - 1000 stars can be formed from the cloud. The closer the gas and dust particles in each clump approach each other the stronger acts the gravitational force upon them, through which the collapse of the star accelerates, and intensifies resulting in a sphere formed by the compressed particles on the nebula's center. This formation is the star's first stage of development, called *protostar*. The kinetic energy of the colliding particles in the dense center of the nebula turns into heat and it starts to glow in the IR-band or the radio-band. A protostar has a temperature of about 3000 K. At these temperatures, atoms in the star ionize and leave only positively charged hydrogen and helium nuclei. Meanwhile, the compression from surrounding matter increases, and the force of gravity exceeds the force

of repulsion between hydrogen nuclei. Eventually, at temperatures above 10 million K, *fusion* processes start. As the core heats up, hydrogen fusion goes faster, and core temperature and pressure rise. At this stage, a *stable star* is formed. The most important property of a stable star is that the force of gravity, which is exerted by the collapsing material, is balanced by the pressure gradient. The stability of the star is maintained through continuous nuclear-energy generation in its core.

2.1.2   The Hertzsprung-Russel Diagram

The study of a star begins with the measurements of the total amount of radiation emitted by a star, which is called the luminosity, and its surface temperature. The luminosity (or magnitude) of a star can be plotted against star temperature (or color)[1]. Figure 2.1 shows the H-R diagram for ~ 40000 nearby stars determined in recent observations made by the *Hipparcos* astrometry satellite of the European Space Agency [93]. This Figure shows that most of the stars are clustered in a certain well-defined regions of the H-R diagram.

Most of the stars shown in the H-R diagram (90%) lie along a narrow line, which goes from the bottom right to the top left of this diagram, and which is called the *main sequence*. From the observations of orbital motion of binary stars, masses of component stars are estimated and an empirical mass-luminosity relationship is derived, which is used to estimate the mass of the main sequence stars. It was found out that stars in this group differ from each other according to a simple rule: the more massive is a star the more luminous it is. This is given by the relation $\mathcal{L} \propto M^{3.9}$. So, the most massive stars lie at the top left end of the main sequence, and at the lowest right end of the main sequence the lowest mass stars are concentrated. The Sun is situated right at the middle of the main sequence.

Starting from the position of the Sun in the main sequence the *giant branch* is extending toward the top right corner of the H-R diagram. These stars are cool, large, and therefore bright (they have huge luminosities). Also there is a small third cluster to be seen on the H-R diagram below the main sequence line on the bottom left. These stars are the faint (10 magnitudes fainter than the Sun), blue, and compact stars, which are called the *white dwarfs*.

The masses of giants and dwarfs do not obey the mass-rule for main sequence stars. A dwarf and a giant having the same surface temperature

---

[1]For the first time this was done, independently, by Ejnar Hertzsprung and Henry Norris Russell around 1910. Therefore, this well-known luminosity-temperature diagram of the stars is called the *Hertzsprung-Russell* (H-R) diagram
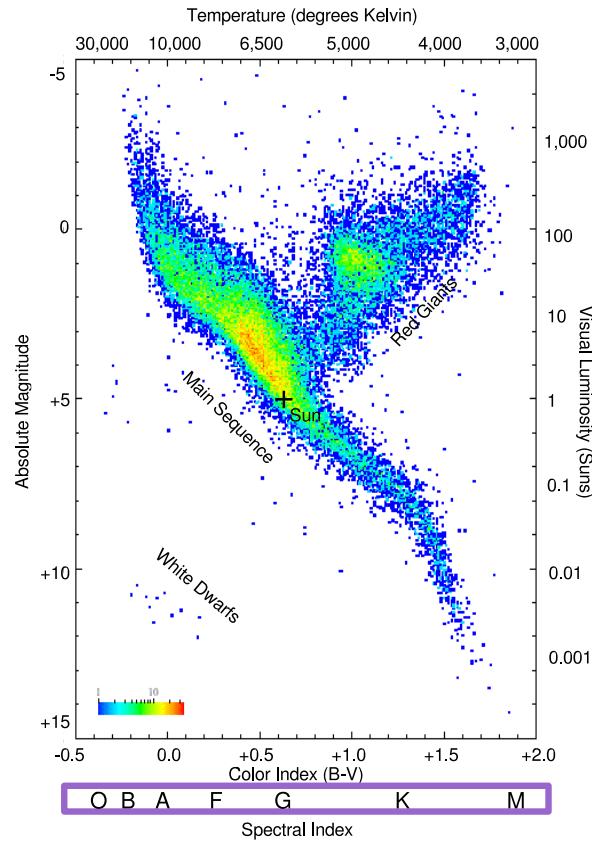
Abbildung 2.1: The well known Hertzsprung-Russell diagram showing the main sequence, giant, and white dwarf stars as three localized clusters. The color code gives the number of stars. In this diagram, there are altogether around 40000 nearby stars observed by the Hipparcos satellite [93]. More information on magnitude, color systems, etc. is given in [105] and [120].

also have nearly the same mass. On the other hand, because the luminosity of a giant is much higher than that of a dwarf star, from the Stefan-Boltzmann relation $\mathcal{L} \sim R^2 T^4$, it can be calculated that a giant has a much larger radius than that of a dwarf star.

2.1.3 Star Evolution

One of the main goals of the theory of stellar evolution is to understand, why stars cluster in certain regions of the H-R diagram, and how they evolve from one part to another. The H-R diagram is very useful in understanding the current stage of the evolution of a star. In star evolution the mass of a
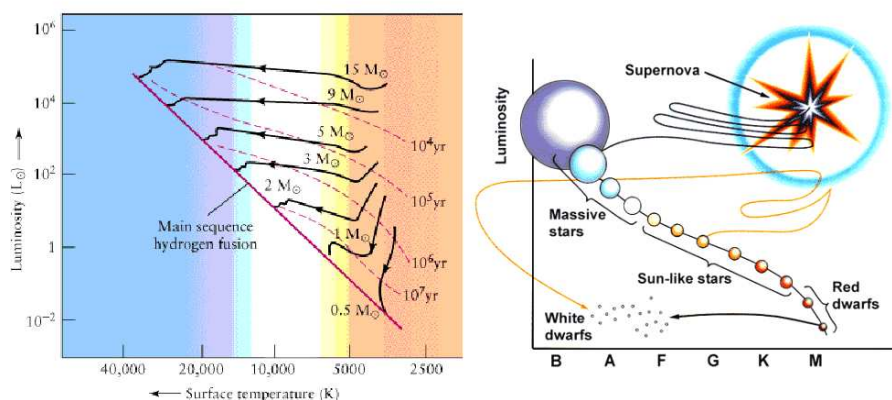
Abbildung 2.2: Evolution of stars. The left picture shows the process of birth of stars and their evolution to the main-sequence. The place they settle on the main-sequence is determined by their initial masses. This process is also called as *Hayashi contraction*, and lasts millions of years. The picture on the right shows the process of dying of three different types of stars: massive stars, sun-like stars and dwarf stars. The evolution of time can be followed as indicated by arrows.

star plays a very important role, because stars with different masses follow different paths in the H-R diagram in their evolution, which can be seen in different phases that the star goes through.

While the star becomes *stable*, its position on the H-R diagram moves according to its mass, from the upper right corner of the diagram, which is the faint and cool stage of the star, to the upper left side, which is the hot and bright phase. Now, the star starts to evolve on the thermal time scale. In this so-called *pre-main-sequence* phase, the star moves slowly from the upper left position on the HR-diagram to settle somewhere along the main-sequence stars depending on its mass. This phase is illustrated in Figure 2.2 (left) and it is also known as the *Hayashi contraction phase* of a protostar. The time for a star to reach the main-sequence varies with its mass. A star with a mass of our sun ($M_\odot$) reaches the main-sequence in 3×10^7 years. A star with a $0.5 M_\odot$ come to this stage in 10^8 years and another with a mass about $15 M_\odot$ in 6×10^5 years.

In the *main-sequence phase*, temperatures in the cores of the stars are so high that hydrogen starts to be converted to helium releasing 0.7% of the rest mass energy, which is the binding energy of helium. The primary output from these so-called *thermonuclear* reactions are photons and a large number of other particles such as neutrinos. There are two types of thermonuclear

reactions, by which hydrogen can be converted into helium. The type of reaction is determined by the initial temperature of the core of the star. Therefore, when the temperature of the star is less than about 2×10^7 K, the *p-p chain reaction* is the primary energy source. If the temperature is greater than this value, the reaction cycle is known as the carbon-nitrogen-oxygen (CNO) cycle, which becomes a dominant process. In the p-p reaction the hydrogen is used as a catalyst, whereas in the CNO cycle the ^{12}C is used as catalyst in the formation of helium (^{4}He). The hydrogen burning phase is remarkably stable. For example, a solar mass star will live almost 10 billion years.

The *post-main-sequence* evolution appears to be different for massive stars than for low-mass stars. When a low mass star ($\lesssim 8M_\odot$) exhausts the supply of hydrogen in its core, it contracts under gravity, heats up, and finally burns helium causing its luminosity to increase and move from the main-sequence to the giant branch (Figure 2.2 (right)). Eventually, helium burns completely and leaves the carbon core behind. Because the core can not withstand its own mass, it collapses under its own weight. At some stage the matter becomes so dense that the electron degeneracy pressure provides the balance against the weight. If the mass of the core is less than $1.2M_\odot$, the star turns into a *white dwarf* and the core moves into the white dwarf branch of the H-R diagram.

The high-mass stars ($\gtrsim 8M_\odot$) continue to convert hydrogen into helium and helium into carbon and slowly move up to the giant branch in the H-R diagram. After the supply of helium in the core is depleted, lighter elements are fused to form heavier ones. Finally, iron is produced in the core, which is the most tightly bound element, but the production of iron continues in the surrounding layers. At some point gravitational pressure in the core exceeds the electron degeneracy pressure and core collapse follows. Due to the core collapse, the temperature in the core rises and the photo-disintegration of iron into helium occurs. The newly formed helium atoms then further disintegrate into protons and neutrons. Protons in turn combine with ambient electrons to form neutrons. Eventually, the neutron density increases and the neutron degeneracy pressure prevents further gravitational collapse. Meanwhile, however, the outer layers continue falling inward and eventually rebound in a massive explosion. The result is a huge shock wave that moves radially out from the core expanding into interstellar space medium (ISM). The surviving degenerate core is extremely dense, with typical mass of M $\simeq$ $1.4M_\odot$ and radius R $\simeq$ 15 km.

This type of explosion of a single star is called *supernova explosion type II* (The *supernova explosion type I* usually happens in binary systems.), the surviving core is referred to as the *neutron star*, and the shock-front is called

supernova remnant. The Crab Nebula is a supernova remnant formed by this type of supernova explosion in the year A.C. 1054, and the Crab pulsar is the resultant neutron star.

2.2 Production Processes of Cosmic Gamma Rays

γ rays are produced in non-thermal processes like interactions of radiation with matter fields. Supernova remnants, where charged particles may be accelerated to TeV energies at the shock fronts, may produce the γ rays (more details on the mechanism of acceleration in SNRs can be found Section 2.4). Also the vicinity of a neutron star which is highly magnetized, or a jet of an AGN are possible production sites of high-energy γ rays. In the following Sections, the possible production mechanisms of high-energy γ rays are briefly summarized.

2.2.1 Charged Particles in Strong Electric or Magnetic Fields

The charge of a particle at rest produces a Coulomb field. When the particle moves, its corresponding electromagnetic field also varies. According to Maxwell's equations, all accelerated charged particles emit electromagnetic radiation. photons are emitted by accelerated charged particles, while momentum is conserved in the whole process.

Cyclotron Radiation

After a non-relativistic charged particle enters a magnetic field, it gyrates (rotates) non-relativistically around magnetic field lines with an angle θ (pitch angle) between the particle's trajectory and the direction of magnetic field and with a specific *Larmor frequency* given by:

$$\nu_L = \frac{eB}{mc} \ ,$$

where e and m are the charge and the mass of the particle, respectively. B is the magnetic field strength and c is the speed of light. The gyration radius is maintained by the balance between the Lorentz force of the magnetic field and the centrifugal repulsion of the orbiting particle. A rotating charged particle emits electromagnetic waves. This type of radiation is called *cyclotron radiation.* It is observed that while the charged particle is moving in the
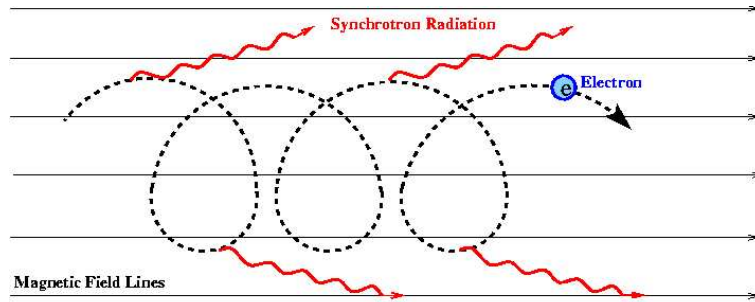
Abbildung 2.3: Synchrotron radiation is emitted by relativistic electrons as they spiral around magnetic field lines.

magnetic field, circularly or linearly polarized waves are emitted depending on the direction of the observer to the magnetic field.

Synchrotron Radiation

Cyclotron radiation is replaced by the *synchrotron radiation*, when the charged particle moves with a speed close to the speed of light. The motion of the particle is circular in trajectory and uniform around the magnetic field lines, but if the velocity along the field lines is non-zero, the path becomes helical as shown in Figure 2.3. Therefore, the radiation emitted by the charged particles is beamed into a cone of angle $\vartheta \approx mc^2/E$. An observer located at the orbital plane of the electron will only see radiation when the cone is pointed in that direction. Instead of a single frequency, the radiation now is emitted as a continuum spectrum about the ν_c, which is the critical frequency at which the maximum power is emitted. ν_c can be written as

$$\nu_c = \frac{3}{2} \left(\frac{eB}{mc} \right) \Gamma^2 \sin \phi,$$

where ϕ is the pitch angle between the direction of the magnetic field and that of the electron and $\Gamma = E/m$ is the Lorentz factor of the particle with mass m and energy E. The critical frequency can be calculated as

$$\nu_c \approx 100 \ B \ E^2 \ \sin \phi \quad \text{MHz} ,$$

where B is measured in μG and E in GeV.

The loss of energy is given by

$$-\frac{dE}{dx} = \frac{1}{c}\frac{dE}{dt} = \left(\frac{2e^4}{3m^2c^4} \right) \Gamma^2 B^2 \quad \text{erg cm}^{-1},$$

where B is measured in G and E in erg. The power distribution below ν_c can be given as

$$P(\nu/\nu_c) \;=\; 0.256(\frac{\nu}{\nu_c})^{1/3},$$

and above ν_c can be given as

$$P(\nu/\nu_c) \;=\; \frac{1}{16}\left(\frac{\pi\nu}{\nu_c}\right)^{1/2}\exp\left(-\frac{2}{3}\frac{\nu}{\nu_c}\right) \;\;,$$

The power emitted by an accelerated particle has a characteristic two-lobe distribution around the direction of the acceleration.

In astrophysical sources the electron energies are obeying a power-law with index α so that

$$N(E) \;\propto\; E^{-\alpha} \,,$$

then the synchrotron spectrum also follows a power-law of

$$P(\nu) \;\propto\; \nu^{\beta} \,,$$

where the spectral index is $\beta = (1 - \alpha)/2$.

Curvature Radiation

In a strong magnetic field ($\sim 10^{12}$ G) an electron may be constrained to follow the path of a magnetic field line very closely, with pitch angle nearly zero. The magnetic field lines are generally curved and the electrons are accelerated transversely and radiate. This radiation is called *curvature radiation*. The frequency spectrum of curvature radiation is like the spectrum of synchrotron radiation: the spectrum depends on the magnetic field strength, the energy of the electron, and the curvature of the magnetic field lines. The relation between the particle energy spectral index (α) and the radiation spectral index (β) is given as $\alpha = 1 - 3\beta$ for the curvature radiation instead of $\alpha = 1 - 2\beta$ for the synchrotron radiation.

This type of production process for the VHE γ rays is expected to take place in pulsars and supernova remnants.

Bremsstrahlung

Acceleration of charged particles in electric fields is another production mechanism of γ rays. If an electron passing by a positively charged nucleus, the trajectory of the electron is altered leading to emission of electromagnetic radiation. This is the process known as *bremsstrahlung*. If the parent
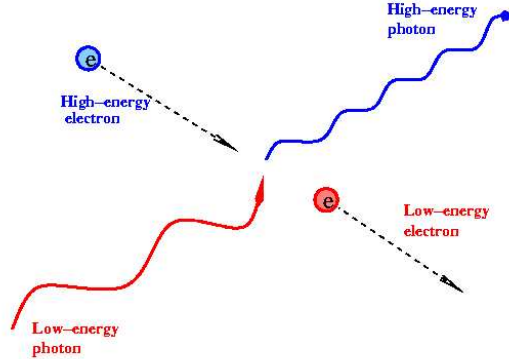
Abbildung 2.4: In the inverse Compton scattering process the low-energy photon, is up-scattered by a very high-energy electron.

electrons have an energy of $N(E_e) \sim E^{-\alpha}$, then the typical spectrum for Bremsstrahlung is given as

$$N(E_\gamma) \ \sim \ E_\gamma^{-\beta} \ , \tag{2.1}$$

where $\alpha = \beta$. The frequency range of this radiation depends on how much the electron trajectories are bent by the interaction with the positive ions or nucleus. This depends on the relative velocities of the two bodies, which in turn depends on the temperature of the gas.

An example of high-energy thermal bremsstrahlung is the X-ray emission from giant elliptical galaxies and hot inter-cluster gas. The high-energy thermal bremsstrahlung does play a very important role in studies of diffuse Galactic emission for energies smaller than 200 GeV, but it is not a primary TeV γ-ray production mechanism in supernova remnants and pulsars.

2.2.2   Inverse Compton Scattering

If photons of lower energy collide with energetic electrons, they gain energy in the collisions. This process is known as the *inverse Compton (IC) process* , which is illustrated in Figure 2.4. The cross section of IC-scattering is approximately described by the *Thomson scattering*, only when the photon's energy in the electron rest frame is smaller than the electron mass $(E_\gamma \ll m_e c^2)$. It is given as follows

$$\sigma_T \ = \ \frac{8\pi}{3} \, r_e^2 \ ,$$
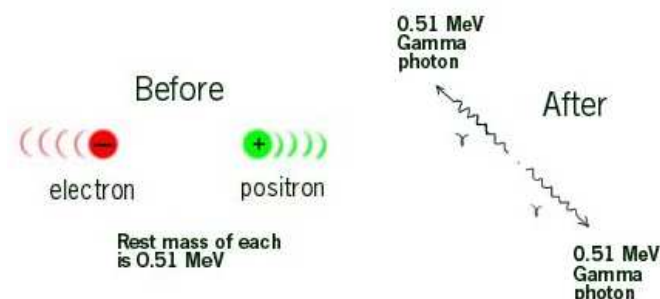
Abbildung 2.5: The annihilation of an electron with a positron gives two γ rays.

where $r_e = 2.8 \times 10^{-13}$ cm is the classical electron radius.

However, around MeV energies, where $E_\gamma \gtrsim m_e c^2$, the cross section of the interaction is described by the Klein-Nishina formula, which is given by

$$\sigma_{KN} = r_e^2 \, \frac{\pi m_e c^2}{E_\gamma} \left[\ln \left(\frac{2E_\gamma}{m_e c^2} + \frac{1}{2} \right) \right] \, .$$

Inverse Compton scattering is considered from relativistic electrons, which have a power-law distribution of the form

$$N(E_e) \sim E^{-\alpha} \, ,$$

and with a soft photon density of $\rho_p h$. The resulting γ rays will have characteristic (Thompson) energies of $\Gamma^2 h\nu$ or (Klein-Nishina) energies of $\Gamma h\nu$, where $h\nu$ is the energy of the soft photon and Γ is the Lorentz factor. The spectrum of the resulting γ rays are given as

$$N(E_\gamma) \sim E_\gamma^{-(\alpha+1)/2} \, ,$$

This process is important in regions with high photon densities. For example, in compact objects like neutron stars, which generate beams of charged particles in their vicinity.

2.2.3 Decays and Annihilation

Pair Annihilation

Annihilation between particles and antiparticles may also produce γ rays. The annihilation process of an electron and positron is shown in Figure 2.5.

The γ rays from pair annihilation are produced in the vicinity of radioactive decay regions, or energetic environments capable of positron production by other processes. Examples can be neutron stars or black holes, which have high energy densities and strong gravitational and magnetic fields.

Similarly, hadronic anti-particles may annihilate with with their particles. This may cause the spectral features at correspondingly higher energies in the γ-ray spectrum.

Pion Production and Decay

The pion is an elementary particle, which is created in strong interaction processes, such as a collision of an accelerated cosmic-ray proton with a nucleus in the ambient gas or with another proton or high-energy photon. In such an interaction charged ($\pi^{\pm}$) or neutral (π^0) secondary pions are created (see Figure 2.6). The neutral pions then rapidly decay into two γ rays, each of which has an energy of $\sim$70 MeV in the rest frame of π^0. The charged pions decay into muons and neutrinos.

If the cosmic ray has a power-law spectrum with a spectral index of α, then for higher energies the gamma-ray spectral distribution is a power-law with spectral index $\beta = (4/3)(\alpha - 1/2)$. When the energy decreases, the spectrum turns over with a peak at 70 MeV. This peak is the characteristic feature of the p-p interaction and a signature of hadrons as primary cosmic rays.

2.3   Supernova Remnants (SNRs)

In a supernova explosion, a shell of ejected material expands rapidly and sweeps up the surrounding matter. If the explosion happens in a uniform matter density, the shell is expected to expand spherically symmetrically. A low density medium (0.3 atom cm^{-3}) is left behind the expanding shell and after some time it becomes transparent to light. This limb brightened, hollow spherical structure is known as *supernova remnant*. Just after the SN explosion the mass of the swept up material is less than the mass of ejecta (about M$_{\odot}$), therefore the expansion proceeds with a uniform velocity (of the order of 15,000 km s^{-1}). This *free expansion* is the first stage of a SNR's life. A shock wave forms at the front edge of the stellar ejecta, because its velocity (10 km s^{-1}) is much higher than the speed of sound. Atoms hit by the shock wave ionize and consequently the temperature rises up to 10^7 - 10^8 K. Everything in front of the shock is propelled forward with the shock.

After $\sim$200 years the expansion decelerates until the radius of the SNR
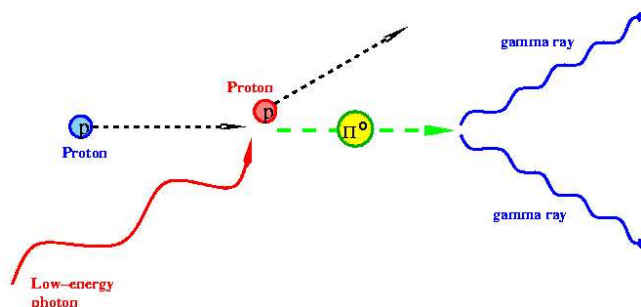
Abbildung 2.6: One of the possibilities of pion production, which is followed by its decay. The pion decay leads to high-energy photons.

is ∼3 pc, and the mass of the swept up material becomes equal to that of ejecta. So, the SNR enters a second phase of adiabatic expansion, which is known as *Sedov phase* or *blast-wave* phase. In this phase the mass of the swept up material gets larger than the mass of ejecta, but the internal kinetic energy of the SNR is still bigger compared to the energy radiated by the shell. Therefore, the rate of expansion is still determined by the initial energy of the explosion and the density of the ISM. While the SN ejecta expands it sweeps up much colder interstellar space matter and so becomes cooler and more massive.

After cooling of the ejected material in and behind the shock, the SNR reaches its third phase, which is called *radiative phase*. This phase lasts around 10^5 yr and the internal energy of the SNR is radiated away during this phase. After some time the shell becomes indistinguishable from the surrounding ISM.

There are three types of SNR, which are shortly explained below.

2.3.1   Shell-Type SNRs

In Figure 2.7 an X-ray image of the supernova remnants *Cygnus Loop* and *Tycho* are shown as two examples for shell-type SNR. One can see the spherically symmetric SNR surrounded by a big shell of bright (or hot) material. This appearance can be explained by the fact we see more shell material along out line of sight at the edges and we almost see nothing in the center of the remnant. This effect is called *limb brightening*. 80% of all observed SNRs are shell-type supernova remnants. The list of the shell-type SNRs observed within the past years by imaging atmospheric Cherenkov telescopes is given in Table 2.1.
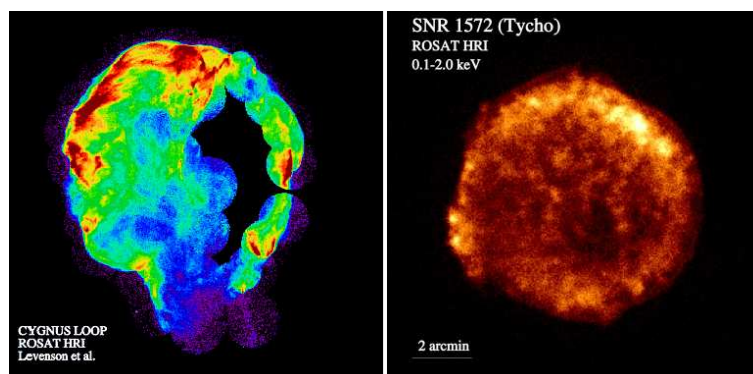
Abbildung 2.7: Two examples of shell-type SNRs. Picture on the right is the Tycho supernova remnant and the picture on the left is the Cygnus Loop observed by ROSAT X-ray satellite.

2.3.2 Plerions

Plerions, which are also known as *pulsar wind nebulae*, are roughly spherical in shape and have filled central regions. The name *plerion*, comes from the word *full* in Greek, and it is given to this type of SNR, because it has a very bright emission, which can be observed from all parts of the remnant. The intensity of this emission is most intense at the center. The type of the emission is synchrotron emission and it is supposed to be caused by a pulsar, which rotates at the center of the SNR. This emission is produced by the ultra-relativistic electrons, which are emitted by the neutron star into its surrounding strong magnetic field. The Crab SNR is a very typical example of this type of SNR. More details on the Crab plerion are given in Section 2.5. Other plerions, which were observed within the past years by imaging atmospheric Cherenkov telescopes, are listed in Table 2.2.

2.3.3 Composite SNRs

Composite supernova remnants carry characteristics from both plerions and shell-type SNRs. Figure 2.8 shows an X-ray image of the Vela complex, which has a hot shell with a small synchrotron nebula having a diameter of about 1' located at the center of the shell.

2.4 Particle Acceleration in SNRs

The main production mechanisms responsible for high-energy γ-ray emission in SNRs are synchrotron emission of electrons in the SNR magnetic field,

Tabelle 2.1: Past observations of the shell-type SNRs in GeV - TeV γ-ray range (information compiled from [63], [8]), as well as the recent observation results of the H.E.S.S. experiment about RXJ 1713-3946.

Shell-SNR Name	Exposure Time [hrs]	Flux/ Upper Limit [$\times 10^{-11} \text{cm}^{-2}\text{s}^{-1}$]
H.E.S.S.		
RXJ 1713-3946 [48]	18.1	1.46 (≥ 1.0 TeV)
CANGAROO		
RXJ 1713-3946 [130, 62]	66	0.53 (≥ 1.8 TeV)
SN1006 [158]	34	0.46 (≥ 1.7 TeV)
HEGRA		
Monoceros [8]	120	0.17 (> 800 GeV)
Cas A [6]	232	0.058 (> 1 TeV)
Tycho [7]	64.6	< 0.058 (> 1 TeV)
γ-Cygni [139]	47	< 1.1 (> 500 GeV)
Durham Group		
SN1006 [42]	41	< 1.7 (> 300 GeV)
Whipple		
Monoceros [115]	13.1	< 4.8 (> 500 GeV)
Cas A [115]	6.9	< 0.66 (> 500 GeV)
Tycho [39]	14.5	< 0.8 (> 300 GeV)
γ-Cygni [39]	9.3	< 2.2 (> 300 GeV)
W44 [39]	6.0	< 3.0 (> 300 GeV)
W51 [39]	7.8	< 3.6 (> 300 GeV)
W63 [39]	2.3	< 6.4 (> 300 GeV)
CAT		
Cas A [74]	24.4	< 0.74 (> 400 GeV)

IC-scattering, electron bremsstrahlung, and π° production. The first three mechanisms involve electrons. The fourth mechanism involves hadrons. In all of these processes the VHE γ-ray production is only possible, when the seed particles whether hadrons or electrons have very high energies. For this reason, it is important to understand the possible acceleration mechanisms of charged particles. There are three fundamental processes, through which particles can be accelerated, [128, 120]. These are given below:

- **Shock Acceleration:** Shock waves are smooth bulk motions of plasma produced in SN explosions and these waves propagate into the interstellar space sweeping up interstellar matter. Particles passing through *shock fronts* of SNRs can be accelerated by the *first-order Fermi acceleration mechanism*. In this mechanism, a particle passing though a shock will be scattered by magnetic inhomogeneities behind the shock.

Tabelle 2.2: Past Observations of the Plerions in GeV - TeV γ-ray range. Information taken from [63].

Plerion Name	Exposure Time [hrs]	Flux/ Upper Limit [$\times 10^{-11} \text{cm}^{-2}\text{s}^{-1}$]	Pulsation in VHE γ-ray Signal
ALL ground-based detectors in Section 1.3.3			
Crab Nebula [11, 9, 134, 57, 92]	$\rightarrow \infty$	7.0 (> 400 GeV)	No
CANGAROO			
PSR 1706-44 [109]	60	0.15 (> 1 TeV)	No
Vela Pulsar [173]	116	0.26 (E/2 TeV)$^{-2.4}$ TeV^{-1}	No
Durham Group			
PSR 1706-44 [41]	10	1.25 (> 300 GeV)	No
Vela Pulsar [36]	8.75	< 5.0 (> 300 GeV)	No

The particle gains energy from this interaction and scatters back and crosses the shock front again. It can again be scattered by the magnetic inhomogeneities this time ahead of the shock, and so bounces back and forth many times gaining energy each time. The energy that a particle gains is proportional to v/c, where v is the velocity of the shock front relative to the un-shocked interstellar space and c is the speed of light. After n crossings the particle has an energy of $E = E_0 (v/c)^n$. After certain time the particles will be carried away by the downstream shock. If the probability of remaining in the shock region after each crossing is P, then after n crossings, the remaining number of particles, N, is given as $N = N_0 P^n$, where N_0 is the initial number of particles before the interaction with the shock front. The resulting energy spectrum of these particles is approximately $dN/dE = E^{-\alpha}$, where $\alpha \sim 2.0$ - 2.5. This mechanism is also known as *diffusive shock acceleration (DSA) mechanism*, which was introduced by Blanford and Ostriker, [29], and Bell, [20] in 1978. The observational evidence that cosmic-ray electrons are accelerated in SNRs is given in Sections 2.3.1 and 2.3.2.

- **Stochastic Acceleration:** In this scenario, particles are immersed in a turbulent medium and change their energy randomly due to many interactions with moving interstellar magnetic field and are eventually, on average, accelerated. This process is called the *second-order Fermi acceleration mechanism*. Through this mechanism particles gain energy proportional to v^2/c^2.
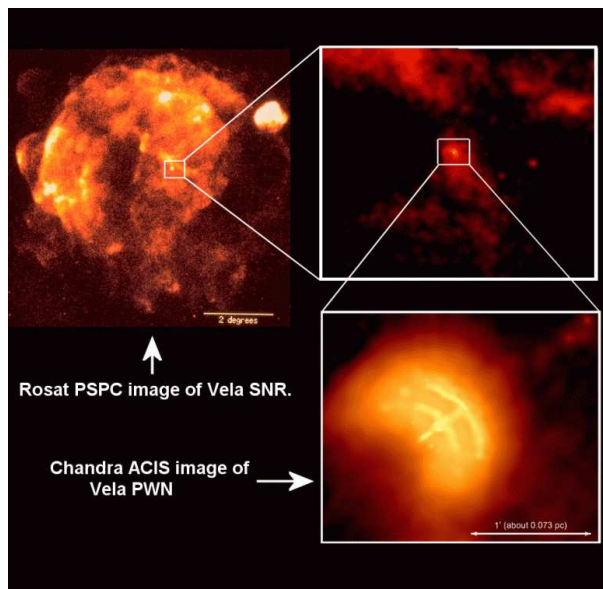
Abbildung 2.8: The Vela supernova remnant as a good example for composite type SNRs. The picture shows an X-ray image taken by the ROSAT and Chandra satellites.

- **Direct Acceleration:** The most direct way to accelerate charged particles is through DC electric fields. This type of mechanism is used to explain the acceleration of particles in neutron stars. One problem in this scenario is that oppositely charged particles are accelerated in opposite directions, and a large scale charge separation occurs. While particles gain energy from the electric field, they are exposed to the drag force from the oppositely charged particles. Therefore, it is the interplay between these two forces that determines whether or not electrons or ions can be accelerated out of a bulk particle distribution.

Because SNRs are regarded as the most probable production and acceleration sites of cosmic rays, the TeV γ-ray observations of SNRs play an important role in the debate of probing the origin of the cosmic rays. These debates were first proposed by Ginzburg and Syrovatskii, [71].

Detection of the signature of a π^0-bump at MeV energies and a spectrum extending to tens of TeV would be a clear indication that cosmic-ray acceleration does take place in SNRs (*DAV model* proposed by Drury, Aharonian, and Völk, [61]). The γ-ray emission from π^0 decay peaks at the beginning of the Sedov phase (Section 2.3) and then slowly decays with the SNR evolution in time. The expected γ-ray spectrum is very hard, which enables TeV γ-ray observations. However, the γ-ray luminosity from π^0 decay compared

to the luminosity from inverse-Compton scattering of relativistic electrons and CMBR is be too low to be detected above 100 MeV in most of the SNRs. From a selected set of shell-type SNRs observed by EGRET, the ones having an interaction with a nearby molecular cloud (which provides a high-density target for π° production) can be selected for further observations in TeV range.

The energy spectrum of most of the shell-type SNRs listed in Table 2.1 and Table 2.2 like Vela and SN1006 can be explained as a composite of a synchrotron and an inverse-Compton component emitted by a population of accelerated electrons. Detected TeV fluxes from two other SNRs, Cas A and PSR 1706-44, are not strong enough to constrain the emission mechanisms. However, the energy spectrum of RX J1713-3946 is claimed by CANGAROO collaboration (Section 1.3.3) to fit best to the models, which produce γ rays via π^0 decay. This claim has been disputed by Reimer and Pohl [143]. They used the complete data set of EGRET measurements to show that the GeV flux required by π^0 decay models significantly exceeds the EGRET measurements. From the recent results of the H.E.S.S. experiment on RX J1713-3946 observations, it can be concluded that because this SNR is also interacting with some molecular clouds, it needs multi-wavelength observations to disentangle the relative contributions of various processes, [48].

2.5 Model of Gamma-ray Emission from the Crab Nebula

The Crab system of nebula and pulsar (NGC 1952), in the constellation of Taurus, is one of the most spectacular and extensively studied objects in astrophysics so far. The birth of this SNR and its pulsar from a supernova of type II, was first observed and recorded by the Chinese, Japanese, and native Americans on A.D. 1054. The new bright "star" was visible at daytime for several days. After a year it faded away, but still could be observed with the naked eye at night time for almost two years. In 1758 it appeared in the catalog of nebulae compiled by Charles Messier, as the nebula M1. In 1791 the British Astronomer John Bevis rediscovered it. The name "Crab Nebula" was given after its tentacle like structure was observed hundred years later (in 1844) by Lord Rosse, [121].

The Crab Nebula is contained in an ellipse 180" × 120" across. The diameter of the remnant is 6 light years. The apparent magnitude is between −6.5 and +7.0, because the distance measured to the Crab Nebula is about 6500 light years ($\sim$ 2 kpc), the absolute magnitude is around −16.5. Op-
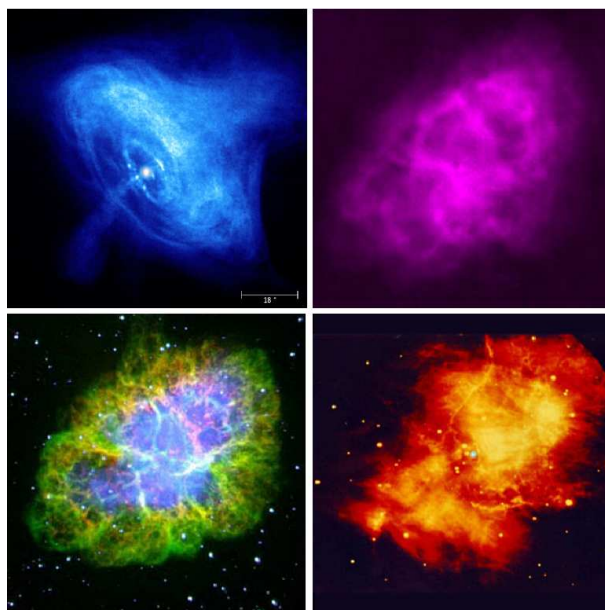
Abbildung 2.9: Multi-wavelength image of supernova remnant Crab. The upper-left image is taken in X-rays, the upper-right picture shows the radio image. The lower-right picture is taken in infrared, and the lower-left picture is the optical image.

tical observations taken with modern telescopes have established the Crab Nebula as a web of bright filaments. These filaments effectively confine the expanding nebula, which in turn accelerates the filaments. From Doppler shift measurements it is found that they expand with a speed of 1000 km/sec.

In 1949 the radio astronomers Bolton, Stanley and Slee [30] identified the Crab Nebula as a radio source. The radio flux density was higher than the optical flux so that the continuum radiation could not be explained in the familiar terms of thermal radiation from ionized gas. This continuum radiation was first explained by Shklovsky in 1953 [154] to be synchrotron radiation emitted by relativistic electrons moving in the magnetic field. Later, it was observed that the whole of the nebula generated optical, radio, X-ray radiation at such a rate that its brightness should fade away within a few years. This showed that there existed another energy source of the Crab Nebula, apart from the supernova explosion observed 900 years ago. The theoretician Pacini suggested in 1967, [137], that a rapidly rotating and highly magnetized neutron star could provide energy for the Crab Nebula . The discovery of the *Crab pulsar (PSR B0531+21)*, was made in the radio b and in 1968, [156]. This was followed by the optical, and X-ray detections of pulsations at a period of 33 milliseconds, which are shown in Figure 2.11. In

1969 Gold, [72], showed that the change of kinetic energy of the neutron star is just of the magnitude needed to match the observed luminosity. This can be shown in a simplified way as follows: The rate of rotational energy loss in a pulsar is given by

$$\frac{dE_{rot}}{dt} \ = \ I \ \omega \ \frac{d\omega}{dt} \quad , \tag{2.2}$$

where I is the moment of inertia ($\sim (2/5)$ M R^2) and ω the angular velocity of the neutron star. ω and $\dot{\omega}$ are measured as 188 rad/s and 2.4×10^{-9} rad/s^2 respectively for the Crab pulsar. M and R are mass and radius of the neutron star typically of the order 2×10^{30} kg and 10 km, respectively. Equation 2.2 thus yields $\frac{dE_{rot}}{dt} \approx 3.6 \times 10^{31}$ W. While the neutron star is spinning rapidly in the intense magnetic field, it acts as a dynamo resulting in electromotive forces. It was shown by Ostriker and Gunn in 1969, [135], that the neutron star should emit *magnetic dipole* radiation with a power given by

$$\frac{dE_{rot}}{dt} \ \simeq \ \frac{2}{3} \left(\frac{B^2 \ R^6 \ \omega^4}{c^3} \right) \quad , \tag{2.3}$$

where B is the surface magnetic field of the neutron star. If the reason for the rotational slow-down of the neutron star is this dipole radiation, then Equation 2.2 can be equated to Equation 2.3. If the spin-down luminosity of the pulsar is known, then the magnetic field strength of the pulsar can be found, which is B$\sim 10^{12}$ for the Crab pulsar. This *magnetic dipole mechanism* explains the pulsar's spin-down rate, but the shortcoming of this model is that it does not take the surrounding medium of the pulsar into account. Goldreich and Julian, [73], proposed the *aligned rotator model*, in which the spin-axis and the magnetic axis are parallel. This model produces the same magnitude of spin-down for a pulsar. This model is illustrated in Figure 1.2. The strong electric field, which is estimated to be $\sim 3 \times 10^{10}$ Volt/cm by Goldreich and Julian, rips the electrons from the neutron star's surface and carries them into the magnetosphere of the neutron star. Some of these particles follow the closed field lines and rotate with the star, while the ones that are stripped from the poles follow open field lines out to infinity. These latter particles cause the *pulsar wind*, which carries away kinetic energy and angular momentum from the neutron star and causes it to spin down.

It was suggested by Hayakawa ([82]) in 1952, by Morrison ([129]) in 1958 and by Gould ([75]) in 1965 that the Crab Nebula could also be a source of VHE photons at the order of $\sim 10^{12}$ eV. The discovery of the Crab Nebula as a GeV and TeV emitter was made by R. Browning in 1971 [38] and by T.C. Weekes in 1989 [168], respectively. Today, for high-energy γ-ray astronomy
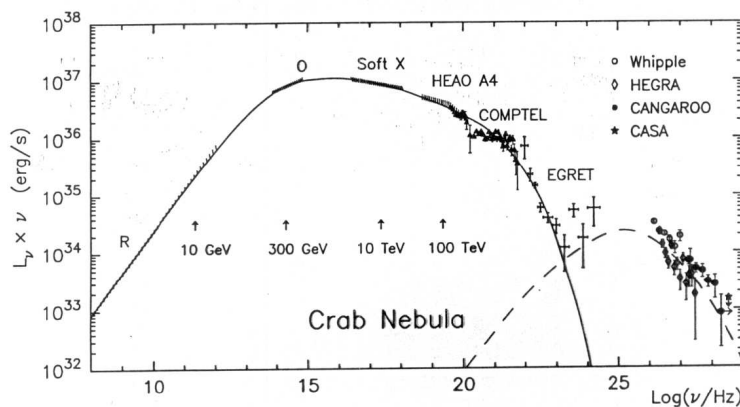
Abbildung 2.10: Multi-wavelength spectrum of a steady flux of the Crab Nebula. The energies given on the plot with arrows, show the energies of the electrons that produce the synchrotron radiation.

it is a very important object, which is routinely observed with a number of instruments as the standard candle at TeV energies. The Crab Nebula and the Crab pulsar are indistinguishable in γ-ray observations, although they can be easily separated in the observation bands from radio wavelengths to X-rays. The multi-wavelength observations of the Crab Nebula and Crab pulsar are shown in Figure 2.9.

Unpulsed Emission

In 1965 Gould pointed out that since the Crab Nebula is a source of synchrotron radiation, due to inverse Compton scattering it may also be a source for higher energy radiation, [75]. Since the synchrotron spectrum of Crab Nebula implies the presence of electrons with energies up to $\sim 10^{15}$ eV, IC emission between 100 GeV and 1 TeV is expected (see Figure 2.10).

Several experiments attempted to detect the IC-component of the spectrum of the Crab Nebula. The first clear detection of this component made by the Whipple collaboration was of a TeV signal (above 0.7 TeV) at 9σ level, [168]. After this detection, 13 other groups detected and confirmed a steady TeV γ-ray signal from the Crab Nebula. There is a good agreement between the measurements of different groups. The energy spectrum of the Crab Nebula at different wavelengths, together with the high-energy γ-ray measurements by the *Whipple*, *HEGRA*, and *CANGAROO* experiments are shown in Figure 2.10.

Pulsed Emission

Rotating with a period of 33.4 msec, the Crab pulsar is one of the fastest pulsars (a brief introduction to pulsars is given in Section 1.3.1), and it is in fact very special, because it maintains its pulse profile across all wavelengths, which can be seen in Figure 2.11.

According to models, which try to explain the alignment of the pulses, the photons from different wavelengths originate from the same place of the pulsar's magnetosphere.

Pulsed γ-ray emission from the Crab pulsar was first reported by balloon experiments and satellite experiments in the energy range between 1 MeV and 1 GeV. EGRET (Section 1.3.3), which was on board of the Compton Gamma Ray Observatory (CGRO) satellite, also detected the pulsed emission from the Crab pulsar, [64]. It was found out that the pulsed emission dominates over the whole observed range of energies, which can be seen from Figure 2.12 (left plot). The pulsed spectrum is softening around 1 GeV, and the un-pulsed spectrum gets harder above 1 GeV compared to pulsed spectrum. The TeV observation for pulsed emission fall into two categories: observations reporting pulses at TeV energies and observations giving upper limits. Figure 2.12 (right plot), is giving upper limits on the pulsed emission from the Crab above 10 GeV, observed by several ground based Cherenkov experiments (description of experiments is given below). By the recent TeV observations, the *Outer Gap* model, and *Polar Cap* model, mentioned in Section 1.3.1, are constrained. Although both Polar Cap and Outer Gap models have had some success in explaining observed spectra of pulsed γ-spectra, they have still a number of problems. For example, polar cap models can reproduce some features of the light curves and phase resolved spectra, but the emission at GeV energies is not fully understood yet. For polar cap models, the spectral cutoff is above 10 GeV due to the pair production effect. Likewise, Outer Gap models have also been used to explain pulsed spectra. They predict the pulsed emission at energies as high as $\sim$50 GeV, although at these energies the predicted fluxes are very low, [45]. Therefore, the current upper limits are within expectations. One can not distinguish between the two models yet. In order to do this, more detections in the energy range from 10 GeV to $\sim$200 GeV are required. It is expected that the satellite experiment GLAST (Section 1.3.3), which is currently under construction, and ground-based detectors like H.E.S.S. (Chapter 4) and MAGIC (Section 1.3.3) will cover this energy range. So far the upper limits have been obtained using the following experiments: Whipple at $\sim$250 GeV ([116]), STACEE at 190 GeV ([134]), CELESTE at 60 GeV ([57]).
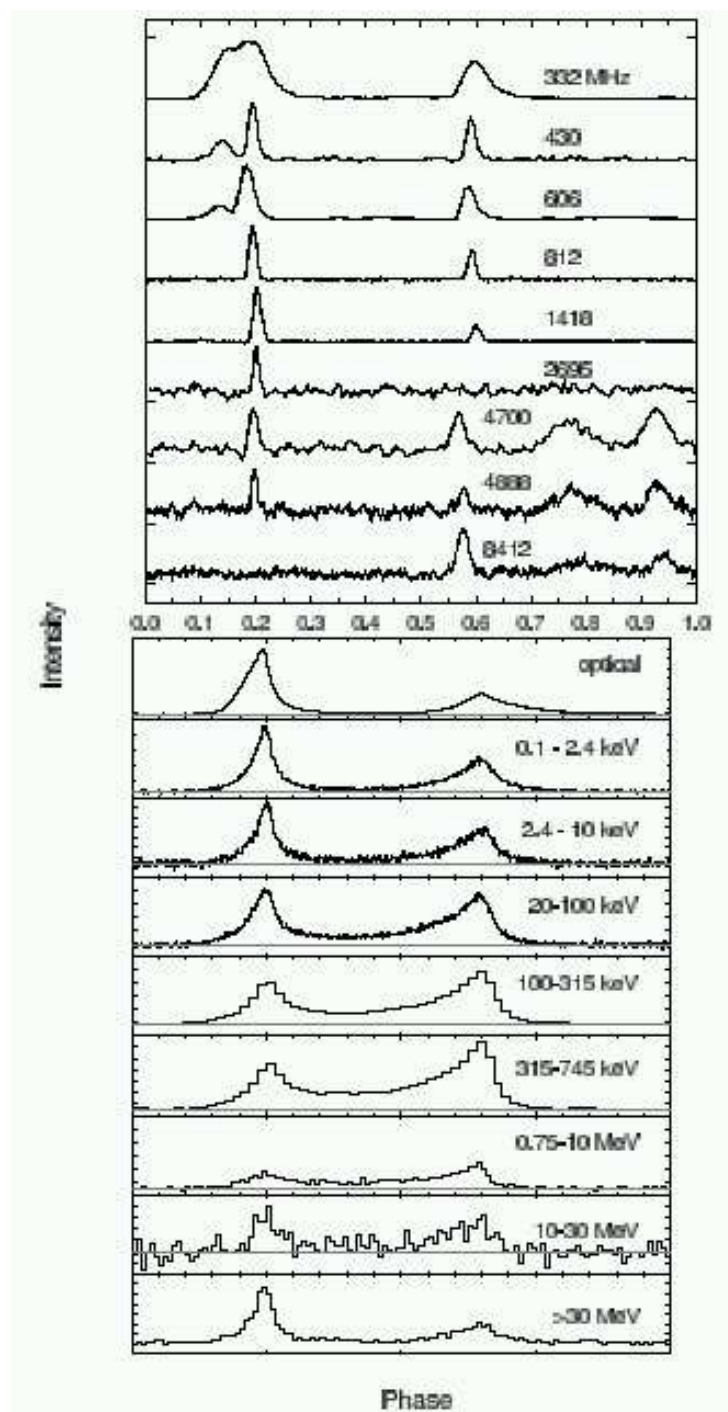
Abbildung 2.11: Multi-wavelength curves of the Crab pulsar. The phases shown at the upper plot are in radio wave-bands and the phases shown at the bottom are at higher energies. Figure taken from [103].
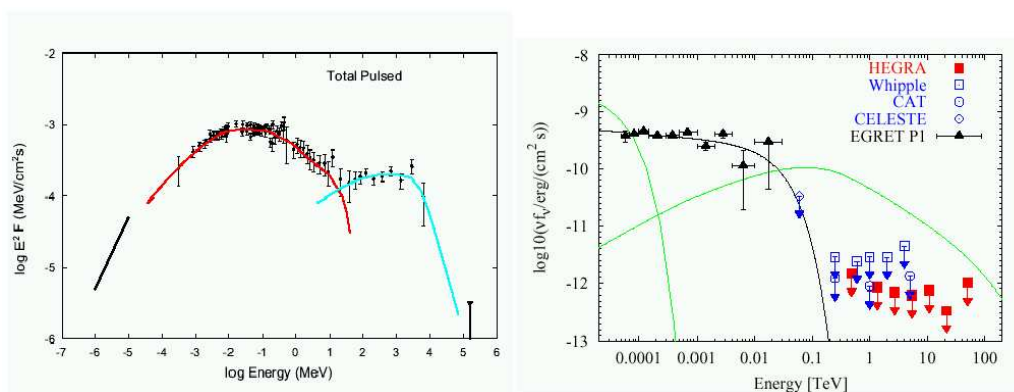
Abbildung 2.12: Left plot ([103]) shows the Crab pulsed emission spectrum together with theoretical predictions for the synchrotron spectrum at lower energies (red line) and the IC curvature radiation peak at higher energies (blue line). The right plot ([9]) shows the upper limits of pulsed emission from the Crab pulsar for energies above 10 GeV. The green line shows the Outer Gap model and the black curve shows the Polar Cap model (see text).

Kapitel 3

Detection Technique of Very High-energy Gamma Rays

3.1   Extensive Air-showers

High energy cosmic rays are evident in observations of extensive air-showers (EAS). An extensive air-shower is a cascade of secondary particles initiated by the interaction between a high energy cosmic particle that impinge on the atmosphere and an air molecule. The produced secondary particles interact with other air-molecules. Therefore, the number of secondary particles multiplies up to the point, where the mean particle energy is not more sufficient to create new particles. The number of secondary particles decreases as more and more particles fall below the threshold for further particle production. If showers are initiated by cosmic rays having energies higher than 100 TeV, then lots of secondary particles can reach the ground. Below 100 TeV most of the secondaries are absorbed in the atmosphere.

If the cosmic particle is an electron or a γ-ray, interactions that take place in the atmosphere are electromagnetic in nature, therefore these cascades are called *electromagnetic showers*. The air-showers initiated by protons or nuclei are called *nuclear cascades* (or *hadronic cascades*). The interactions in *nuclear cascades* are strong interactions, weak decays processes and electromagnetic interactions. Therefore, these showers contain *hadronic cascades* and *electromagnetic showers* as sub-showers (Figure 3.1).

3.1.1   Nuclear Cascade

In nuclear collisions of hadrons with atomic nuclei the nucleus splits into smaller nuclear fragments, which become detached and move off independently to undergo nuclear interactions on their own. As long as their energy
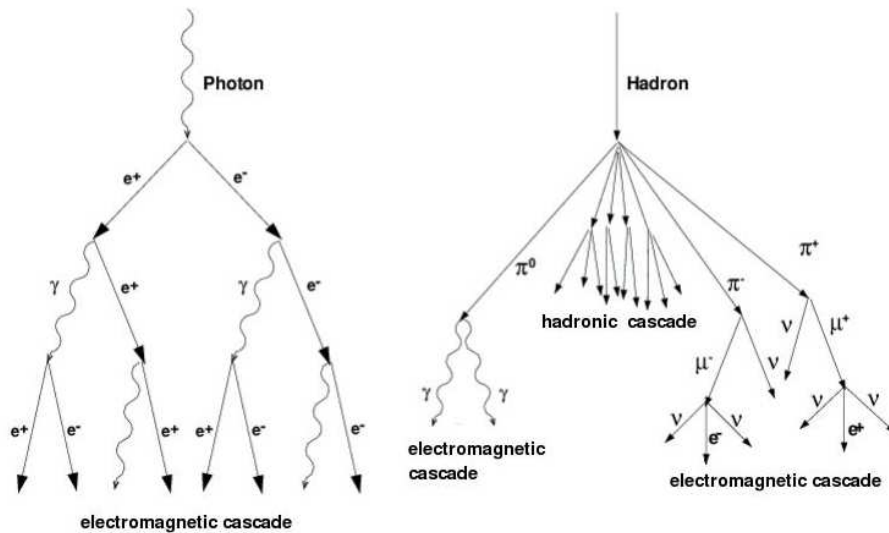
Abbildung 3.1: Development of air-shower in the Earth's atmosphere: a photon-induced shower (left), and a hadron-induced shower (right). Figure taken from [161].

is sufficient, primary hadron and daughter nucleons interact further to produce new particles such as hadrons (mostly pions), mesons (K-mesons), nuclei (neutrons, protons), hyperons, and nuclear fragments of the target nuclei. The mean distance taken along the vertical trajectory through the atmosphere down to sea level before the particle is fragmented in the first interaction is defined as the *interaction mean free path*, λ_i [g/cm^2]. The majority of the heavy nuclei have shorter mean free paths relative to protons, because their interaction cross sections, σ_i [cm^2], are much larger. The interaction mean free path is given by

$$\lambda_i = \frac{1}{N \, \sigma_i} \ ,$$

where N is the number of target nuclei per unit volume. The interaction mean free path of protons is ∼80 g/cm^2, [77].

When the energy of the initial is around 10 GeV or higher, the interactions may end up with multiple production of charged and neutral pions. The main decay channels of the neutral and charged pions are

$$\pi^+ \rightarrow \mu^+ + \nu_\mu \ ,$$
$$\pi^- \rightarrow \mu^- + \bar{\nu}_\mu \ ,$$
$$\pi^0 \rightarrow \gamma + \gamma \ .$$

The mean lifetime of charged pions is $\sim 2.6 \times 10^{-8}$ s, while it is $\sim 8.3 \times 10^{-17}$ s for neutral pions. So, hadronic air-showers also include an electromagnetic component, which is fed by the secondary photons produced through the π^0-decays. The average ratio of generated neutral pions to charged pions is roughly 1/3. A 1 TeV proton produces in one single interaction in the atmosphere about 12 secondary low energy pions. Some of those pions may interact again to form finally sub-hadronic showers. It is important to mention that the secondary particles of the nuclear cascade acquire non-negligible transverse momenta, which lead to substantial lateral spread of the nuclear cascade.

Muons are produced in the hadron-induced showers (Figure 3.1). The main decay channels for the muons are the following:

$$\mu^+ \rightarrow e^+ + \bar{\nu}_\mu + \nu_e \ ,$$
$$\mu^- \rightarrow e^- + \nu_\mu + \bar{\nu}_e \ .$$

Muons mostly persist until ground level because of their relativistic speeds and relatively long lifetimes (the lifetime of a muon is $\sim 2.2 \times 10^{-6}$ s).

3.1.2 Electromagnetic Shower

Electron-photon cascades can be produced in the atmosphere through the interaction of primary γ rays with atoms in the air. The main air-shower interactions are bremsstrahlung and pair production processes (Figure 3.2).

Bremsstrahlung is the radiation associated with the acceleration of electrons in the electrostatic fields of the nucleus of atoms. The radiation length, X_0 [g/cm^2], is the distance over which the initial energy of a cascade particle is reduced by a factor of 1/e by bremsstrahlung. In atmosphere the radiation length is 37 g cm^{-2}.

The *Pair production* process is one of the main particle production mechanisms in electromagnetic showers. Photons having energies higher than twice the rest mass of an electron (rest mass m$_e$ of an electron is 0.511 MeV, where c=$\hbar$=1) are converted into an electron-positron pair in the presence of a nucleus, which guaranties the energy and momentum conservation. As for bremsstrahlung process, the *radiation length* for the pair production process, X_{pair}, can be defined. If the radiation lengths for pair production and bremsstrahlung for ultra relativistic electrons are compared, it can be found that $X_{pair} \simeq X_0$. This reflects the similarity of the bremsstrahlung and pair production according to quantum electrodynamics. This means that γ-ray induced cascades start to develop in the atmosphere at rather high altitudes (10 - 20 km) above the ground level (the total atmospheric depth is
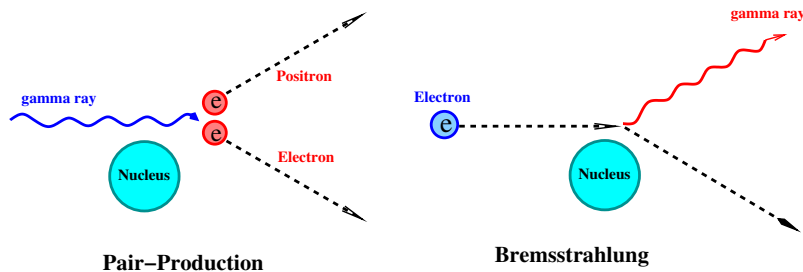
Abbildung 3.2: Main air-shower interactions.

1030 g cm^{-2}). The secondary electrons or positrons produced through pair-production mechanism may interact further with ambient nuclei giving off photons via bremsstrahlung. The photons produced in bremsstrahlung processes may again pair-produce into secondary electrons. Thus finally a cascade of electrons and photons develops in the atmosphere.

While the shower propagates, the number of cascade particles increases, whereas the energy per particle simultaneously decreases. The average energy per particle is given as

$$E \; = \; E_0 \; \exp\left(-\frac{p}{X_0}\right) \;\; , \tag{3.1}$$

where E_0, p, and X_0, are the initial energy, the atmospheric depth [g cm^{-2}], and the characteristic radiation length, respectively. The *atmospheric depth* can be expressed in terms of the *atmospheric height*, h, as follows:

$$p(h) \; = \; p_0 \; \exp\left(-\frac{h}{h_0}\right) \;\; , \tag{3.2}$$

where $p_0 = 1030$ g cm^{-2}, and $h_0 = 8$ km. The cascade grows exponentially and finally reaches its maximum of the order of 10^3 particles for a 1 TeV γ-ray-induced shower. The *shower maximum* occurs at the atmospheric height between 7 and 10 km above the sea level.

At further stages of the cascade development the ionizing collisions with atomic electrons becomes a dominant process for the remaining cascade particles. The ionization depends mainly on the electronic binding energy of atoms in the absorbing material (i.e. the air) and not on the energy of the cascade particle. The critical energy, E_c, at which the radiation loss equals the collision loss is $\sim$80 MeV for air. For cascade particles with energies below E_c the collision-ionization loss becomes dominant over the radiation loss.
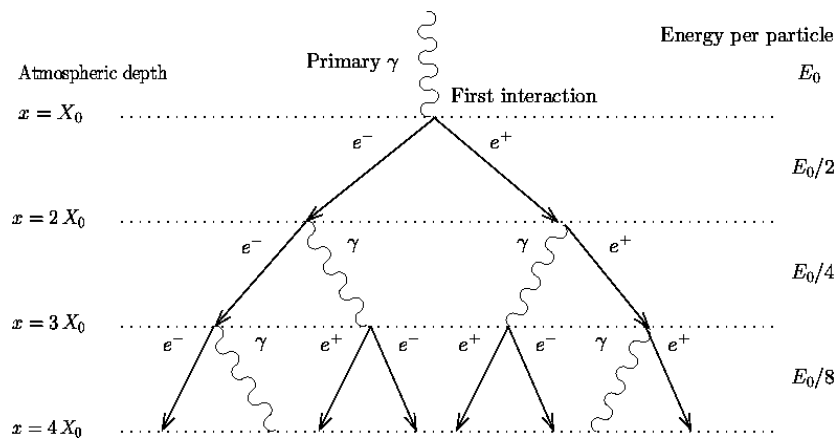
Abbildung 3.3: A model of electromagnetic shower according to Heitler [85]. The figure is taken from [21].

The small transverse momentum of the secondary electrons in γ-ray showers cause the electromagnetic cascades to be beamed along the direction of the primary photon. Multiple Coulomb-scattering of cascade electrons determine the lateral distribution of the shower. The radial spread is determined by the radiation length and the angular deflection per radiation length at the critical energy. This spread is of order one Moliere unit $X_M = 21(X_0 E_c) \simeq 9.6$ g cm^2. Therefore, the shower particles are moving within a cone around the shower axis. This cone has a radius of 80 - 120 m at sea level, and it contains 90% of the total energy of the shower.

The *Heitler model* ([85]) is a simplified picture (Figure 3.3) of the longitudinal shower development. According to this model, the electromagnetic cascade begins with pair-production and continues in the second step with bremsstrahlung. This two-step process repeats itself until the critical energy, E_c, is reached. After that the production processes begin to diminish because of lack of energy. Therefore, it is expected that the number of particles produced in the second step is doubled. As a result, the total amount of particles in the shower is

$$N = 2^n \ , \tag{3.3}$$

after n radiation lengths. At each step the energy is equally distributed between the secondary particles. So, the energy of the shower particles after n radiation lengths can be expressed as follows

$$E_n = E_0 \, 2^{-n} \ , \tag{3.4}$$

which is illustrated in Figure 3.3. It was assumed that after n$_{max}$ radiation lengths the energy drops down to the critical energy, E$_c$. The maximum

number of radiation lengths, n_{max} is thus

$$n_{max} = (\ln 2)^{-1} \ln \left(\frac{E_0}{E_c} \right) \ . \tag{3.5}$$

Using Equations 3.3 and 3.5, the maximum number of particles, N_{max}, produced after n_{max} radiation lengths can be found as

$$N_{max} \approx \frac{E_0}{E_c} \ , \tag{3.6}$$

where $(1/3)N_{max}$ are photons and $(2/3)N_{max}$ are electrons and positrons.

The position of the shower maximum in the atmosphere can be found in terms of n_{max} and the radiation length X_0, which is given as

$$X_{max} = n_{max}X_0 \ . \tag{3.7}$$

Substituting Equation 3.5 into Equation 3.7 the atmospheric depth of shower maximum can be deduced as

$$X_{max} = \frac{X_0}{\ln 2} \ln \left(\frac{E_0}{E_c} \right) \ . \tag{3.8}$$

Using Equation 3.6, and Equation 3.8, one can also show

$$X_{max} = \frac{X_0}{\ln 2} \ln \left(N_{max} \right) \ . \tag{3.9}$$

The relation of number of particles to the atmospheric depth for showers with different energies is given in Figure 3.4.

Although the simplified shower model by Heitler explains the basic properties of the shower rather well, a more detailed description of the shower differs from this model. It is known as the *Nishimura-Kamata-Greisen-Formalism.* More detailed theory of longitudinal shower development can be found in [76].

3.1.3 Differences between Hadron- and Gamma-ray Induced Air-showers

The air-showers generated in the energy range from 100 GeV to 10 TeV are dominated by hadronic showers. In order to select the small number of γ-ray induced air showers from the overwhelming background of proton showers the longitudinal and lateral profiles of showers must be studied in detail.

- Comparing the characteristic radiation length of electromagnetic interactions ($\sim$37 g/cm^2) with the interaction mean free path of the protons ($\sim$80 g/cm^2), it can be concluded that the initial hadronic interactions take place on average deeper in the atmosphere than the initial γ-ray interactions.
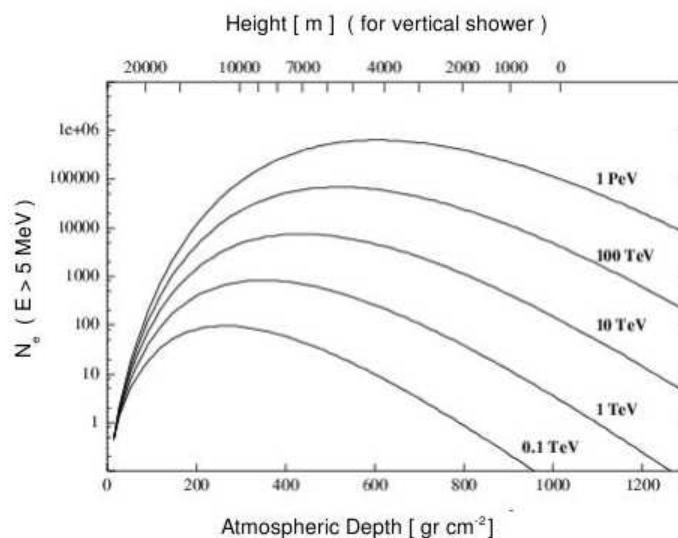
Abbildung 3.4: The dependency of number of electrons with energies higher than 5 MeV for γ-ray showers at different energies to the atmospheric depth. The atmospheric depth corresponds to a certain height of shower maximum, which is given at the upper part of the histogram. Figure taken from [25].

- The longitudinal extension of hadronic showers is larger due to the decays of pions.

- The secondary particles produced by strong interactions and weak decays gain higher transversal momenta resulting the lateral extension of the hadronic showers to be larger compared to the electromagnetic showers. Figure 3.5 shows a comparison between the simulated lateral distribution of a 300 GeV γ-induced shower, and a 1 TeV proton-induced shower.

- Only hadronic showers with three-fold energy obtain the same number of particles as γ-ray showers.

3.2 Cherenkov Radiation from Air-showers

Cherenkov radiation is emitted when a charged particle moves through a transparent medium with a velocity greater than the speed of light in that medium; This phenomenon was first observed around 1910. The first detailed studies were done by Cherenkov, after whom the effect is named, between
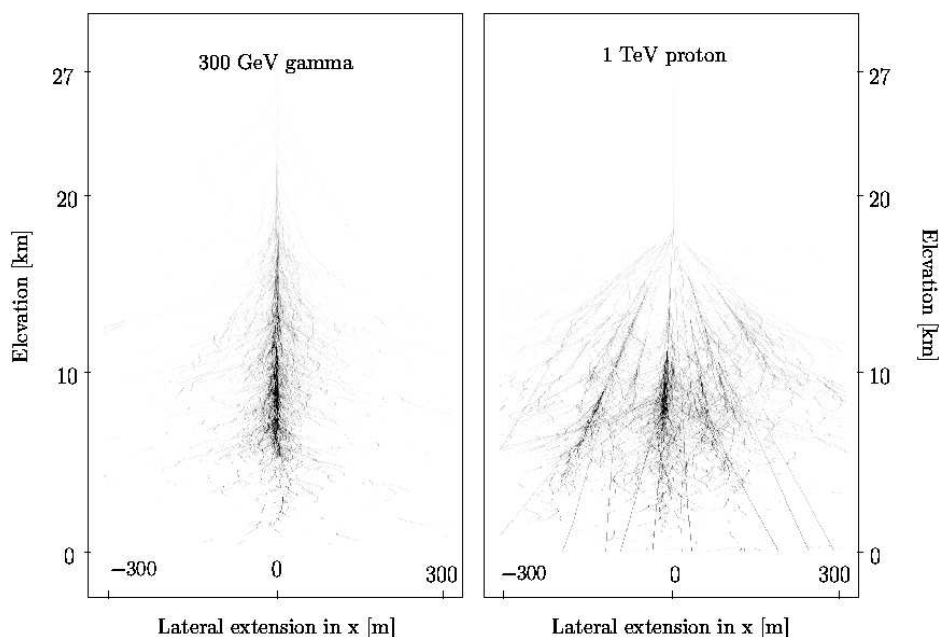
Abbildung 3.5: Simulated data ([24]) is used to show the comparison of the longitudinal development of a 300 GeV γ-ray-induced shower (left plot) and a 1 TeV proton-induced shower (right plot). Picture taken from [21].

1934 and 1938. The charged particles in the EAS are moving in the atmosphere at relativistic velocities that exceed the speed of light in air. As a result Cherenkov light is emitted from the shower, which has a characteristic emission profile depending on type and energy of the primary particle. This light reaches the ground level, where it can be observed with ground-based detectors.

3.2.1 Production of Cherenkov Radiation

When an electron with relativistic velocity v_e moves in a dielectric medium of refractive index n, it disturbs the neutrality of the atoms in its immediate vicinity inducing polarization. After the particle passed by, the atoms relax back into their initial state and while they do so they emit pulses of electromagnetic radiation. Cherenkov radiation occurs, when these pulses are emitted coherently. Considering that the speed of light in this dielectric medium is c_n and when $v_e < c_n$, the wavefronts emitted at different points from atoms along the path of the electron never intersect. So, interference can not occur. This case is illustrated in Figure 3.6 (a). However, if $v_e > c_n$, then the wavefronts do overlap and constructive interference can take place, which is
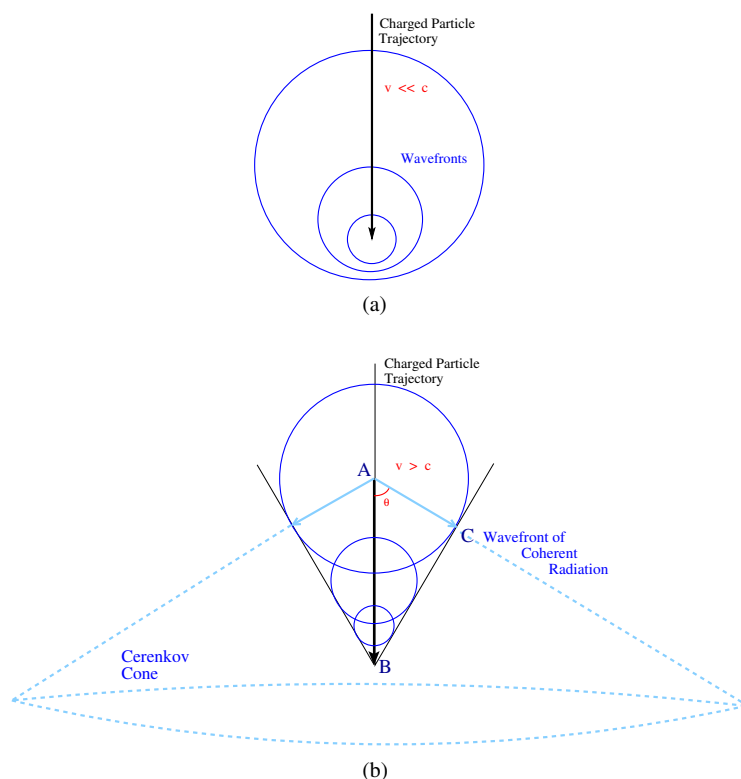
Abbildung 3.6: Cherenkov Light Emission. Upper plot shows the case, when the particle is moving in the medium with a speed (v_e) less than the speed of light in that medium (c_n). So, the wavefronts emitted by atoms along the particle's track do not intersect. The plot at the bottom shows the case $v_e > c_n$. From the interference of the wavefronts Cherenkov light is produced.

shown in Figure 3.6 (b). The wavefronts produce a large conical wavefront centered at the electron's trajectory, with an opening angle θ. This emission is called the *Cherenkov emission*, and the cone is called the *Cherenkov cone*.

The *Cherenkov angle, θ,* can be determined using *Huygen's principle*, which can be derived from Figure 3.6 (b). For a wavefront emitted by atom A to be coherent with a wavefront emitted by atom B, both wavefronts must be emitted at the same angle θ with respect to the trajectory of moving particle. If the electron travels from A to B within a time interval Δt with a velocity $v_e = \beta \cdot c$, and the wavefront emitted at A travels to the point C within the same time interval Δt, where the retarded velocity of light in the medium with refractive index n is v_n ($= c \ / \ n$), then the following relations

can be written

$$AB \;=\; \beta\, c\, \Delta t \quad,\quad AC \;=\; \frac{c}{n}\, \Delta t \quad. \tag{3.10}$$

Using both relations in Equation 3.10, the basic *Cherenkov relation* can be obtained as follows

$$\cos(\theta) \;=\; \frac{1}{\beta\, n} \;=\; \frac{c}{v_e\, n} \;=\; \frac{AC}{AB} \quad. \tag{3.11}$$

Equation 3.11 gives the threshold velocity as

$$\beta_{min} \;=\; \frac{1}{n} \quad. \tag{3.12}$$

Using Equation 3.12 the minimum energy required for a particle to produce Cherenkov emission can be computed as

$$E \;=\; \gamma\, m_0\, c^2 \quad,$$

$$E_{min} \;=\; \frac{m_0\, c^2}{\sqrt{1 \;-\; \beta_{min}^2}} \quad. \tag{3.13}$$

E_{min} is ~21 MeV for electrons in air. When the particle moves with extreme relativistic velocities, then $\beta \;\rightarrow\; 1$ is case, in which the angle of Cherenkov emission maximal

$$\theta_{max} \;=\; \cos^{-1}\left(\frac{1}{n}\right) \quad. \tag{3.14}$$

The Cherenkov angle is typically ~1.3° in air, but it has a dependence on air pressure (Equation 3.14 and Equation 3.15).

3.2.2 Atmospheric Cherenkov Light

When a shower propagates through the atmosphere, Cherenkov radiation is emitted by the secondary particles such as electrons and positrons. These secondary particles are produced in different atmospheric layers, the density of which changes continuously with the height above the sea level. The dependence of the refractive index, n, on the height, h, can be approximated by

$$n(h) \;=\; 1 \;+\; \eta_0\, \exp\left(\frac{h}{h_0}\right) \quad, \tag{3.15}$$

where $\eta_0 \;=\; 0.00029$ and $h_0 = 8400$ m.
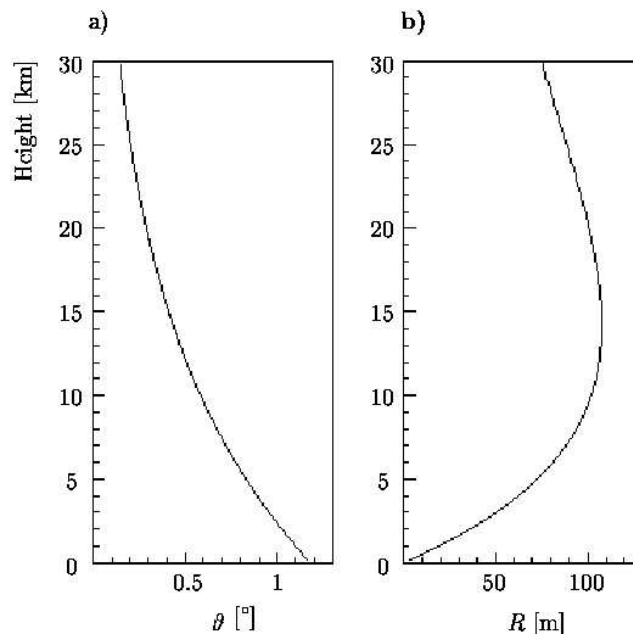
Abbildung 3.7: Parameters of the Cherenkov light emission from the shower. In plot (a), the dependency of the Cherenkov emission angle, θ, to the height of the shower maximum is shown. In plot (b), the height of the shower maximum is plotted against the radius of the Cherenkov ring on the ground. Figure taken from [21].

Lateral and Longitudinal Distributions

According to Equations 3.13, 3.14, and 3.15 from the previous Section, the lower the altitude is, the lower is the threshold energy (E_{min}), but the higher is the Cherenkov angle, θ. For a TeV γ-ray-induced air-shower, at the height of shower maximum the threshold energy for electrons is around 50 - 55 MeV. The secondary electrons and positrons emit Cherenkov light even beyond the shower maximum until their energies fall below an absolute threshold of 21 MeV at the sea level. It can be easily calculated that from 15 km a.s.l. down to the sea level the Cherenkov emission angle, θ, varies from 0.5° to 1.38°, respectively. The dependency of Cherenkov angle on the emission-height is shown in Figure 3.7 (a).

For electromagnetic showers, the Cherenkov light emitted by all shower particles reaches the ground within a ring of radius given by

$$R = \frac{(h - H)}{\tan \theta} \quad , \tag{3.16}$$

where h and H are the height of shower maximum and the observation level,

respectively. The relation between the height of shower maximum and the radius of the *Cherenkov ring* is shown in Figure 3.7 (b).

The lateral extension of a shower varies along the longitudinal shower profile. The deeper the shower penetrates into the atmosphere, the larger it expands laterally due to the multi-scattering in the atmosphere (see Section 3.1.2). This lateral extension of the shower results in the specific distribution of the Cherenkov light at the ground, which is also called as *Cherenkov light pool*. In general, the spread of shower particles is wider for more energetic showers, because the shower maximum occurs later in time and deeper in the atmosphere. Beyond the shower maximum, the γ-ray-induced showers begin to die away and to shrink in its lateral spread consequently. The hadronic showers, on the other hand, fade more slowly, but at the same time often show a heterogeneous, and asymmetric lateral profile, which is due to individual muons.
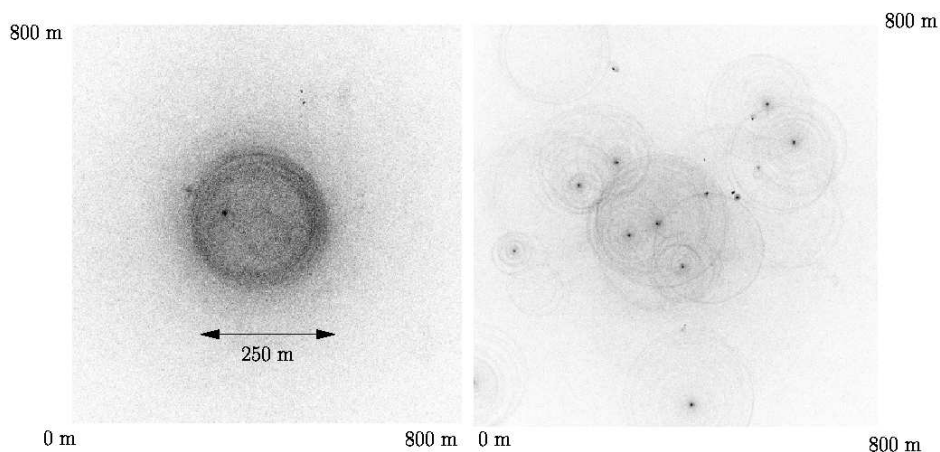
Abbildung 3.8: The Cherenkov light distributions for a 300 GeV γ-ray-induced shower (left plot) and a 1 TeV proton-induced shower (right plot) as seen on the ground. Picture taken from [21].

When Cherenkov light from γ-ray showers is focused using a reflector with a camera, it can be seen that the recorded image bear the general characteristics of the shower profile. Thus the images are compact, and uniform for γ-ray showers, while the proton images are non-uniform and irregular in shape. Also muon rings appear often in the images of proton showers.

Time Profiles

The time of development of an air-shower from the first interaction until it dies in the atmosphere is about 50 μs, [22]. Cherenkov light flashes are very

short in duration, which is for a 1 TeV γ-ray induced-shower $\sim$5 ns and each flash yields about 100 photons per m^2 within 100 m of the shower axis.

Extinction of Atmospheric Cherenkov Light

As the Cherenkov light propagates through the atmosphere, it can be partially scattered or absorbed. This causes systematic limitations in its detection. Light extinction is characterized by the corresponding *extinction coefficient* α. The exponential loss of intensity due to the light extinction can be formulated as follows

$$I(x) \;=\; I_0 \; \exp\left(-\alpha\, x\right) \; . \tag{3.17}$$

This coefficient, α, depends on the wavelength range $\Delta\lambda$ covered by the Cherenkov light spectrum. The Cherenkov light spectrum from the air-showers peaks around 400 nm, i.e. in blue visible wavelength region, but has non-negligible contributions in UV and IR as well.

The basic types of scattering and absorption processes for Cherenkov light are as follows:

- *Rayleigh scattering:* This type of scattering is dominated by polarizable molecules like oxygen and nitrogen, which have sizes significantly smaller than the wavelength of Cherenkov light.

- *Mie scattering:* This denotes the interactions of Cherenkov light with such targets as dust molecules and aerosols, the size of which is comparable with the wavelength of the Cherenkov light.

- *Absorption by Ozone Molecules:* The Cherenkov light in a wavelength range of 200 - 320 nm is almost completely absorbed by the ozone and aerosols in the higher atmosphere.

The contribution from the extinction coefficients of the independent processes mentioned above (Rayleigh and Mie scattering, and the absorption processes) to the overall extinction coefficient, α, as a function of the altitude at certain wavelengths is as follows:

$$\alpha \;=\; \alpha_{Rayleigh} \;+\; \alpha_{Mie} \;+\; \alpha_{Ozone} \; .$$

3.3 Imaging Atmospheric Cherenkov Technique

A Cherenkov flash from an air shower lasts roughly $\sim$5 ns. Using a simple light detector composed of a single photomultiplier tube (PMT) mounted at

the focus of a reflector having a small collection area ($\sim$2 m^2) and coupled to fast pulse counting electronics can be used to measure the Cherenkov light flashes, [167].

A Cherenkov flash from an air-shower, which is mostly a hadronic shower, is measured as the light signal S (in number of photoelectrons) if the integration time, t, of the photomultiplier pulse counting system is greater than the duration of the Cherenkov light flash. The measured light signal S is

$$S \; = \; \int_{\lambda_1}^{\lambda_2} \; F^C(\lambda) \; \varepsilon(\lambda) \; A \; d\lambda \; , \tag{3.18}$$

where $F^C(\lambda)$ is the Cherenkov photon flux, A is the mirror collection area, $\varepsilon(\lambda)$ is the response curve of the photomultiplier tube, and λ_1 and λ_2 are the minimum and maximum wavelengths of the PMT response.

$$F^C(\lambda) \; \propto \; E(\lambda) \; T(\lambda) \; , \tag{3.19}$$

where $E(\lambda)$ is the Cherenkov light emission spectrum of the shower, $T(\lambda)$ is the atmospheric transmission function.

The Cherenkov light pulse must be detected above the fluctuations in the night-sky background in the time interval t. The night-sky background is given as

$$B \; = \; \int_{\lambda_1}^{\lambda_2} F^B(\lambda) \; \varepsilon(\lambda) \; t \; A \; \Omega \; d\lambda \; , \tag{3.20}$$

where Ω is the solid angle of observation and $F^B(\lambda)$ is the night-sky background flux. A Cherenkov light flash of a 1 TeV γ-ray (having a typical duration of $\sim$5 ns) produces about 100 photons per m^2 within 1°. In 5 ns, only 1 - 2 photons per m^2 are detected from the night-sky background within 1°, [110]. The signal to noise ratio is

$$\frac{S}{\sqrt{B}} \; = \; \frac{\int_{\lambda_1}^{\lambda_2} \; F^C(\lambda) \; \varepsilon(\lambda) \; A \; d\lambda}{\sqrt{\int_{\lambda_1}^{\lambda_2} F^B(\lambda) \; \varepsilon(\lambda) \; t \; A \; \Omega \; d\lambda}} \; , \tag{3.21}$$

The smallest detectable Cherenkov light pulse (or the minimum shower energy, E_{min}) is inversely proportional to the signal to noise ratio ([167]). In order to optimize E_{min}, the following conditions are required:

- The integration time, t, can be adjusted as close as possible to the duration of the Cherenkov pulse,

- the collection area, A, should be maximized,

- the quantum efficiency of the PMT, $\varepsilon(\lambda)$, should be maximized.

Apart from the night-sky background, the efficiency in detection of the γ-ray showers is affected by the overwhelming background of hadron-induced air-showers. To discriminate between the γ- and proton showers advanced detectors and analysis methods have been developed. More details on the early works on the imaging atmospheric Cherenkov technique can be found in [90], [165], [166], [40]. The detectors nowadays are telescopes have larger mirror collection areas and the camera consists of a group of PMTs connected to fast electronics. The camera, which is segmented into PMTs allows a more precise image of the shower can be detected in the camera.

3.3.1 Two-Dimensional Angular Image

Parallel approaching Cherenkov light rays having the same two-dimensional Cherenkov angle $\Theta = \{\theta_x, \theta_y\}$ are focused onto the same point in the camera. For example, in Figure 3.9 (a) for a coordinate system, where the telescope axis coincides with the z-axis, the point with coordinates (x_s, y_s, z_s) is imaged onto a point in the camera with coordinates $(-x_c, -y_c, F)$, where F is the focal length of the telescope dish. The minus sign in front of x_c and y_c indicates the reflection of the light by the mirror. Therefore, the angular distribution of the light coming from the shower can be mapped into the camera focal plane, where the following relations hold

$$\theta_x \approx \tan\theta_x = \frac{x_s}{z_s} = -\frac{x_c}{F} \ , \ \ \theta_y \approx \frac{y_s}{z_s} = -\frac{y_c}{F} \ ,$$

$$\Theta \approx (\theta_x^2 + \theta_y^2)^{1/2} \ . \tag{3.22}$$

Equation 3.22 can be written in matrix form as follows

$$\begin{pmatrix} \theta_x \\ \theta_y \end{pmatrix} = -\frac{F}{z_s} \begin{pmatrix} x_s \\ y_s \end{pmatrix} \ . \tag{3.23}$$

Assuming that the Cherenkov light is emitted isotropically around the shower axis, Cherenkov light emitted at each point along the shower axis is imaged onto the camera. In Figure 3.9 (b) the light-ray number 1 is emitted at the top of the atmosphere, and it is focused close to the camera center,
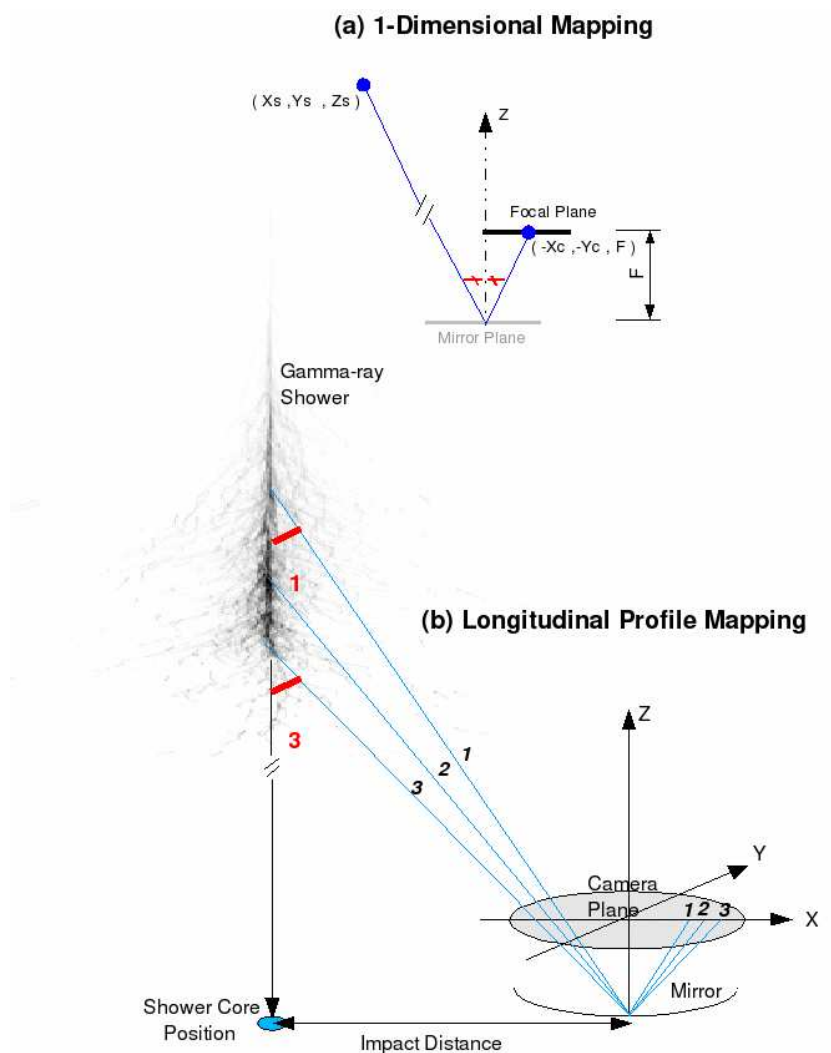
Abbildung 3.9: In one-dimensional mapping (a), a Cherenkov light-ray emitted from a point on the shower axis having coordinates x_s, y_s, z_s is mapped onto the camera plane as $-x_c, -y_c, F$, where the minus sign is due to the reflection by the mirror. Similarly, all emission points along the shower axis are mapped (b) into the focal plane of the telescope., where the point higher in the atmosphere is mapped closer to the camera center.
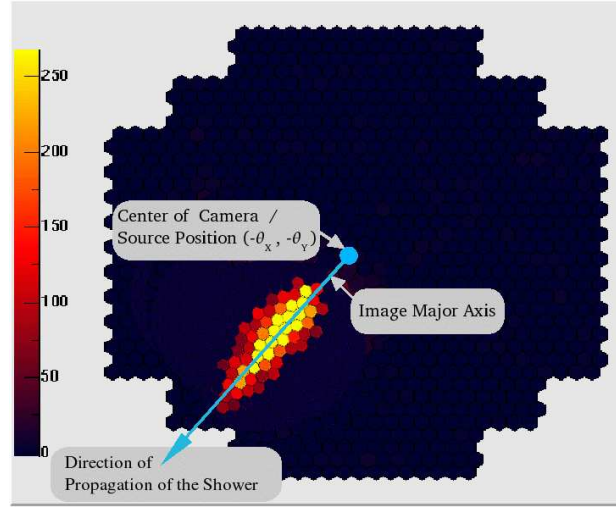
Abbildung 3.10: For this image in the camera, the direction of the γ-ray induced shower was parallel to the telescope axis. Therefore, the expected source position on the image major axis is at the center of the camera. The shower axis pointing to the edge of the camera represents the position of Cherenkov light that would be emitted close to the impact position of the shower on the ground. Color code represents the intensity in units of photo-electrons..

whereas the light-ray number 3 is emitted at the tail of the air-shower, and it is focused away from the center of the camera. The image of the shower axis in the camera is a straight line pointing toward the shower core position on the ground (Figure 3.10). Therefore, the orientation of the image of the shower axis indicates the shower direction with respect to the telescope axis.

A substantial amount of Cherenkov light from a γ-ray shower is emitted around the shower maximum. The relation between the height of the shower maximum and the impact distance (Figure 3.9) can be derived from the geometry using the Cherenkov angle

$$\Theta \sim \tan \Theta \;=\; \frac{R}{H_{max}} \;\;, \tag{3.24}$$

where R is the the core position of the shower on the ground, and H_{max} is the height of the shower maximum.

In Figure 3.9 (b), if the light-ray number 3 is emitted with a Cherenkov angle of Θ_3 and the light-ray number 1 is emitted with an angle of Θ_1, the difference $\Delta\Theta = \Theta_3 - \Theta_1$ gives the longitudinal spread of the image in the

camera. For increasing distances of R, $\Delta\Theta$ increases causing the length of the image to increase and the image to shift toward the edge of the camera. For each point along the longitudinal emission axis, there is a certain lateral profile of the shower. The lateral extension of the shower is represented by the width of the image in the camera. The intensity distribution in an elliptical image in the camera is usually symmetric around shower axis, although the longitudinal profile is mapped asymmetrically onto the camera plane due to the $1/z$ dependence of Equation 3.23, which causes the images to have a comet-like shape with a steep rising edge and with a relatively long tail toward the edge of the camera.

The form, position, and orientation of the images detected by the camera can be further analyzed to determine an exact shower profile. This enables to differentiate shower types and eliminate most of the background.

Kapitel 4

The H.E.S.S. Experiment

4.1 Overview

The H.E.S.S. experiment is a system of four imaging atmospheric Cherenkov telescopes designed for γ-ray astronomy in the range from 100 GeV up to TeV energies. The acronym H.E.S.S. stands for *High Energy Stereoscopic System*. The stereoscopy is achieved by simultaneous observations of air-showers from different viewing angles. The stereoscopic approach provides a significant rejection of background and a good angular resolution.

The H.E.S.S. telescopes (Figure 4.1) are located in the Khomas Highland of Namibia, on the Farm Goellschau, about 100 km south-west of Windhoek. The exact location is 23°16'18" S and 16°30'00" E at 1800 m a.s.l.. This location in the southern hemisphere gives the possibility to observe part of the Galactic Plane and the galactic center. Namibia has a clear sky, mostly cloudless nights and a good climate suitable for γ-ray astronomy with the IACTs.

The first of the four telescopes of the H.E.S.S. system in Phase-I started operation on June 2002 and the second telescope started working in March 2003. The system is fully functional since the beginning of 2004. A later expansion of the system (H.E.S.S. system Phase-II) is foreseen.

Each of the H.E.S.S. telescopes consist of two main parts: the mechanical and optical structures (dish, mirrors, etc.), and the electronic components (cameras, etc.). This Chapter includes a brief overview of the main components of the H.E.S.S. array. A more detailed review is given in [97].

Abbildung 4.1: The H.E.S.S. telescopes fully operational since 10th of December 2004.

4.2   Design of the System and Telescopes

The four telescopes of the Phase-I H.E.S.S. array are placed at the corners of a square of 120 meters (m) side length. Each H.E.S.S. telescope has a steel dish designed in a hexagonal shape, which is supported by an *Altitude-Azimuth (Alt-Az) mount.* Figure 4.2 (left) shows a technical drawing of such type of mount. This mount rotates on a 15 m diameter rail. *Friction drives* acting both on azimuth and elevation drive rails provide a positioning speed of 100 ° min^{-1}. The tracking precision is about 30", [32].

4.3   Reflector

The reflector of a H.E.S.S. telescope has 15 m focal length and 13 m diameter, which makes up a total area of $\sim$107 m^2. The design of the reflector is *Davies-Cotton* [53]. In Davies-Cotton design the dish for mirror mounting is spherical and has a radius of curvature half that of the individual facet-mirrors. There are 380 facet-mirrors made of alumnized glass with a quartz coating (initial reflectivity around 85%), each of which has a diameter of 60 cm. The images collected by each of these facet-mirrors are focused onto a plane at the center of curvature of the telescope's dish. The Davies-Cotton design has many advantages in γ-ray astronomy, for example, both *on-axis (object of interest is along the axis of the telescope)* and *off-axis* aberrations are small, [117]. The alignment of the mirrors is simple, because all the facet-mirrors are identical in construction and optical characteristics. The major disadvantage is that it is not *isochronous.* In an an-isochronous design, there is a spread of arrival times of the light in the focal plane (e.g. the temporal spread is about 6 ns for a telescope with a focal length of 10 m, [110]).
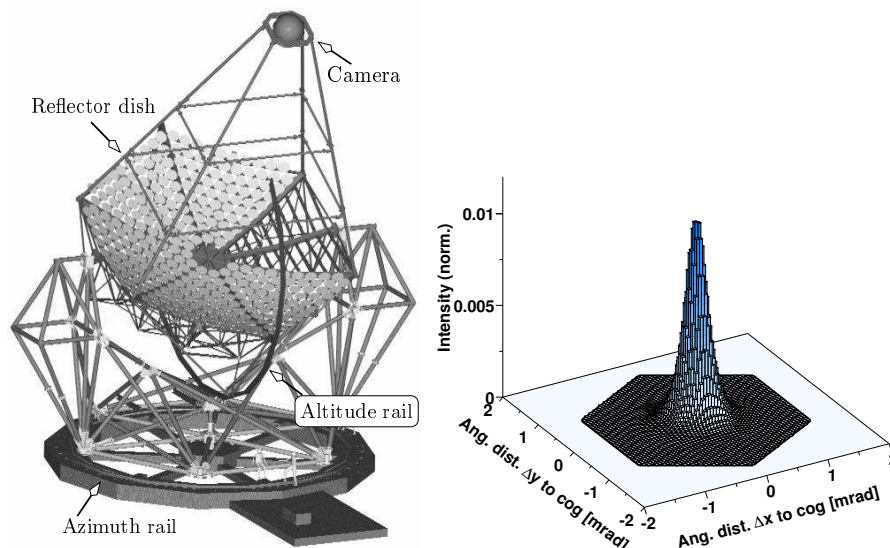
Abbildung 4.2: (Left) The structure design of the H.E.S.S. telescope. (Right) On-axis intensity distribution of a star on the closed camera lid after alignment of the mirrors. The hexagonal border is the size of a pixel in the camera. Figure taken from [50].

4.4   Pointing Accuracy

The accuracy of the pointing of a telescope depends on the mirror alignment accuracy, the tracking accuracy, and the precision of corrections for misalignments and deformations of the structure of a telescope.

The mirror alignment procedure is based on viewing the image of a star, which is reflected by facet-mirrors onto the closed lid of the telescope's camera, [50]. The reflected image positions (spots) are recorded by a lid-CCD camera, which is mounted at the center of the telescope's dish (Figure 4.3). Then each of the facet-mirrors are moved one by one, changing the location of the corresponding spot on the lid; the displacement is recorded every time. With the help of this recorded data, the spot can be focused into a single position at the center of the camera lid. This procedure guaranties that a point-like source at infinite distance to be imaged on the focal plane of the telescope. The *point spread function (PSF)* shown in Figure 4.2 (right) is the on-axis intensity distribution of a star on the camera lid after alignment. It can be seen that the distribution is symmetrical and the width is smaller than the size of a PMT pixel, which is about 0.16°. On the optical axis, an RMS-width of ∼48" is measured. When this accuracy of aligned mirrors is combined with the tracking precision (≈30"), the telescope points
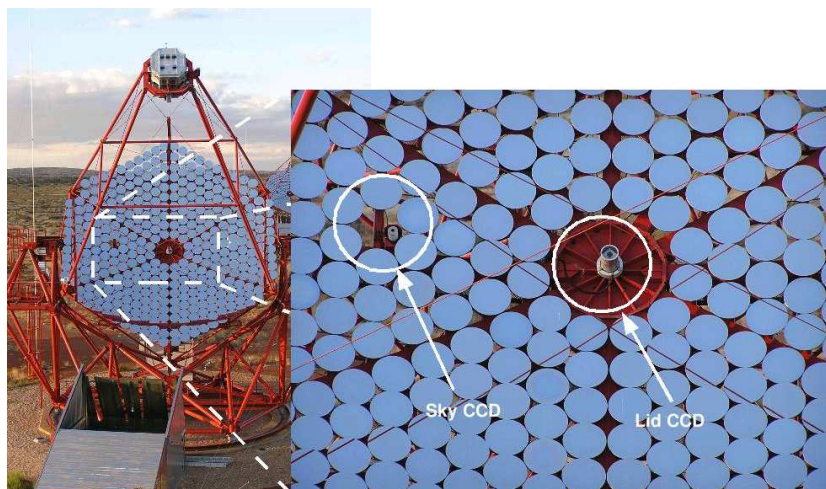
Abbildung 4.3: The position of lid-CCD and sky-CCD on the dish indicated by white circles. The lid-CCD is mounted in the center of the telescope dish, and the sky-CCD can be seen on the left of the lid-CCD.

to a source with a combined accuracy of $\sim$60". Detailed information on the mirror-alignment procedure can be found in [26], [51]

The mis-pointing of the telescopes due to the mechanical imperfections should be corrected in order to achieve an arc-second level of resolution. The mechanical imperfections are the reproducible errors such as bending of the structure under gravity, as well as the irreproducible effects like bending due to wind. To predict the reproducible errors positions of a sample of bright stars are recorded (while the lid of the camera is closed) by the lid-CCD as a function of azimuth and altitude. A detailed mechanical model is fit to this data so that given a pointing of the telescope the model returns the expected mis-pointing, [69]. Without any model corrections, the raw mechanical pointing accuracy is about 60" (two-dimensional RMS), after the correction, a pointing precision of 20" RMS is achieved. This accuracy can be improved by other techniques using the sky-CCD (shown in Figure 4.3). These techniques are still under study, [70].

4.5   Camera

The camera of a H.E.S.S. telescope consists of 960 pixels (PMTs) each having a diameter of $0.16°$, which results in an overall field of view of $5°$. All the signal processing, triggering, and digitization processes run within the camera body.
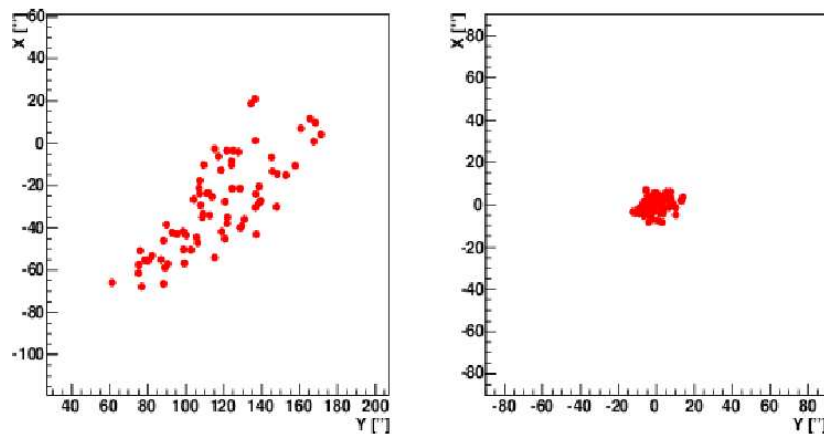
Abbildung 4.4: After mirror alignment a second step correction due to the mis-pointing of the telescope is done. (Left) The spots of the stars on the camera plane before applying any pointing-model have a RMS of about 60". After applying the pointing corrections a pointing precision of less than 20" is obtained. Figure taken from [70].

The *photo-multiplier tubes (PMTs)* of type *Photonis XP2960* consist of a photo cathode enclosed with μ-metal shielding, which prevents the photo-electrons to be deflected by the Earth's magnetic field and plastic casing. The material, of which the PMT's window is made affects the sensitivity of the PMT. In order to be able to detect Cherenkov light, the transparent range has to be above 250 nm. The PMT's used in the H.E.S.S. experiment have windows made of borosilicate glass. A PMT acts as a combination of a simple photo-cell with a high-gain amplifier. The gain for each PMT is 2×10^5. Operating voltages for the PMTs are supplied by DC-DC converters integrated into each PMT base with active stabilization for the last four dynodes for best linearity, [97]. The *quantum efficiency,* Q_{eff} can be expressed as the number of electrons emitted by the cathode divided by the number of photons hitting the PMT's window. The quantum efficiency depends on the material that the window and the cathode is made of. The maximum Q_{eff} is around 25% for the wavelength range from 390 to 420 nm, [101].

The collection of light that is reflected from the telescope's mirrors onto the camera is improved by *Winston cones*, which are mounted on top of the pixels in the camera. These light-guiding cones are used to salvage photons, which would otherwise be lost in the space between pixels. They are also used to select light that comes from the mirrors of the telescope and shield against large impact angle scattering light etc..

16 pixels are grouped in a *drawer unit*. There are 60 drawers in each

Abbildung 4.5: The H.E.S.S. Camera with the lid opened.

camera. The drawers can be inserted from the front side of the camera body and have connectors to power, readout bus, and trigger bus at the backside. Apart from the PMTs, each drawer contains two *acquisition cards*, each of which is connected to 8 PMTs. The incoming signals from the PMTs are measured across a resistor, R_{PM}, and amplified into the acquisition channels. In order to observe the showers within an energy range from 40 GeV to 20 TeV or higher, a dynamical range of 1 - 2000 photoelectrons (ph.e.) is required. With only one channel per PMT it is not possible to cover this range. Therefore, for each pixel there are two *acquisition channels* that have different gains: the *high-gain (HG) channel* is used to detect signal charges up to 200 ph.e., and the *low-gain (LG) channel* covers the range from 10 to 1600 ph.e.. For the analysis, the linear range (Figure 4.6) of both of the channels is used.

Apart from the acquisition channels, each acquisition card has a *trigger channel* and four *Analog Ring Samplers (ARS)s*, each of which contain 128 capacitor cells. The ARS plays an important role in the camera's readout process. Analog signals arriving from the (HG and LG) acquisition channels of a PMT are sampled in the ARS. This is done by storing the analog voltage levels in a ring buffer of 128 capacitor cells with a rate of 1 GHz (i.e. each cell is stored within 1 ns). Sampling of analog signals continues until a *camera trigger* signal arrives. Usually it takes 70 ns that a trigger signal is formed (see also Section 4.6). In each ARS the width of the *read-out window*, where the Cherenkov signal is expected, is normally 16 cells long. Only the analog signal from this read-out window is digitized by an *Analog to Digital Converter (ADC)* with a specific conversion factor of 1.22 mV per ADC-counts ([88]) and
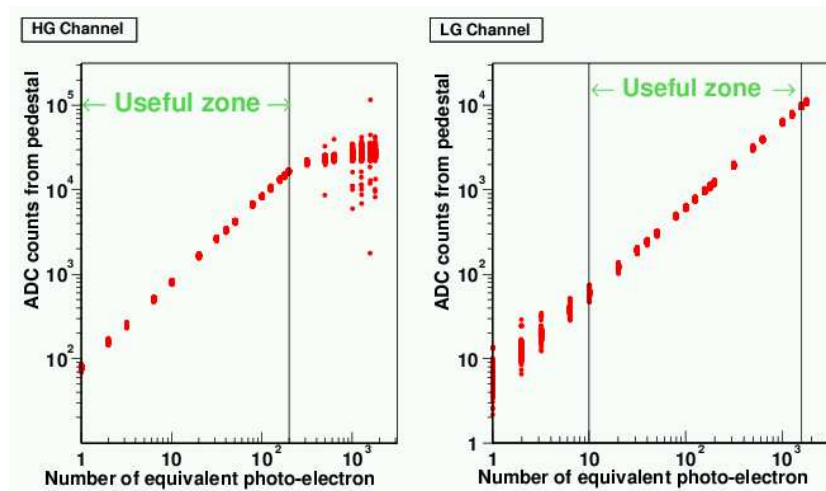
Abbildung 4.6: (Left) Linearity of the high-gain (HG) channel and (right) linearity of the low-gain (LG) channel. Figure taken from [88].

sent to a *Field Programmable Gate Array (FPGA)* that allows two different modes of recording: the *charge-mode* and the *sample-mode*. In sample-mode ADC-values stored in each cell of the read-out window are recorded. In the charge-mode the ADC-values of all cells of the read-out window are summed and recorded. The sample-mode is used in calibration (Section 4.9) of the data, the charge-mode for data-taking, [164].

4.6   Trigger

In the H.E.S.S. experiment simultaneous observation of an air-shower with multiple telescopes is carried out at the hardware level by the *central trigger system (CTS)*. The CTS consists of a *central trigger unit* placed in the control building of the H.E.S.S. array and interface modules located in each camera. The communication between the CTS and interface modules is achieved by an optical fiber link.

The trigger-process consists of two parts: The *camera trigger* and the *central trigger*. The *camera trigger* results from a multiplicity trigger within overlapping *trigger sectors* (Figure 4.7), each having 64 pixels. In a pixel, the *PMT comparator* checks if the number of ph.e. in the signal exceeds a given *pixel threshold, p*, and creates a trigger pulse. The length of the pulse reflects the time the input signal exceeds the threshold. Since typical noise signals rarely exceed the threshold p and result in short trigger signals, the effective resolving time of the pixel coincidence is in the 1.3 to 2 ns range providing
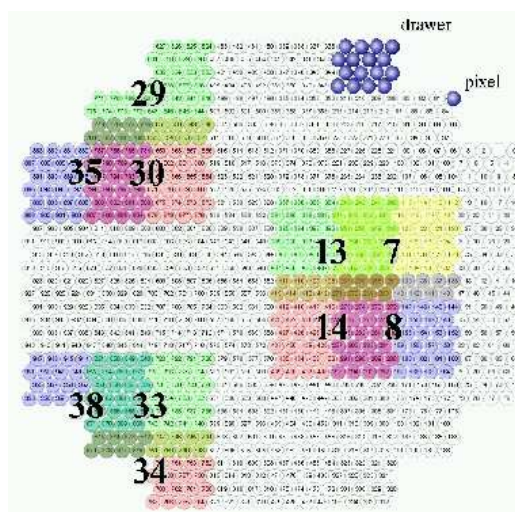
Abbildung 4.7: Each of the H.E.S.S. cameras is divided into 38 overlapping trigger sectors.

a high suppression of random coincidences, [97]. The *camera trigger* occurs by the coincidence of the number of pixels, which have signals above the threshold p, in a trigger sector exceeding an adjustable *sector threshold, q* (usually from 3 to 5 pixels). The time needed to build a trigger signal is 70 ns. Following a camera trigger signal the readout of the camera starts. At the same time, the trigger information of the camera is sent to the CTS.

In the CTS if several telescope triggers coincide within a time window of 80 ns, a *central trigger* signal is send. This signal initiates the readout from the data of the whole array. The CTS assigns an absolute time-stamp to each system-event, which is provided by a GPS clock in the central trigger unit, [65].

4.7   Data Acquisition System

The DAQ system provides readout of the subsystems such as the camera, tracking system, the light pulser systems (used for calibration purposes), the IR radiometer for atmospheric monitoring, the CCD systems used for the pointing corrections, and the weather station. The main data stream is produced by the telescopes' cameras, which generate events with a size of 1.5 kB. Four telescopes generate a maximum data rate of 6 MB per second resulting in ~100 GB of data per observation night. The data rates from the other subsystems are much smaller. The received data is distributed to 15 *Linux farm PCs*, gets processed and stored locally on a RAID-system for

later archiving.

The software package that manages the DAQ is object oriented, and is general enough also to be applied by other similar experiments. The other software packages used are the omniORB ([132]), implementation of the CORBA protocol for the inter-process communication, and ROOT ([145]) for storage and analysis of the data. Furthermore, the shift crew interacts with the DAQ system via a central GUI (Graphical User Interface) providing an access point to the system and direct monitoring of the states of the running processes, [34].

4.8   Observational Modes

Data is taken with the H.E.S.S. telescopes after the Sun sinks 18° below the horizon and data taking is only possible on moonless periods of the night.In the H.E.S.S. experiment, there are two different modes of observation, in which data has been taken. These are the *ON/OFF-mode* and the *wobble-mode.*

In *ON/OFF-mode* there are successive observation runs of *ON-mode* and *OFF-mode.* In an ON-mode observation run, the source position is in the center of the FoV and as a control of this signal region an OFF-mode observation run follows by shifting the center of the FoV 30 minutes in *right ascension (RA).* This is shown in Figure 4.8 (top). The disadvantage of this method is that it needs double the observation time (2×30 min) to get data on the signal region and background region.

In wobble-mode the telescope is focused so that the source position is not in the center of the FoV, but shifted by a specific distance, $\vec{r}$, away in *declination (Dec)* like it is shown in Figure 4.8 (bottom), or in *RA* or in linear combinations of *RA* and *Dec.* The norm of vector $\vec{r}$ is also known as the *wobble radius, r.* The wobble-radius is usually taken as $\pm0.5°$, $\pm1.0°$, or $\pm2.0°$. The duration of a wobble run is 28 min. Both the *signal region* and the *background regions* are extracted from the same wobble-run. Some of the wobble runs (especially of the extended sources covering the regions used for background estimation) are combined with OFF runs. The selection of the signal- and background-regions in wobble runs is explained in detail in Section 6.5.
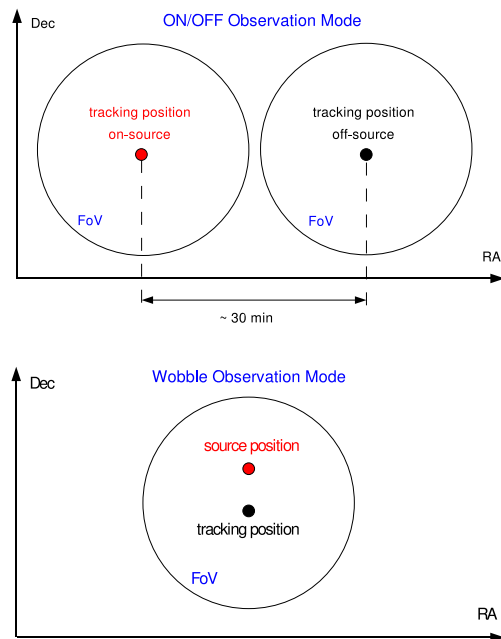
Abbildung 4.8: Main observation modes in the H.E.S.S. experiment.

4.9 Calibration

In order to start to analyze the data, the signal amplitude of each pixel is needed. The *amplitude* is the charge in photoelectrons (ph.e.) induced by light on the PMT.

In order to convert the ADC (Analog-to-Digital Converter) values into physically meaningful values, i.e. photons or ph.e., a source of light having wavelength, pulse duration, and intensity distribution similar to Cherenkov light from the γ-ray showers has to be used to illuminate the PMTs.

Moreover, the homogeneity of the responses from the whole PMT matrix in the camera has to be assured. This is done by *correcting the amplitude* in a pixel by the relative efficiency of this pixel compared to the mean value over the camera. This is known as the *flat-fielding* procedure.

The *calibration* provides the required conversion coefficients from ADC counts to the corrected photoelectrons. It is done by using artificial sources of light like UV-LASERs and LEDs, or by making use of *atmospheric muons*.

The instruments used in calibration are the following:

- *LED flasher*: It is mounted at the center of the telescope dish 15 m away from the camera. The flashers provide a uniform illumination of
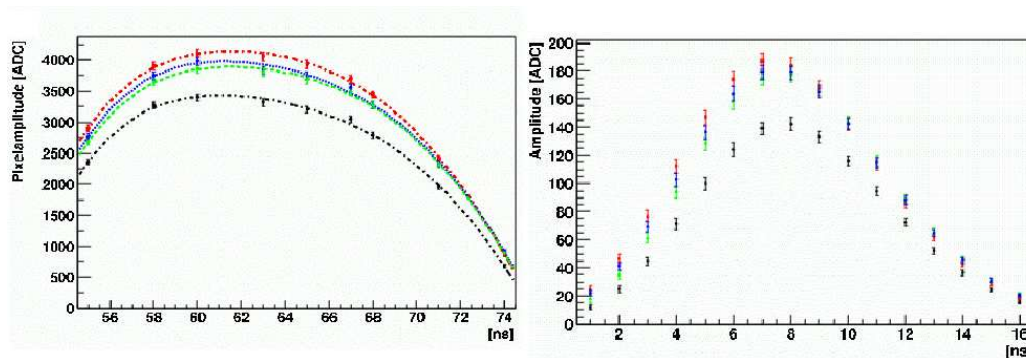
Abbildung 4.9: (Left) The mean pixel amplitude measured as a function of the width of the read-out window, N_d, for the HG-channel. (Right) The position of the mean maximum is shown over the chosen length readout window. Different colors correspond to different pixels. Results for LG-channel looks alike. Figure taken from [101].

the camera up to 10°, which is bigger than the angular size of the camera, and short pulses within a wavelength range from 390 to 420 nm (This range is around the wavelength of the PMT's peak quantum efficiency). The pulse intensity is stable (within 5% RMS), and can be adjusted with 5 different neutral density filters. These filters provide an operating range of 10 to 200 ph.e. The LED flasher has recently replaced a UV-LASER (only on CT3), [14].

- *LED pulser*: The LED pulsers with diffusers are mounted 2 m away from the cameras in the camera shelters. The pulses are created with a repetition rate of 70 Hz.

The main steps taken to calibrate the raw PMT data are summarized below. More details can be found in [114], [88], and [101].

- **Determination of the Read-out Window:** The width of the *read-out window*, N_d, has to be calibrated so that the Cherenkov signal integrated over the readout window is maximized.

  For this purpose, special runs with the LED-pulser (explained above) or with a UV-LASER are taken in *charge-mode* to record the N_d values together with the integrated amplitudes. It is found out that for a specific pulse intensity (~45 ph.e.) of the laser, the read-out window varies between 55 ns and 74 ns, [101]. This can be seen in Figure 4.9 (left) for the HG-channel (LG-channel shows the same behavior). Also a set of runs are taken in *sample-mode* in order to check if the signals are within the calibrated readout window. To achieve this the pulses

sent from the LED-pulser (or laser) have a certain fixed delay in order to center the arrived signal in the readout window. This is shown in Figure 4.9 (right). The mean of the distribution given in Figure 4.9 (left) is roughly 62 ns and this calibrated length of the readout window is used in *observation runs* in data taking.

- **Estimation of Pedestals and NSB:** In the absence of any light, electronics noise creates a narrow Gaussian ADC distribution. The mean of this distribution is the pedestal position. To acquire information on electronic noise, which has a typical value of 0.18 ph.e., some data is taken while the camera lid is kept close and a high-voltage is left on. The pedestal is determined by the base-line voltage of the electronic channels at the input of the ADC. The base-line voltage is ~ -0.9 V, which corresponds approximately to -730 ADC counts for both channels. The typical measured pedestal values range between -13000 and -11000 ADC counts. The pedestal position varies with the temperature of the camera due to seasonal changes. It is found that the pedestal position is shifted by 10 ADC counts/$^\circ$C, [88]. The pedestal value in Figure 4.10 is found to be around -15 ADC counts after the base-line value is shifted to zero.

  During the observation runs, in addition to electronic noise, the pixels are illuminated by the NSB photons, which increase the pedestal width. The pedestal positions are determined every minute in presence of NSB to take into account the temperature dependence. This is done by checking the amplitude of neighbouring pixels, if their amplitudes are above a certain value, or if the pixels own amplitude is above a threshold. If the amplitude values are higher than the threshold, then the pixel is suspected to be contamined by Cherenkov light. So, the pixels for this event are not used in the pedestal histogram. The mean of the pedestal histogram gives the pedestal position. The pedestal position remains constant in the usual NSB range in Namibia, which is predicted to be about 100 MHz (per pixel). This induces a typical noise of 1.2 to 1.5 ph.e.s RMS in the pixels.

- **Conversion Factor:** The ADC to ph.e. *conversion coefficient or conversion factor* (γ_e^{ADC}) is calculated using the following relation:

$$\gamma_e^{ADC} \;=\; \int V_{ph.e.}(t) \; dt \; \frac{G}{N_d \; \tau \; V_{ADC}} \;\;, \tag{4.1}$$
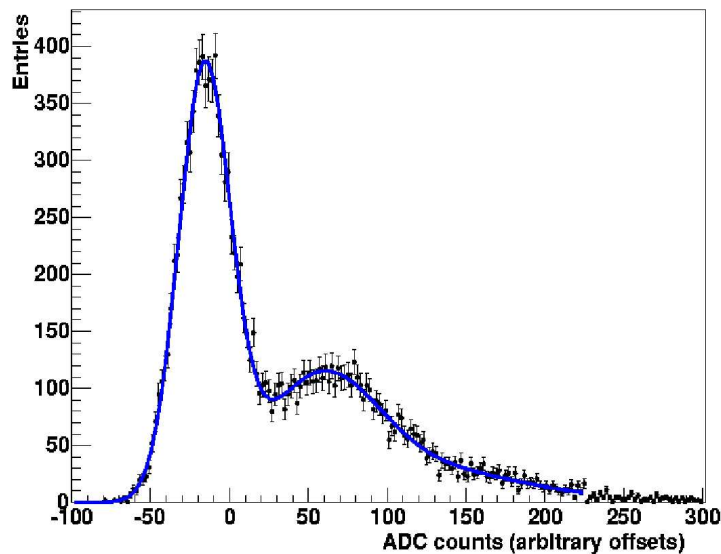
Abbildung 4.10: Typical example of a single photo-electron spectrum together with the fitted function. Figure taken from [114].

where $V_{ph.e.}$ is the single photo-electron pulse shape, V_{ADC} is the conversion factor of the ADC, which is 1.22 mV/count, N_d $\tau = 16 \times 10^{-9}$ is the read-out window in seconds. G is used for the pixel gain. The pixel gain G is determined by a fit to the ADC count distribution of a pixel which is obtained by illuminating the pixel by a LED-pulsar that provides a mean signal of $\sim$1 ph.e.. An example of a *ADC count distribution* is shown in Figure 4.10. To derive the ADC count distribution fit function, the following assumptions are made: The number of photons from the LED-pulser follow a Poisson distribution, the width of the electronic noise is much smaller than that of the single ph.e. distribution, and the single ph.e. distribution is described by a Gaussian distribution. The pedestal is also represented by a Gaussian function weighted by the probability of having zero ph.e.. The distribution of a single ph.e. is found to be approximately 75 - 85 ADC counts.

- **Amplification Ratio (HG/LG):** In the range from 30 to 150 ph.e., where HG- and LG-channels are linear (Figure 4.6), the mean ratio of the pedestal-subtracted ADC counts in both channels is used to estimate the amplification ratio for each pixel. The mean amplification ratios of all cameras are around 13.5, [88].

- **Flat-field Coefficients:** Although the electronics of PMTs is calibrated, pixels give slightly different responses to a uniform illumination.

This shows that there may still be inhomogeneities in the camera due to different quantum efficiencies of the pixels, and due to collection efficiencies of Winston cones. The *flat-field coefficients (FF)* are used to correct these differences and equalize the sensitivity of of the PMTs over the whole camera.

There are special *flat-field runs*, which are every every two nights. These runs are taken with the help of LED flashers. The camera is triggered in the same way as for Cherenkov emission of air-showers, but with an increased pixel multiplicity (> 9 pixels) to reduce the background of air-showers.

For each event the mean pixel amplitude, $\bar{A}_i$, over each camera is calculated (without the broken PMTs) as follows:

$$\bar{A}_i = \frac{\sum_{n=0}^{N} \sum_{p=0}^{956} P_{n,p}}{960 \ N}, \tag{4.2}$$

where $P_{n,p}$ is the amplitude of the pixel p for the event n and N is the total number of events. The ratio of each pixel amplitude over the mean pixel amplitude is accumulated over a run. The mean of this ratio gives the efficiency of each pixel relative to the camera mean, and the inverse of this value gives the flat-field coefficient (FF) of the pixel under consideration. The typical RMS of flat-field coefficients is $\sim 10\%$.

It should also be noted that the broken pixels are not used in the calibration process. The mean number of pixels excluded from the calibration and analysis is typically $\sim 4\%$.

In summary, following the calibration steps given above the calculation of the amplitudes (A^{HG} and A^{LG}) of every PMT for both channels (HG and LG) can be written as follows:

$$A^{HG} = \frac{ADC^{HG} - P^{HG}}{\gamma_e^{HG}} \ FF \ , \tag{4.3}$$

$$A^{LG} = \frac{ADC^{LG} - P^{LG}}{\gamma_e^{LG}} \ \frac{HG}{LG} \ FF \ , \tag{4.4}$$

where

- ADC^{HG}, ADC^{LG}: ADC counts in HG and LG channels respectively.

- P^{HG}, P^{LG}: Mean position of the pedestals.

- γ_e^{HG}, γ_e^{LG}: ADC counts equivalent to one ph.e. in HG- and LG-channel.

- $\frac{HG}{LG}$: Amplification ratio of the high gain to the low gain.

- FF: Flat-field coefficient.

Kapitel 5

The Stereoscopic Reconstruction

In this Chapter, it is explained how the stereoscopic shower reconstruction algorithms including the geometrical reconstruction and the energy estimation of the shower, are implemented in the H.E.S.S. software environment pursuing the ideas developed previously in the HEGRA experiment ([94], [111], [98]). The implementation demonstrated in this Chapter was one of the first trails to implement stereoscopic shower reconstruction algorithms in the H.E.S.S. environment.

Monte Carlo simulations are extensively used in the implementation and testing phases of the algorithms. The simulations are produced using the CORSIKA package for air-shower simulations and the *sim_ telarray* package ([23]) for detector simulations. Using the simulated Hillas parameters the shower parameters are reconstructed and compared to the simulated shower parameters to obtain the angular resolution, shower core resolution, and the energy resolution for various zenith angles. Look-up tables are filled to be used to calculate the MSW and MSL values and reconstruct the energy of the shower in event for each during the analysis of real data. Moreover, the rates, energy thresholds and collection areas are calculated using the simulations produced for various zenith angles. The collection areas are used in producing the energy spectrum of the Crab Nebula (Section 6).

5.1   Monte-Carlo Simulations

In order to understand the physical phenomena of the detected showers and the detector responses to different types of showers, simulations of cascades and the detector are very important in γ-ray astronomy. It is possible to study the differences between γ-ray and hadron induced showers so that a better discrimination between signal and background can be achieved. Moreover,

the energy estimation of the shower out of the measured data can not be achieved without the help of the simulations.

5.1.1   Shower Generator

Several sophisticated air-shower simulation packages are currently used by the cosmic-ray community. One of them is the *CORSIKA (COsmic Ray SImulations for KAscade)* package ([84], [83]) which was first developed for the *KASCADE* experiment, [60]. This package is used to simulate electromagnetic and hadronic cascades in a model atmosphere, using Monte Carlo techniques, and to track the trajectories of all secondary particles to relatively low energies like $\lesssim 1$ MeV. For the H.E.S.S. experiment CORSIKA is utilized together with other packages like KASCADE ([108]) package, which is used to simulate γ-ray air-showers at TeV energies, and IACT/ATMO ([26]) package, which allows an efficient recording of generated Cherenkov photons. For this thesis the latest version of CORSIKA package (version 6.0231) is used.

- **Air Shower Simulations:**

  Different particles can be chosen as the primary cosmic-ray. For the simulation of nuclear and electromagnetic interactions, values of cross sections from accelerator experiments are used.

- **Cherenkov Light:**

  When a charged secondary particle is produced with an energy higher than or equal to that for the production of Cherenkov light (Equation 2.14), the creation of Cherenkov photons along its flight-path is simulated. It is not possible to simulate flight-paths of the Cherenkov photons, because already for a γ-ray shower of 1 TeV the emitted number of photons is 6×10^7, [102], and simulating all flight-paths would require much longer simulation time, and larger disk space for storage. For this reason, the programme only calculates a *photon bunch*. The calculation of photon bunches are done by dividing the whole particle trajectory into segments, each of which has a length of ΔH (Figure 5.1). The mean number of Cherenkov photons, $\overline{N}$, are simulated for each piece of track segment, and it is assumed that all these photons are emitted from the middle of that track, which is shown as H in Figure 5.1. All the photons emitted from H form a Cherenkov cone with a Cherenkov angle θ. The detector plane cuts the Cherenkov cone at the height H_D forming a circle with a Cherenkov radius of R. The photons arriving the detector plane hit the mirrors of the telescope,

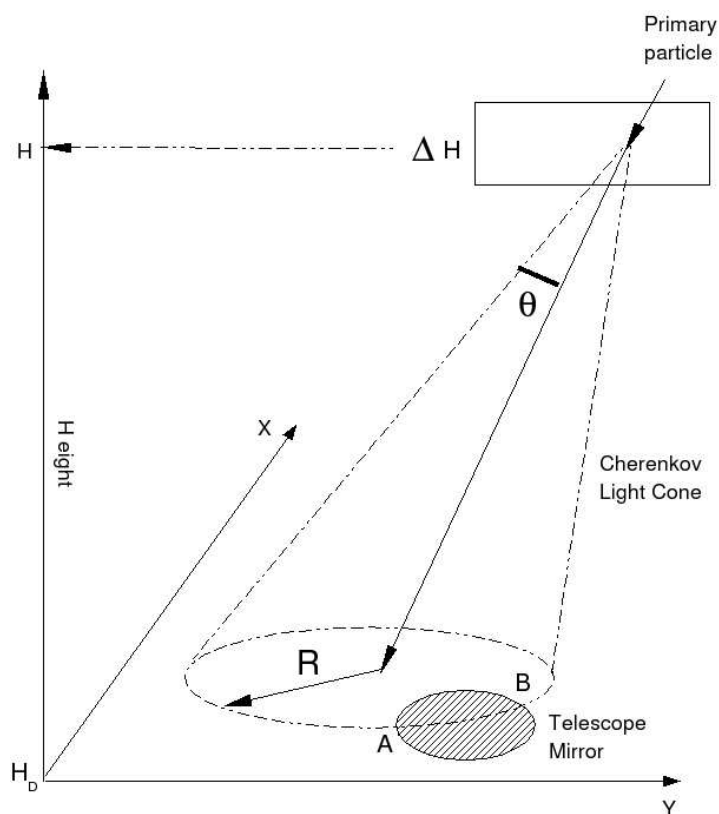Abbildung 5.1: Simulation of the Cherenkov light emission from a piece of simulated trajectory of the particle forms a Cherenkov cone. On the detector (XY-) plane, the Cherenkov cone has a radius of R. The representation of the mirror of a telescope is illustrated by the shaded region. The Cherenkov photons hitting the mirror surface bounded by the arc of $\overline{BC}$ come from the height H.

which is only a rough presentation at this stage. If Cherenkov photons hit a part of the mirror surface, which is bordered by the line segment $\overline{AB}$ shown in Figure 5.1, then the mean number of photons hitting this part of the mirror, $\overline{N}_D$, can be found from the following equation:

$$\overline{N}_D \;=\; \frac{\overline{AB}}{2\pi R}\,\overline{N} \quad .$$

Only the information of the photons hitting the telescope mirror are stored. For each photon hitting the telescope mirror the stored information comprises the direction of arrival, the arrival time of the photon on the telescope mirror, and the arrival position on the detector plane. These information is used by the atmosphere and detector simulations (Section 5.1.2).

- **Parameters:**

  For this thesis work the following parameters are set in CORSIKA to steer the simulations:

  - *The primary particle parameters:* For this thesis proton showers with energies in the range of 300 GeV - 60 TeV and γ-ray initiated showers with energies from 100 GeV to 20 TeV are simulated. The spectral index of the energy spectrum is selected to be -2.0 for γ-ray induced showers and -2.7 for background proton-showers.

    The direction (zenith angle, θ, and azimuth angle, ϕ) of the incoming primary particle is selected for simulation. A specific value of the *view cone* with a certain opening angle can be selected. If a *point source* is simulated, then the view cone is set to 0°. This feature can also be used in order to simulate background showers (e.g. protons), that are spread isotropically within the field of view of the detector. The simulated γ-ray showers in this thesis are all produced as a point-source and the background showers are produced with a view-cone value corresponding to the FoV of the H.E.S.S. camera ($\sim$5°).

    The impact positions of a simulated shower can be randomized over an area with a certain impact radius R_{max}. This procedure is usually done by shifting the telescope position randomly around the shower core position and it is called *oversampling*. The simulations produced are oversampled by a factor of 10 - 30 times. The selection of the R_{max} depends on the selection of the zenith angle and the energy of simulation. R_{max} is selected between 1 - 2 km in order to increase the gain for very high energy showers.

Oversampling helps to reduce the simulation time for larger R_{max} values, although it causes the detection efficiency for showers with lower energies to drop for larger R_{max} values. To overcome this problem, a method of *importance sampling* can be used ([153]).

– *Cherenkov light emission* is set in the wavelength range from 250 nm to 700 nm.

– The number of telescopes and their positions.

– *Environment parameters* are the atmospheric model, the geo-magnetic field strength, and its direction.

  The selected atmospheric model plays an important role in the development of air showers and propagation of Cherenkov light. The change of the refractive index of the air depends on the atmospheric depth as a function of height in the atmosphere (Figure 5.2). The number of generated Cherenkov photons change according to the atmospheric depth. The tabulated values of atmospheric depth and height are used by the simulation programme are the Windhoek, Namibia, all year average. The simulation also takes into account the atmospheric extinction, which includes absorption due to the aerosols and ozone, as well as Rayleigh- and Mie-scattering (Section 3.2.2).

5.1.2   Detector Simulation Procedure

For the H.E.S.S. experiment the response of the detector to the CORSIKA simulated air-showers is simulated by the *sim_telarray* package, [23]. By running this programme over a data set simulated by CORSIKA, the trigger decision, as well as information on the image parameters and the direction, impact position, and energy about a particular shower is obtained.

The signal created in the detector depends on the arrival time and number of the Cherenkov photons that pass the detector components like mirrors, funnels, and PMTs, as well as on the amplification and digitization of the electronic pulse. The simulation of the mirrors contain the reflectivity, which depends on the wavelength of the Cherenkov light (Figure 5.3 (top)). After a photon is reflected by the mirror, it arrives at the funnel, which guides the light to the PMTs. The transmission of the funnels is shown in Figure 5.3 (middle). The PMTs used in the experiment are sensitive in a wavelength range of 280 and 650 nm. The values of quantum efficiency are obtained from the manufacturer (Figure 5.3 (bottom)).
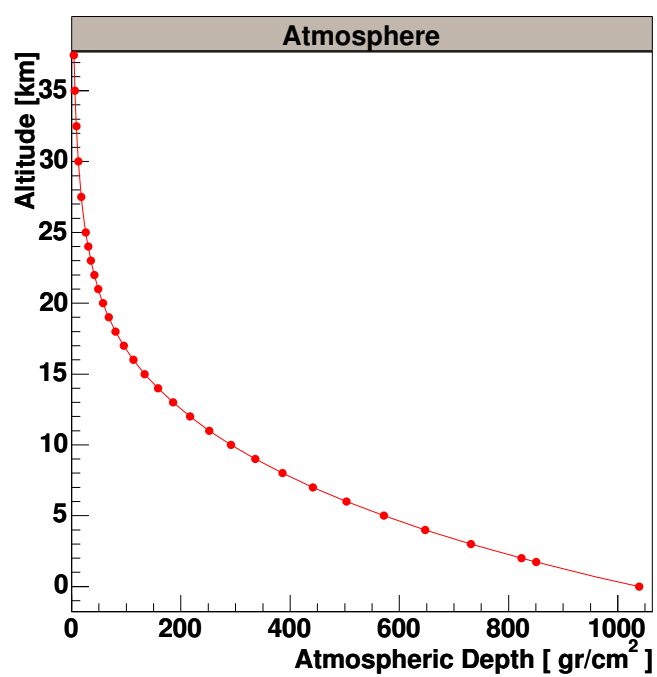
Abbildung 5.2: The relation between atmospheric depth and altitude in the atmosphere as used in the simulations. The values given here are for the atmospheric model-10 (Windhoek, Namibia, all year average)
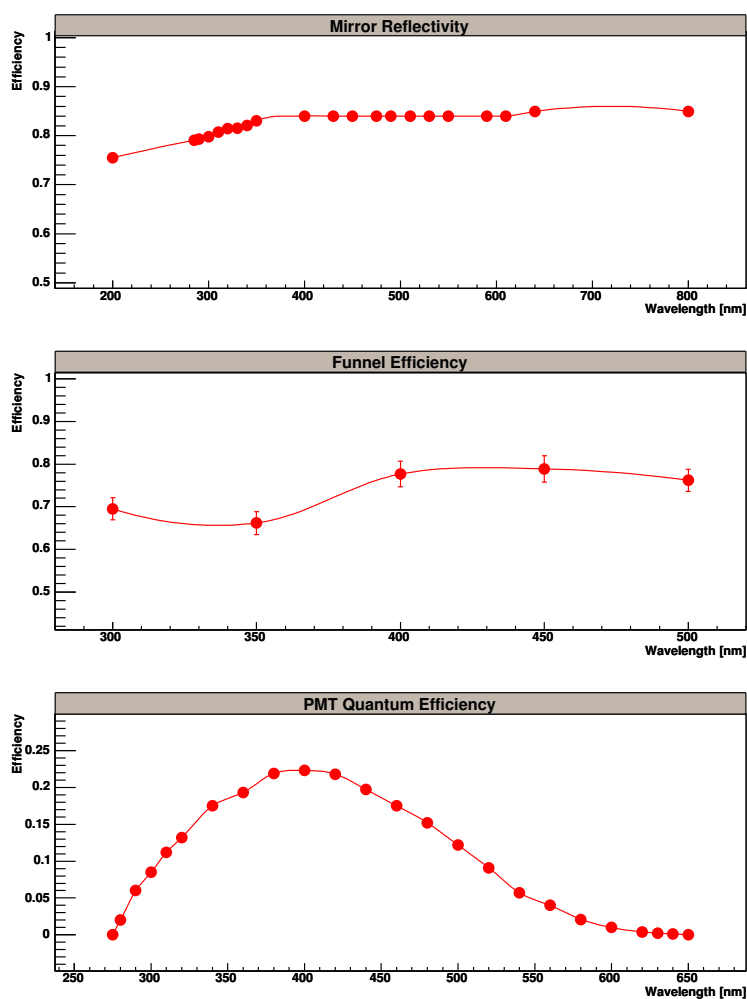
Abbildung 5.3: The light yield of different components of the telescope as a function of the wavelength of the Cherenkov light: The mirror reflectivity (top) and the quantum efficiency of the PMTs (bootom). In the middle plot the funnel efficiency is shown.

Tabelle 5.1: γ-ray showers for energies from 0.02 TeV to 20 TeV within the zenith angle range of 0° - 60° are simulated by the CORSIKA package ([84]) to be used in the analysis.

Zenith Angle [deg]	Radius of Cherenkov Cone [m]	Number of Simulated Showers Showers
0	1000	$1{\times}10^6$
20	1000	$1{\times}10^6$
30	1000	$1{\times}10^6$
40	1000	$1{\times}10^6$
45	1000	$1{\times}10^6$
50	1400	$12{\times}10^5$
55	1700	$6{\times}10^5$
60	2000	$4{\times}10^6$

The other parameters that play an important role are the NSB rate, trigger condition, electronic noise , and the pulse shape of the trigger signal.

Table 5.1 shows the set of simulated γ-ray data used for the analysis in this thesis work. This set is simulated for an offset of target position (i.e. wobble radius) of 0° and ±0.5°. Moreover, a set of background events are simulated for the same range of zenith angles.

5.2 Determination of Image Parameters

5.2.1 Hillas Parameters

An effective way to parameterize the image in the camera of an IACT was first developed by Hillas, [91], in the early 80s. These parameters of the image are called the *Hillas Parameters* (Figure 5.4).

The air-shower image on the two-dimensional camera focal plane can be regarded as a distribution of intensities characterized by the first, second, and third order moments of this distribution (Appendix A).

Assume that the ith pixel has coordinates $q_i = \{x_i, y_i\}$ (in radians), where the origin of the system is the center of the camera focal plane. If the distribution of intensities is a Gaussian distribution, then the matrix formed by second moments of the intensity distribution is an error matrix. The error
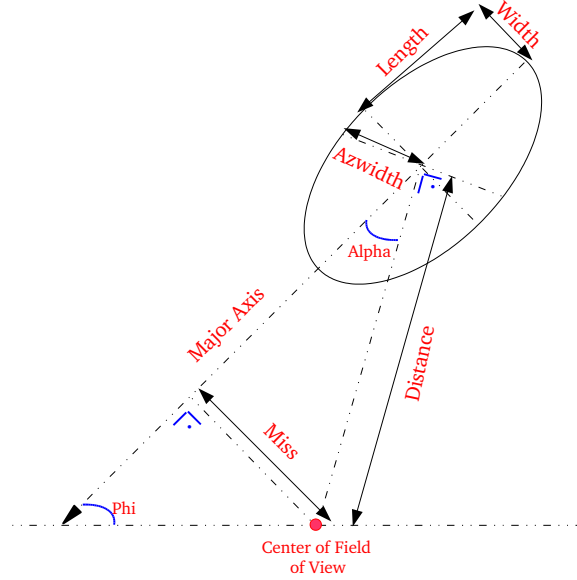
Abbildung 5.4: The Hillas parameters.

matrix can be defined as follows

$$M \; = \; \begin{pmatrix} \sigma_{x^2} & \sigma_{xy} \\ \sigma_{yx} & \sigma_{y^2} \end{pmatrix} \; . \tag{5.1}$$

The Length and Width can be directly derived using the second moments of the matrix elements, because they are the RMS spreads measured along the *major axis* and *minor axis* of the image, respectively. The squared values of Length and Width are given as

$$\langle \text{Length} \rangle^2 \; = \; \widehat{\sigma}_{x^2} \; = \; \frac{1}{2} \, \text{tr} M \; + \; \sqrt{\frac{1}{4} \, (\text{tr} M)^2 \; - \; \det M} \; , \tag{5.2}$$

$$\langle \text{Width} \rangle^2 \; = \; \widehat{\sigma}_{y^2} \; = \; \frac{1}{2} \, \text{tr} M \; - \; \sqrt{\frac{1}{4} \, (\text{tr} M)^2 \; - \; \det M} \; , \tag{5.3}$$

where $\text{tr} M \; = \; \sigma_{x^2} + \sigma_{y^2}$ is the trace of the matrix M and $\det M \; = \; \sigma_{x^2} \, \sigma_{y^2} - \sigma_{xy}^2$ is the determinant of the matrix.

The orientation angle of the image centroid, angle Phi (or ϕ) shown in Figure 5.4, is defined as the angle between the x-axis of the focal plane and

major axis of the ellipse. Assuming that the image is rotated by an angle ϕ, the rotation matrix can be written as

$$R = \begin{pmatrix} \cos\phi & \sin\phi \\ -\sin\phi & \cos\phi \end{pmatrix} \quad . \tag{5.4}$$

By rotating the matrix M using the rotational matrix R the angle ϕ can be obtained as follows

$$\phi = \arctan\left(\frac{\widehat{\sigma}_{x^2} - \sigma_{x^2}}{\sigma_{xy}}\right) \quad . \tag{5.5}$$

The intensity distribution in an elliptical image is not always symmetrically distributed along the minor and major axes. γ-ray image distributions are usually skewed towards the source position. The Asymmetry of the image in the camera, which is also known as the Skewness, can be computed using the second and the third moments of the intensity distribution:

$$\mu_x = \frac{1}{A}\sum_i s_i\,(x_i - \langle x\rangle)^3 = \langle x^3\rangle \ - \ 3\langle x^2\rangle\langle x\rangle \ + \ 2\langle x\rangle^3 \quad . \tag{5.6}$$

$$\mu_y = \frac{1}{A}\sum_i s_i\,(y_i - \langle y\rangle)^3 = \langle y^3\rangle \ - \ 3\langle y^2\rangle\langle y\rangle \ + \ 2\langle y\rangle^3 \quad .$$

The complete list of definitions of Hillas parameters are given in Appendix A.

5.2.2 Differences between Proton- and Gamma-shower Images

In order to detect γ-rays from the direction of observation, γ-ray showers have to be selected out of background (proton) showers. The shape and orientation of the two dimensional images in the camera can help to discriminate γ-ray induced air-showers from proton showers.

The angle α of an image gives information of the orientation of the air-shower image in the camera. If the telescope is directed towards the source position, the images of γ-ray showers have major image axes going through the center of the field of view. These images originating from the center of the camera have small values of α (Figure 5.5 (right)). On the other hand, proton images are randomly oriented over the field of view, due to the isotropic distribution of the arrival direction of the proton showers. So, the alpha distribution of proton showers is approximately flat all over the FoV (Figure 5.6 (bottom-right)).
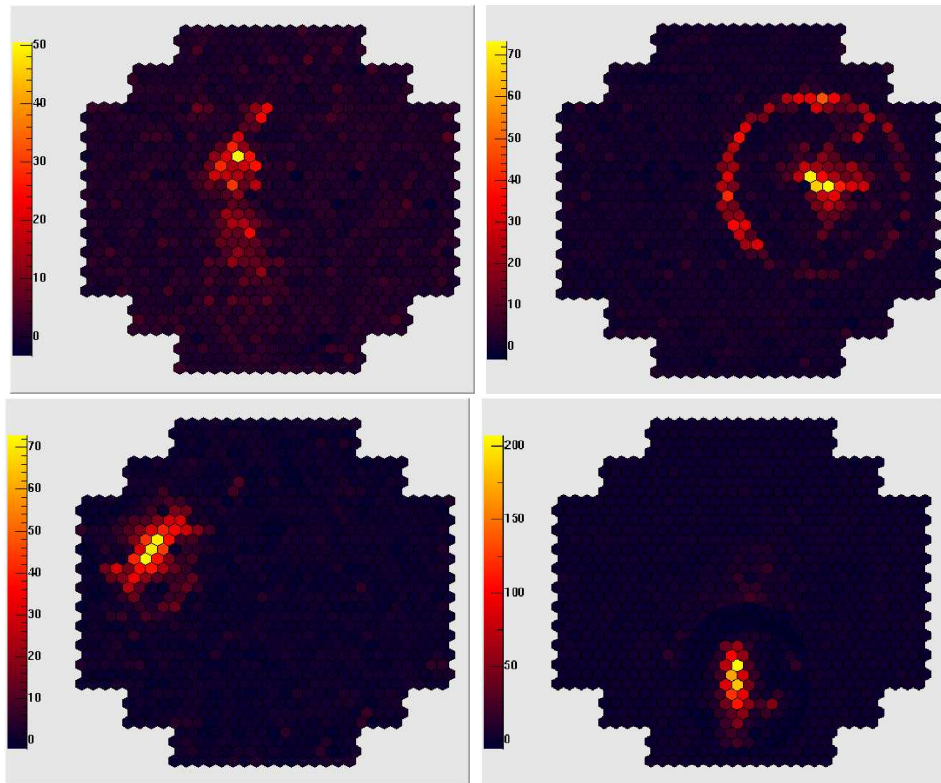
Abbildung 5.5: Hadron induced shower images (top-left) are usually sparsely distributed. Some of them (top-right) contain ring-like images caused by muons in the hadron induced showers. The γ-ray induced shower images as observed in the camera (bottom-right) are more compact relative to proton images (bottom-left). γ-ray showers have major image axes going through the center of the field of view, whereas proton images have larger values of parameter α. Color code gives the intensity in units of ph.e..

Figure 5.6 shows a typical distribution of the parameter α for simulated γ rays and background protons. The distribution of α depends on the angular spread of the γ-ray source. For a point-like source this distribution peaks at $0°$ and its RMS is given by the angular resolution of the telescope. For an *extended source* the peak around $0°$ becomes broader.

The *Width* of the image is an indicator of the lateral development of the air-shower and the *Length* gives information on the longitudinal development of the shower. For the fixed energy and impact distance of the shower to the telescope these two parameters for γ-ray showers are systematically smaller than for proton induced showers. Figure 5.6 (top-left and top-right) shows typical distributions of *Length* and *Width* parameters of γ- and proton induced
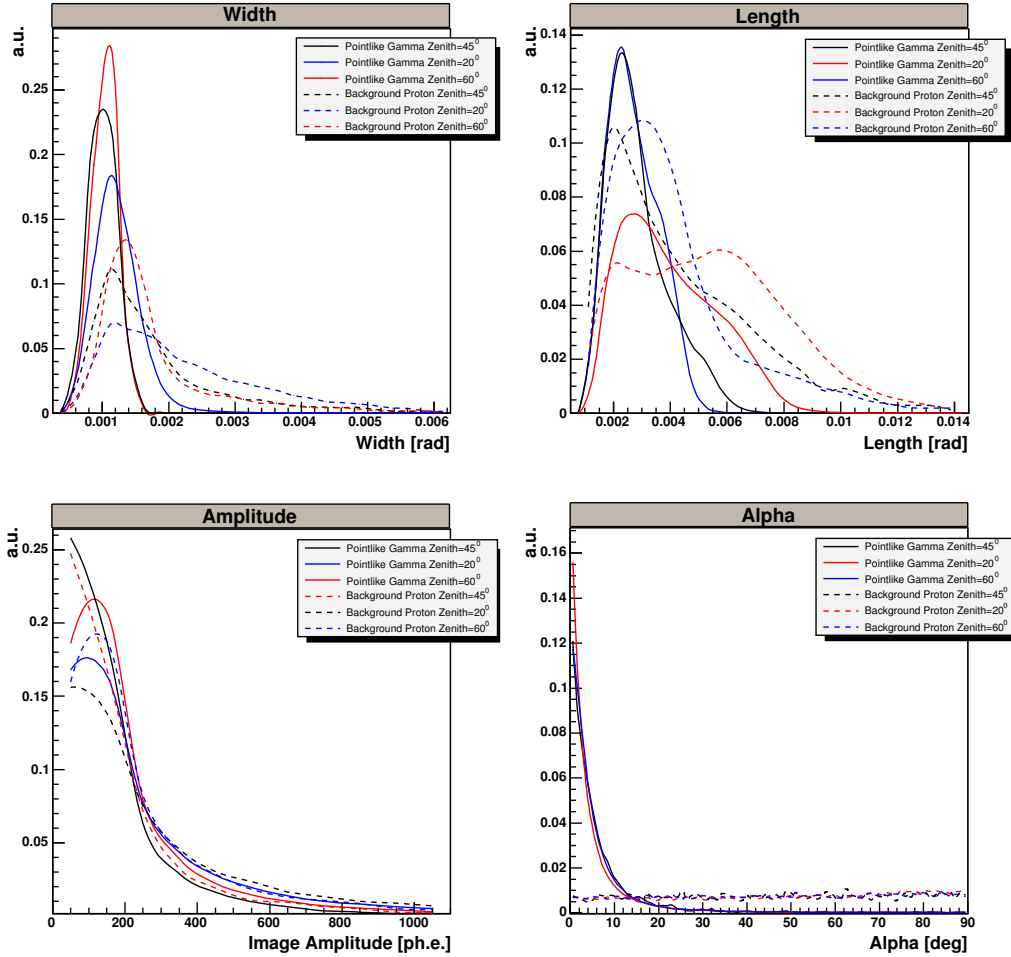
Abbildung 5.6: *Width, Length, Size* of an image and parameter α for simulated γ-ray showers for a point-like source produced with an energy spectral index of -2.0, as well as for proton showers simulated isotropically over the FoV of the camera with a typical cosmic-ray energy spectral index of -2.7. The solid lines are simulated γ-ray showers and the dashed line are for simulated proton background. Black, blue, and red lines are for showers simulated at 45, 20, and 60 degrees of zenith angle.

air-showers.

5.2.3   Mean Scaled Width and Length

The parameters Width and Length have been shown to be very effective for cosmic-ray background rejection. Although these two parameters perfectly describe the image shape and consequently the lateral and longitudinal shower extension of the shower, they depend strongly on the shower energy and the distance between the telescope and the shower core position, the *impact distance (ID)*. As a result, for a fixed cut on width and length the resulting discrimination efficiency for all simulated/recorded proton showers is not very high. In order to avoid the dependence of the standard image parameters width and length on image amplitude, which is proportional to the shower energy, and impact distance the *mean scaled width (MSW)* and the *mean scaled length (MSL)* can be derived for each shower event as follows

$$MSW \ = \ \frac{1}{N_{tel}} \sum_{k=1}^{N_{tel}} \frac{w_k}{\langle w \rangle_k^{ij}} \quad , \quad MSL \ = \ \frac{1}{N_{tel}} \sum_{k=1}^{N_{tel}} \frac{l_k}{\langle l \rangle_k^{ij}} \ , \qquad (5.7)$$

where N_{tel} is the total number of triggered telescopes in the event, w_k is the width of the kth image, and $\langle w \rangle_k^{ij}$ is the expected mean image width calculated beforehand from the Monte Carlo simulations over a number of bins on the impact distance (ΔID_i ; i=1,...,50) and image amplitude ($\Delta \log(A_j)$; j=1,...,50), where the width of ith impact distance bin is ΔID_i and the width of the jth logarithmic image amplitude bin is $\Delta \log(A_j)$, [111].

5.3   Geometrical Reconstruction of Showers

The concept of stereo imaging is based on the simultaneous detection of air showers in different projections by at least two telescopes separated by a distance, which is comparable with the radius of the Cherenkov light pool. In the H.E.S.S. experiment the telescopes are built at the corners of a square with side length of 120 m. The advantages of stereoscopic observations are: (i) better quality of reconstruction of shower parameters, as compared to a single telescope; (ii) very powerful rejection of background showers, (iii) effective suppression of night-sky as well as muon background [10]. Depending on the size of the array, the dynamic energy range in registration of γ rays may be extended towards multi-TeV showers.

Using the coordinate transformations given in Appendix B, the shower direction, the shower core position, the height of the shower maximum, and

the energy of the shower is determined. Below the methods of determination of the complete shower geometry are given:

- **Determination of Shower Arrival Direction:** The information of the pixel coordinates are transformed from the camera system into the nominal system. Using this information the major axis of images are determined for each telescope. Then the so-called Algorithm 1, which is one of the reconstruction algorithms explained in [94], for the directional reconstruction is applied. The orientations of the major axes of any triggered telescope pair are used to find their intersection in the camera focal plane in the nominal system (Figure 5.7). Afterwards, a weighted mean of these intersection points is taken as the shower direction. Various alternative weights can be used in this procedure. In this work, the weighting factor for the intersecting ith and jth telescopes ($i, j = 1, 2, 3, 4$) is defined as follows
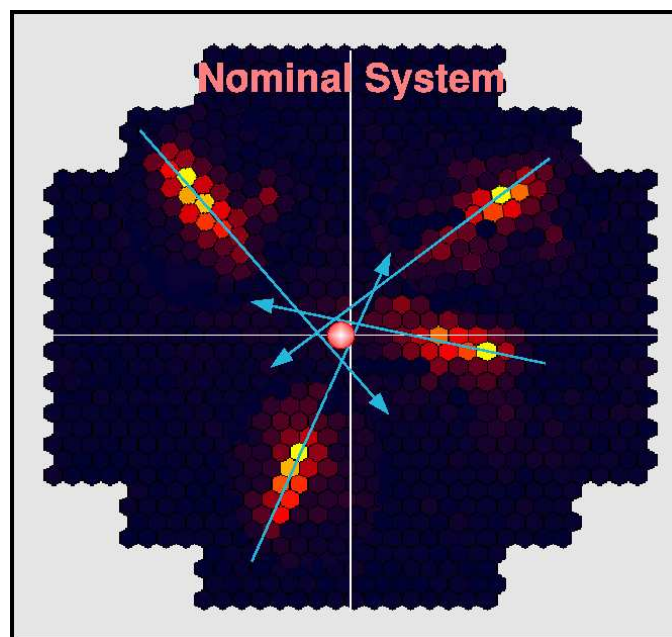
Abbildung 5.7: The shower direction is calculated as the weighted mean of the intersection points of the image major axes of triggered telescope pairs in the nominal system.

$$w_{ij} = \frac{|\sin(\phi_i - \phi_j)|}{1/\text{size}_i + 1/\text{size}_j} \quad , \tag{5.8}$$

where $\phi_{i(j)}$ is the angle between the image major axis and the x-axis in the nominal system for the $i(j)$th telescope. The weight w_{ij} is derived

empirically from the fact that the telescope pairs with larger angles between their intersecting image major axes and telescopes having brighter images provide a more precise determination of the shower axis. Therefore, with the help of this weight, telescope pairs with their major axes being approximately parallel to each other and telescopes with very faint images are suppressed to improve the reconstruction quality.

More information on different methods of the reconstruction of the shower direction can be found in [94].
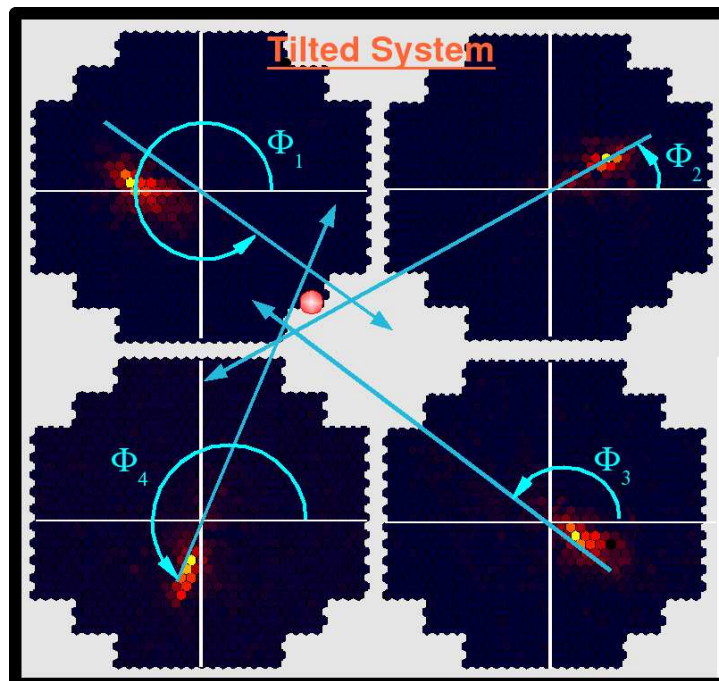
Abbildung 5.8: The shower core position is calculated by intersecting the directional lines formed by the telescope coordinates and image orientation angle (Φ) in the z-projected plane of the tilted system. The intersection points are weighted with the angle of intersection, and the mean of these intersection points gives the shower core position.

- **Determination of Shower Core Position:** The core position is calculated in the tilted system. First the x,y coordinates of the telescopes are transformed from the ground system into the tilted system (Appendix B). Using the telescope coordinates and the orientation angle ϕ, a directional line is calculated for each triggered telescope. For each pair of triggered telescopes an intersection between the directional lines (Figure 5.8) attached to the actual telescopes positions in the z-projected

plane of the tilted system is determined using the following weight

$$w_{ij} = |\sin(\phi_i - \phi_j)| \ . \tag{5.9}$$

The weight w_{ij} is empirically derived like Equation 5.8, from the fact that the telescope pairs with larger angles between their intersecting image major axes results in a more accurate determination of the shower axis. The contribution of the image amplitudes to the weight are not used in Equation 5.9.

The weighted mean of all intersection points gives the core position of that shower in the tilted system. This reconstructed shower core position is denoted as $\vec{p}$ (in the ground system). In the H.E.S.S. analysis the convention is used to express the final core position in the x-y plane corresponding to z = 0. So, the shower axis, which is defined by $\vec{p}$ and the shower directional vector $\vec{r}$ are located in the plane of z = 0. The position of the shower core in the x-y plane is given by $\vec{C}$, and it is found as follows

$$\vec{C} = \vec{p} - \frac{p_z}{r_z} \vec{r} \ , \tag{5.10}$$

where p_z and r_z are the components of $\vec{p}$ and $\vec{r}$ in z-direction, respectively.

5.3.1 Angular Resolution and Accuracy of Shower Core Localization

In Figure 5.9 (top-left) (or (top-right)), the difference $\Delta\theta_x$ (or $\Delta\theta_y$), between the x-(or y-)components of the reconstructed shower direction and the actual simulated shower direction is shown. The radial angular residual, $\Delta\theta$, is found by

$$\Delta\theta = \sqrt{\Delta\theta_x^2 + \Delta\theta_y^2} \ . \tag{5.11}$$

Higher values of $\Delta\theta$ would imply a bad reconstruction of the shower direction basically due to the erroneous reconstruction of the major axis of the simulated/recorded images. This problem arises mainly for very faint images, which are produced by showers at rather large impact distances from the telescope, as well as by showers of very low energies.

The images detected at relatively large impact distances have an elongated angular shape and enable an accurate determination of the image orientation ([112]), as long as the images are not truncated by the camera edges.
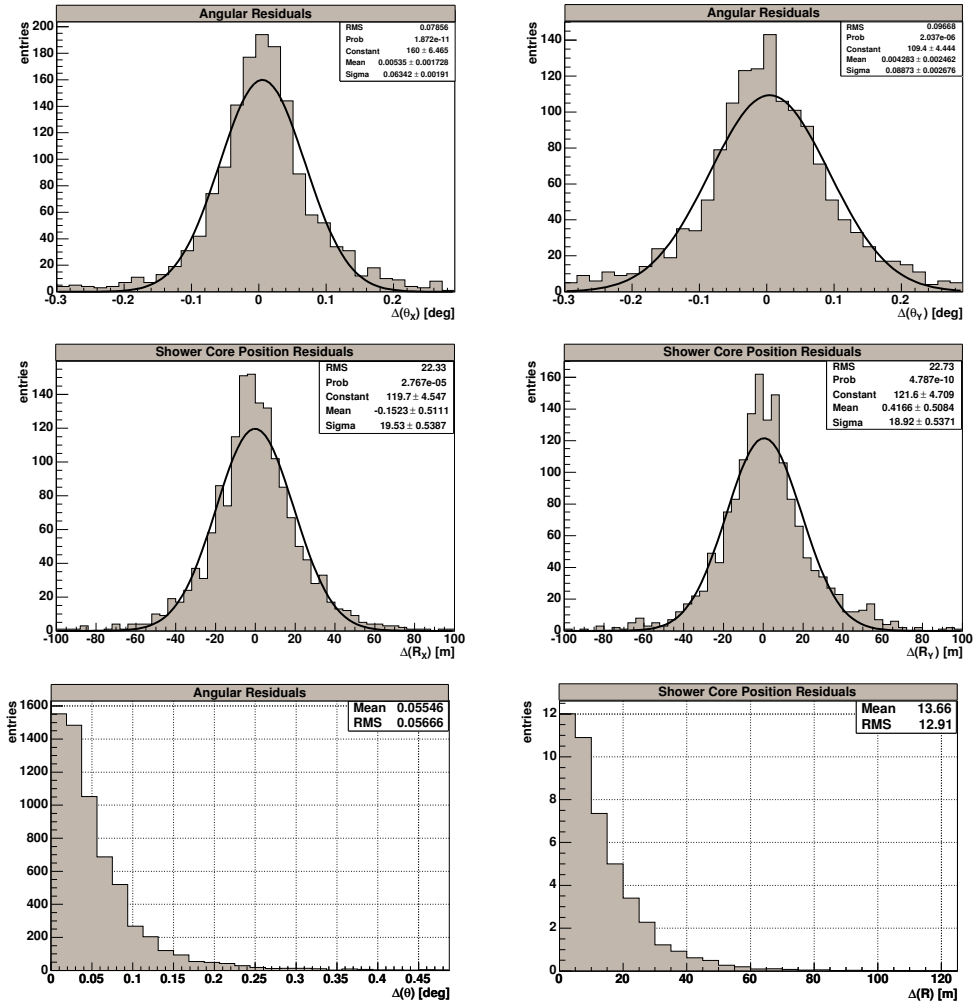
Abbildung 5.9: Distributions of angular residuals ($\Delta\theta_x$ (top-left), $\Delta\theta_y$ (top-right)) and residuals of shower-core position (ΔR_x (middle-left), ΔR_y (middle-right)) of the reconstructed γ-ray candidates are shown. The showers are simulated for zenith angles of 45° and quality cuts are applied (see text). Radial angular resolution, $\sigma_{\Delta\theta}$, is the value of $\Delta\theta$ (on the x-axis), left of which the number of entries is 68% of the total number of entries in the $\Delta\theta$ distribution (bottom-left). Similarly, the shower-core position resolution, $\sigma_{\Delta R}$, can be found from the ΔR distribution (bottom-right).

This effect needs to be eliminated in the analysis, because it may result in distorted image shapes and consequently wrong reconstruction of the image orientations. To remove distorted images from the analysis some specific cuts are applied. These cuts are called the *quality cuts*, which are applied after the image cleaning procedure (Section 6.2). They are listed below

- Image Amplitude $\geq$ 45 ph.e.,

- Distance $\leq$ 2 degrees,

- minimal number of pixels in an image $\geq$ 4,

- minimal number of images in the event $\geq$ 2.

The distribution of $\Delta\theta$ after the quality cuts is shown in Figure 5.9 (bottom-left), which still has a long tail towards higher values of $\Delta\theta$. In the distribution of angular residuals, the value, for which 68% of the whole entries of the $\Delta\theta$ distribution are within the error circle around the source position, is taken as the *angular resolution, $\sigma_{\Delta\theta}$,* of the reconstruction. Similarly, the accuracy of localizing the shower core position (*shower-core resolution*), $\sigma_{\Delta R}$, is found from the distribution of shower-core residuals given in Figure 5.9 (bottom-right).

It was found that the angular resolution of the IACT strongly depends on the telescope multiplicity ([112]), where the higher multiplicity of triggered telescopes results in a better angular resolution. To observe telescope multiplicity dependence of angular and shower-core resolutions at various energies, the values of $\sigma_{\Delta\theta}$ and $\sigma_{\Delta R}$ are calculated for each energy bin between 0.1 TeV and 20 TeV and for telescope multiplicities of 2, 3, 4, and $\geq$2 (Figure 5.10).

From Figure 5.11, it is apparent that the showers with higher energies located close to the center of the telescope array yield the best angular and shower-core resolutions. For example, the average angular resolution is found to be of $\sim$0.16° and the average shower core resolution is found to be of $\sim$33 m at zenith angle of 45°. The accuracy of localization of the shower core position correlates with the accuracy in the angular resolution.

It is found that the dependence of angular resolution on the source position in the FoV (or the pointing modus of the telescopes) can be ignored within a reasonable angular distance from the center of the camera. Therefore, so-called wobble-mode observations up to 1.5° do not significantly affect the angular resolution [112].
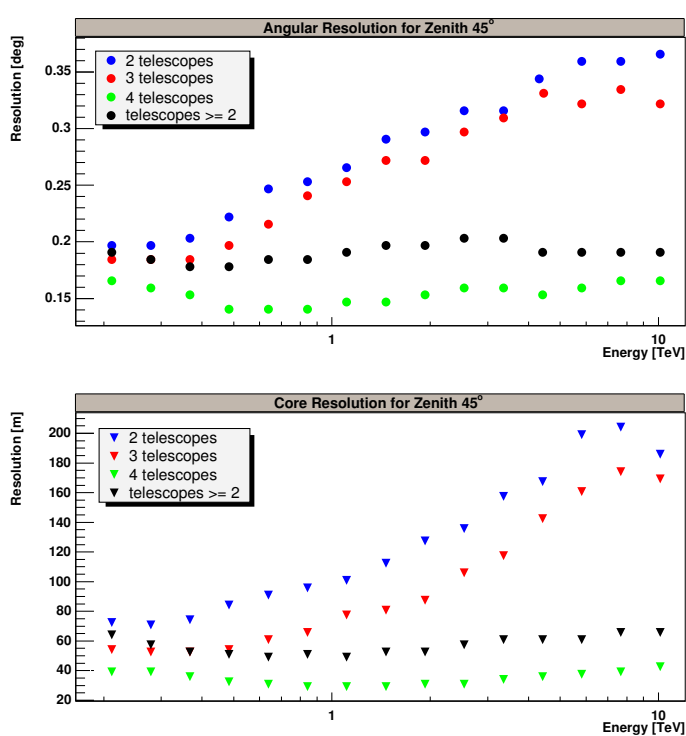
Abbildung 5.10: The angular- (top) and shower core (bottom) resolutions at a zenith angle of 45° are calculated per energy bin for telescope multiplicities of 2, 3, 4, and ≥ 2 (blue, red, green, and black markers, respectively).
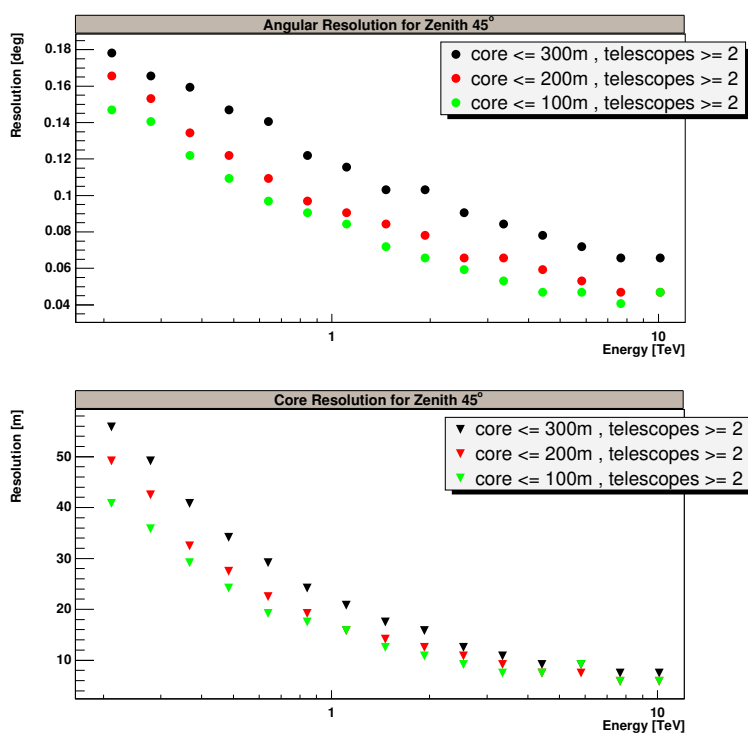
Abbildung 5.11: The angular- and shower core resolutions at a zenith angle of 45° are calculated per energy bin for telescope multiplicities ≥ 2. and after various cut values applied on the shower core: 100, 200, and 300 (shown by green, red, and black markers, respectively).
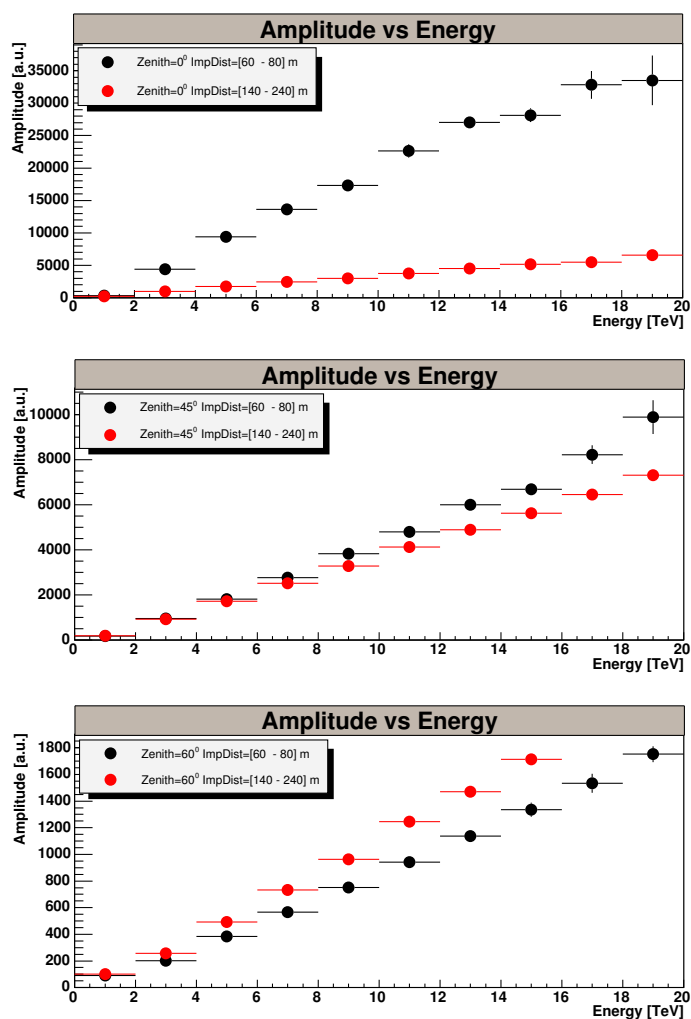
Abbildung 5.12: The relation between the energy of the shower and the measured image amplitude is shown for different zenith angles (0° (top), 45° (middle), 60° (bottom)) and for two different true impact distance ranges: the range of 60 - 80 m shown with black markers and the range of 140 - 240 m shown with red markers.

5.4 Method of Determination of Shower Energy

The amplitude of the shower image in the camera is proportional to the amount of emitted Cherenkov light from the region around the shower maximum. The amount of Cherenkov light is proportional to the energy of the air-shower. The strong correlation between image amplitude and shower energy is shown in Figure 5.12. For a fixed energy E_0, the amplitude of the image depends on the zenith angle of observations and the impact distance. This is demonstrated in Figure 5.12 for zenith angles 0°, 45°, and 60° at two impact distance intervals, 60 - 80 meters and 140 - 240 meters.
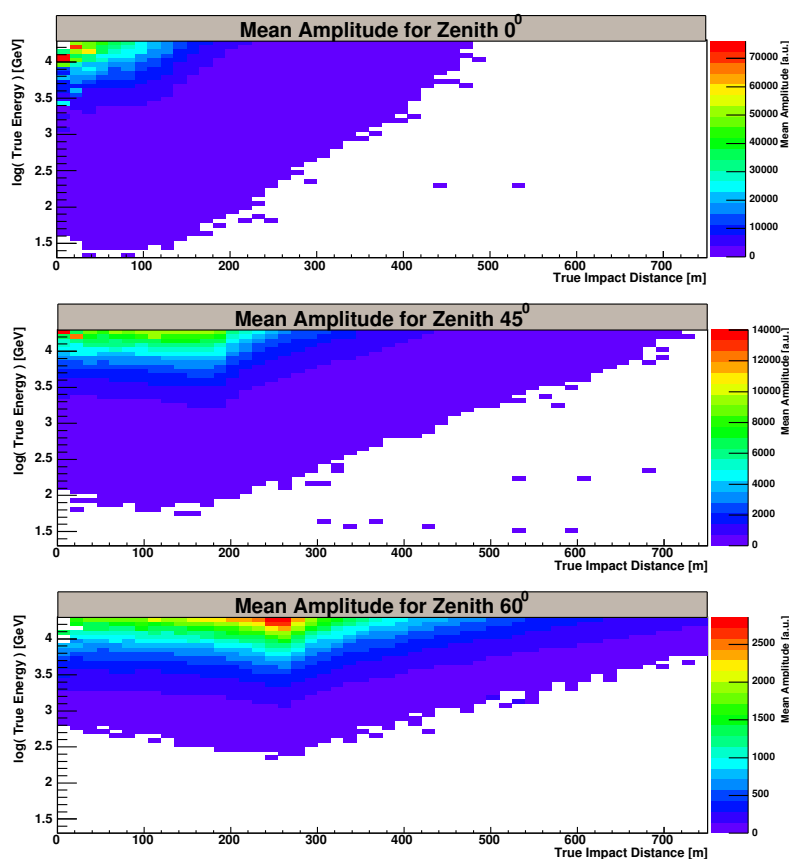
Abbildung 5.13: The look-up tables containing mean amplitude values for 50 true energy bins and 50 true impact distance bins shown for zenith angles of 0° (top), 45° (middle), and 60° (bottom), where the color code indicates the mean amplitude value in each true energy and impact distance bin.

The relationship between the amplitude of the image at a specific true impact distance and energy of the shower can be tabulated using Monte Carlo

simulations. The tables are produced for zenith angles of 0°, 20°, 30°, 40°, 45°, 50°, 55°, 60°. Each of these tables is subdivided into 50 logarithmic bins of true energy in the range of 0.02 - 20 TeV and 50 bins of true impact distance within a range of 0 - 750 meters. The range of impact distance is taken large enough to include the higher energy events at larger zenith angles 55° - 60°. In Figure 5.13 the tables for zenith angles 0°, 45°, and 60° are shown. The x-axis and y-axis represent the true impact distance and the true energy, respectively. The color code indicates the value of the mean amplitude for each bin. In observations the basic information that can be obtained for each recorded event consists of the image amplitude for each of triggered telescope, the reconstructed impact distance, and the zenith angle. The table corresponding to the zenith angle of observation (z_0) is selected. For the true impact distance bin including the measured impact distance value (ID_0) the tabulated true energy and mean amplitude values are plotted and a straight line is fitted to the data. The resulting fit parameters and the measured image amplitude (A_0) are used to reconstruct the energy ($E^{Reco}(z_0)$) for this specific impact distance bin. In case, there is no table found corresponding to the measured zenith angle, the closest two tables produced for zenith angles z_{low} and z_{high} are read. For ID_0, energies $E^{Reco}(z_{low})$ and $E^{Reco}(z_{high})$ are calculated from these tables. $E^{Reco}(z_0)$ is obtained from the linear interpolation in $\cos(z)$ between $E^{Reco}(z_{low})$ and $E^{Reco}(z_{high})$ as follows:

$$
\begin{aligned}
E^{Reco}(z_0) \;=\; & E^{Reco}(z_{low}) \;+ \\
& \left(E^{Reco}(z_{high}) - E^{Reco}(z_{low}) \right) \left(\frac{\cos(z_{low}) \;-\; \cos(z_0)}{\cos(z_{low}) \;-\; \cos(z_{high})} \right) \;,
\end{aligned} \quad (5.12)
$$

where $E^{Reco}(z_0)$ is the reconstructed energy for the ith triggered telescope ($i = 1 , ... , N_{tel}$) and N_{tel} is the total number of triggered telescopes). The reconstructed energy for the system (E^{Reco}_{sys}) is then the mean of reconstructed energies for all triggered telescopes. E^{sys}_{Reco} is the final measure of the shower energy used for the spectrum evaluation.

5.5 Energy Resolution

If the energy of a simulated shower of energy E^{True} is reconstructed as E^{Reco}, the fractional residual of the energy is calculated as follows:

$$
\Delta E \;=\; \frac{(E^{Reco} \;-\; E^{True})}{E^{True}} \;, \quad (5.13)
$$

where the RMS of the distribution of residuals is given as the energy resolution $\sigma_{\Delta E}$, and the mean of this distribution gives the bias. The residual

distributions for energy bins of 400 GeV and 7 TeV are shown in Figure 5.14. Each distribution is fitted using the Gauss function, which roughly describes the ΔE distribution. Starting from the energy bin, which is around 400 GeV (In Figure 5.14 (top)), up to higher energies (≥ 5 TeV), the ΔE distribution has a tail, the reasons of which are not further studied in this work.
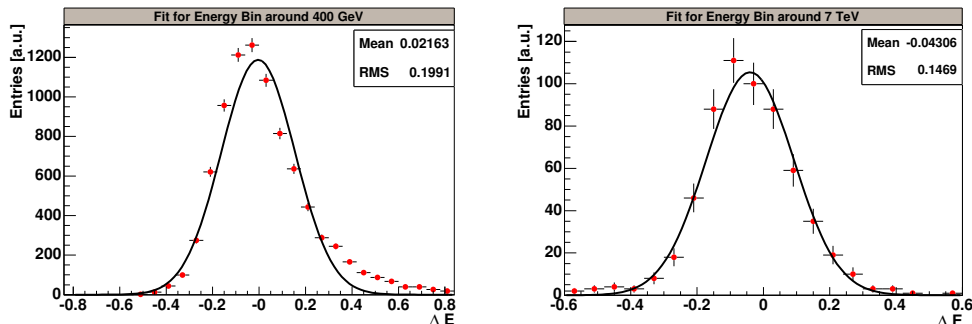
Abbildung 5.14: Distributions of fractional residuals for zenith angle of 45° and energy bins around 400 GeV (top) and 7 TeV (bottom) together with a gaussian fit.

The quality of reconstruction of the shower direction, shower core position, and shower energy depends on the analysis cuts. In addition to the quality cuts (Section 5.3.1), shower (parameter) cuts are applied to improve the overall energy resolution in the range of 300 GeV to 20 TeV.

In the selection of the shower parameter cuts the following rough estimate is used: A typical height of the shower maximum is around 6000 meters above the telescopes. Cherenkov light emitted from this height would have a typical Cherenkov angle of $\sim 2°$, which corresponds to a Cherenkov pool with a radius of ~ 200 meters on the ground. Assuming that the edge of the Cherenkov pool touches on the ground the edge of the collection area (with radius ~ 100 meters) of an individual telescope, it causes the telescope to trigger. If the whole array also triggers for the same shower, the shower has to be (according to the geometry of the H.E.S.S. array) at least ~ 300 meters away from the array center. For larger zenith angles of observation the value of the shower core and impact distance cuts can be increased, i.e. impact distance cut is increased to 400 meters for zenith angles higher than 50°. Optimization of the shower parameter cuts is not done. The selected *shower parameter cuts* are the following:

- Shower core distance ≤ 300 m,

- shower impact distance ≥ 50 m and ≤ 200 m.

The fractional bias and energy resolutions are calculated after the analysis cuts for the showers simulated for a zenith angle of 45° and for an energy range of 0.1 TeV and 20 TeV. The results are shown in Figure 5.15. Over 300 GeV a negative bias in ΔE distributions is observed in all energy bins, whereas biases are smaller than 10% between 300 GeV and 20 TeV.
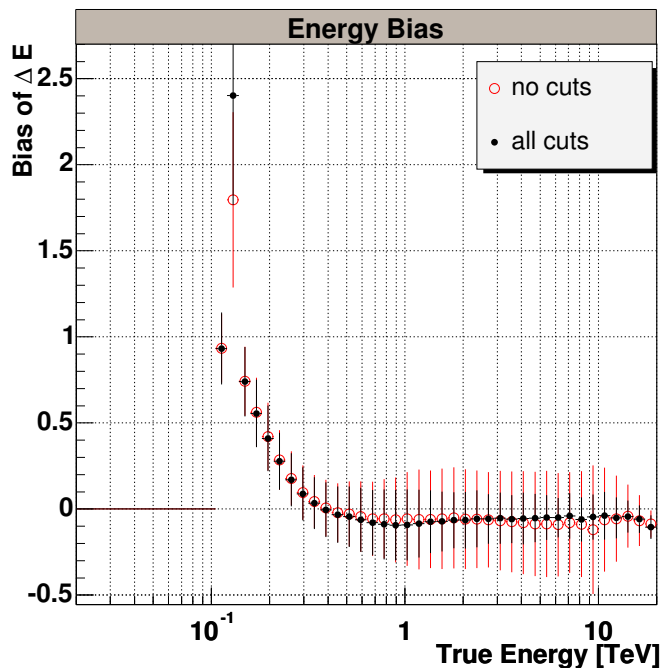
Abbildung 5.15: Energy bias of distributions of fractional residuals (ΔE) for each energy bin between 100 GeV and 20 TeV for a zenith angle of 45° are shown with black or red markers. The red markers show the bias without any cuts. The black markers show the bias after the quality cuts and the shower-parameter cuts, which are explained in the text. Error bars are the RMS values ($\sigma_{\Delta E}$) of the fractional residual distributions for each energy bin. The bias in the reconstruction is smaller than 10% in all energy bins above 300 GeV.

The bias in the energy is calculated each time, when the energy is reconstructed. This means, each time when the shower direction and core position are reconstructed and after the shower passes all the cuts, the reconstructed energy is compared to the true energy. The bias is positive for energies lower than ∼300 GeV and it increases while energy decreases. The bias calculated for energy bins higher than ∼300 GeV is negative and it stays constant for all higher energy bins. Both the positive bias for energy bins lower than ∼300 GeV and negative bias for energy bins higher than ∼300 GeV can be

explained as follows:

While filling the lookup tables, the mean amplitude calculated for any impact distance bin is an average of amplitudes of high-energy and low-energy showers. To find the reconstructed energy, the image amplitudes of showers having impact distances corresponding to a certain impact distance bin are compared to the averaged image amplitude for that impact distance bin. Then the energy is read out for the corresponding impact distance and mean amplitude bins.

The detection probability of low-energy showers (< 1 TeV) is smaller compared to the detection probability of high-energy showers. However, more low-energy showers are detected within smaller impact distances than high-energy showers, because the energies of the showers are weighted with a spectral index of -2.0 during the simulations. Nevertheless, some of these high-energy shower images are registered and they contribute to the mean amplitude calculated for smaller impact distance bins in the lookup tables. Therefore, when image amplitudes from low-energy showers are compared to the mean amplitude from the tables, the mean image amplitude is higher compared to most of the low-energy shower image amplitudes. Additionally, the positive bias gradually increases for the energy bins lower than ~ 300 GeV, because the number of simulated low-energy showers that contribute to the the mean amplitude decreases rapidly for impact distances smaller than ~ 100 meters and also for impact distances greater than ~ 250 meters for 45°.

The high-energy shower images dominate the large impact distance bins, because the shower-maxima of low-energy showers occur higher in the atmosphere due to atmospheric extiction these showers can not be detected by the telescopes. Only the showers having energies higher than 1 TeV contribute to the mean amplitude for larger impact distances, although, for example, the detection porbability of 1 - 5 TeV showers drop gradually after ~ 400 meters, when compared with 5 - 10 TeV showers. However, the shower energies are simulated with a spectral index of -2.0. Therefore, there are less high energy showers compared to lower energy showers in each energy bin. Therefore, the mean amplitude at large impact distance bins has the contribution from the detected lower energy showers, and if the mean amplite value from the lookup tables is compared to any individual high-energy shower image amplitude, it causes the shower energy to be underestimated. The negative energy bias stays constant over higher energy bins, because the number of higher energy showers decrease at higher energy bins due to weighting the energies with the spectral index, whereas the detection probability of lower energy showers decrease at larger impact distances, balancing the loss of higher energy events in these impact distances.

The shower parameter cuts, especially the shower core cut, improve $\sigma_{\Delta E}$ from 0.23 to 0.14 for data at zenith angles 45°. Both the shower cuts and the quality cuts decrease the number of events. Shower cuts decrease the number of events in the higher energy bins.

The possible factors that influence the energy resolution are the following:

- *Statistical fluctuations in the image:* The number of photoelectrons in a typical image is $\mathcal{O}(100)$ (Figure 5.5). The statistical fluctuations in the number of photoelectrons limit the resolution to $\mathcal{O}(10\%)$. Amplification of PMTs or variations in the NSB produce more fluctuations in the number of photoelectrons [98].

- *Image truncation:* Two effects give rise to mis-reconstruction of the image parameters and consequently the shower parameters.

  First, faint images produced by showers of very low energies, or by showers, which have the shower maximum too high in the atmosphere (i.e. at large zenith angles) usually generate images, which are circular rather than elliptical in shape. Therefore, the image parameters can not be calculated very accurately. In fact, a large fraction of these images is truncated by the tail cuts (see Section 6.2), and these images have corrupted shapes leading to erroneously reconstructed shower parameters.

  Second, the images can be truncated at the edges of the camera. This effect is important for showers with large impact distances, because the image of these showers are stretched out and they sometimes continue beyond the camera. In such a case the orientation of the images (the image's major axis) can be reconstructed incorrectly. For this reason, a distance cut is applied in the analysis (Section 5.3.1). This cut accepts only images with the center of gravity within a given radius.

- *Threshold effect:* In the region near the trigger threshold, the detected image intensity is biased. To improve the shower reconstruction quality an amplitude cut is introduced in the analysis, which accepts only images with a number of photoelectrons above a certain value (Section 5.3.1).

- *Shower-core localization efficiency:* The quality of the shower energy reconstruction depends in addition on the reconstruction efficiency of other shower parameters like the shower direction and core position. Especially for telescopes outside the characteristic Cherenkov radius, where the light intensity decreases quickly with the shower core distance, the uncertainty in the energy estimate may exceed 30% [98].

- *Systematic errors:* These may be related to the imperfections in Monte Carlo simulations of air-showers or telescope response. Also imperfect alignment and calibration errors, which are not simulated, may cause systematic effects. More details are given in Section 6.10.

- *Monte Carlo statistics:* Statistical errors in the look-up tables, especially at higher energies, may affect the quality of reconstruction of the shower energy.

5.6 Evaluation of Collection Areas

The physics of astrophysical objects is strongly linked to their energy spectrum. The detection rate of γ rays for a particular γ-ray source can be used to evaluate the flux of that source, $\Phi(E)$, which can often be parametrized by a power law with a spectral index of α,

$$\Phi(E) \;=\; \Phi_0 \; \left(\frac{E}{E_0}\right)^\alpha \quad . \tag{5.14}$$

A telescope detects for a certain zenith angle of Z a shower with an energy reconstructed within an energy interval of E_i^{Reco}, with a detection rate of $\Gamma(E_i^{Reco}, Z)$ that can be expressed as

$$\Gamma(E_i^{Reco}, Z) \;=\; \frac{N^{Ex}}{T} \quad , \tag{5.15}$$

where N^{Ex} is the number of excess events compatible with the source direction for an observation time of T, which is corrected for the dead-time of the telescopes. In order to calculate the flux value of a source for an energy interval E_i^{Reco} observed under a zenith angle of Z, apart from $\Gamma(E_i^{Reco}, Z)$ also the so-called *(effective) collection area* $A_{coll}(E_i^{Reco}, Z)$ of the telescope system has to be known.

$A_{coll}(E, Z)$ is computed from the Monte Carlo simulations. γ-ray showers are simulated with a spectral index of -2.0 under a zenith angle Z, which fall randomly onto an area A_0 limited by a radius R_{max} and trigger the telescope system. The telescopes' trigger condition is set to 3 neighboring pixels with a pixel signal above 4 ph.e.. From those events that cause a trigger for a minimum telescope multiplicity of 2, only the events for which the energy can be reconstructed and those passing the analysis cuts, are recorded and used in the collection area calculations. The collection area is given as

$$A_{coll}(E^{Reco}, Z) \;=\; A_0 \left(\frac{n}{N} \right) \quad , \tag{5.16}$$

where n is the number of showers that trigger the telescope array and which have a reconstructed energy E^{Reco} and pass the γ-ray selection criteria (Section 5.3.1 and Section 5.5) and N is the total number of simulated showers at a true energy of E. Figure 5.16 shows the (effective) collection area as a function of shower energy for different zenith angles. The telescope multiplicity is ≥ 2. One can see that the effective areas for different zenith angles stay almost constant at higher energies. This is because the detection probability for showers with energies higher than ≥ 1 TeV is very near to 1 for almost all impact distances. The cut efficiencies of the analysis cuts are shown in Figure 5.17 (top-right) for quality cuts, (bottom-left) for shower cuts, and (bottom-right) for scaled cuts, i.e. MSW-, MSL-cut and an orientation cut, the so-called Θ^2-cut (see also Section 6.4), where in this context Θ^2 is the square of the angular distance between the source position and the reconstructed shower direction.

The detection rates shown in Figure 5.18 are obtained using the relation $\Gamma(E_i^{Reco}) \;=\; \Phi(E_i) \cdot A_{coll}(E_i^{Reco})$, under the assumption that $\Phi(E_i) \sim E_i^{\alpha}$, where α is the spectral index of the Crab Nebula (-2.59). After applying the cuts the rate substantially drops at all zenith angles by 30% - 40%, but the shape of the distributions doesn't change. Combined rates for various zenith angles with the same telescope multiplicity is shown in Figure 5.19.

In Figure 5.20, α is varied ($\alpha = -2.0, -2.59, -2.9$) to see if it causes any changes in the rate. Detection rates obtained for different spectral indices do not vary too much around the threshold. However, they vary slightly at higher energies, where the rate drops to zero.
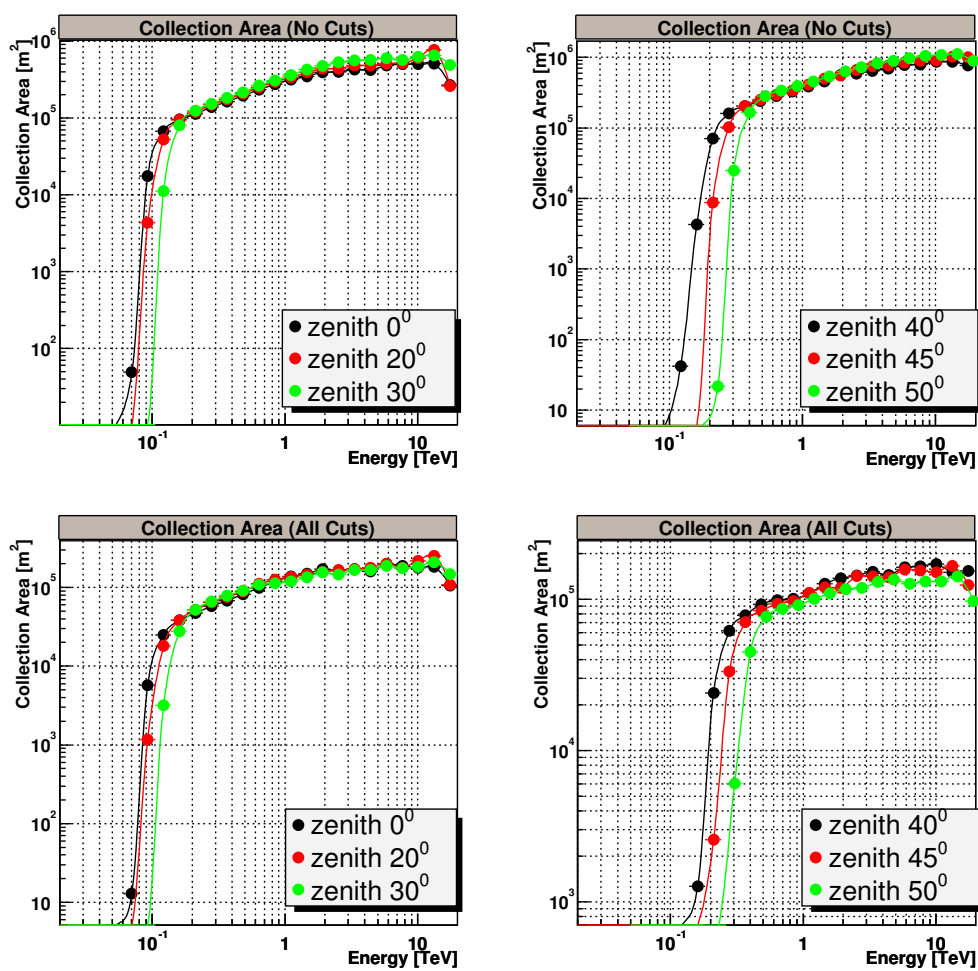
Abbildung 5.16: The top-left plot and the bottom-left plot are the collection areas for the small zenith angles (i.e. 0°, 20°, 30°) before and after cuts, respectively. The top-right plot and the bottom-right plot are the collection areas for the large zenith angles (i.e. 40°, 45°, 50°) before and after cuts, respectively.
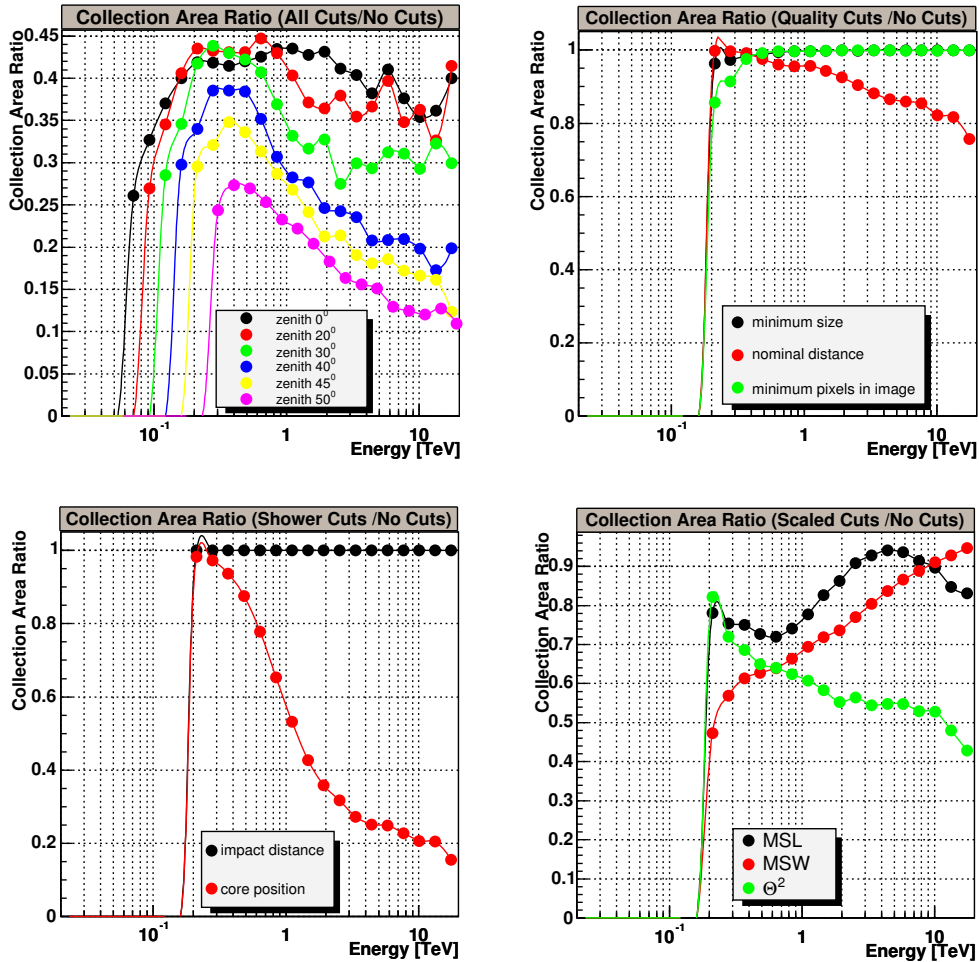
Abbildung 5.17: Cut efficiencies used in the analysis of the Crab Nebula data. Simulated Monte Carlo events for a spectral index of -2.0 are used to produce the collection areas. The top-left plot shows the overall cut efficiency for different zenith angles. The top-right plot shows the efficiencies of quality cuts for zenith $45°$. The bottom-left plot shows the efficiencies for the impact distance cut and the shower core cut for zenith $45°$. The bottom-right plot shows the efficiencies for the exclusive application of MSW-cut, MSL-cut, and Θ^2-cut (see text) for zenith $45°$.
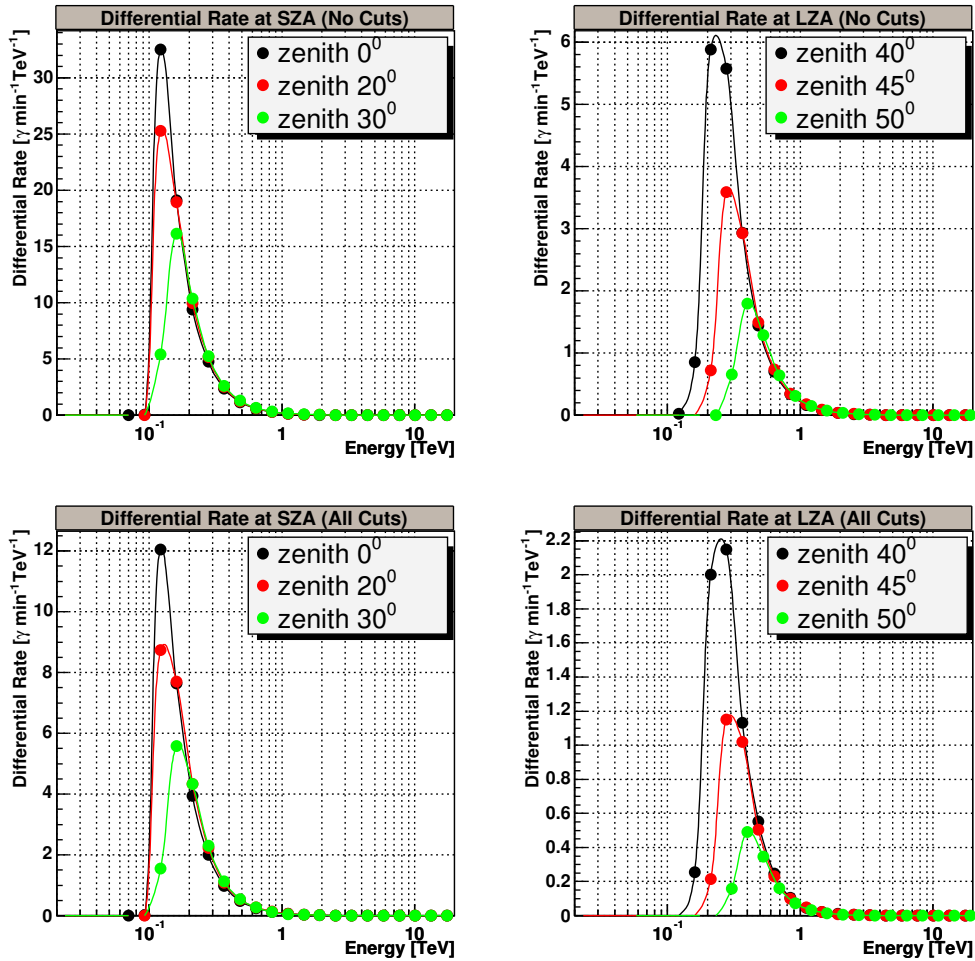
Abbildung 5.18: Detection rates produced using the collection areas given in Figure 5.16 on the bottom-left plot and the bottom-right plot for the energy spectral index of −2.0, reweighted to −2.59. The top-left plot shows the rates at small zenith angles (SZA = 0°, 20°, 30°) before cuts and the bottom-left plot after cuts. The top-right plot and the bottom-right plot show the rates for the large zenith angles (LZA = 40°, 45°, 50°) before and after cuts, respectively.
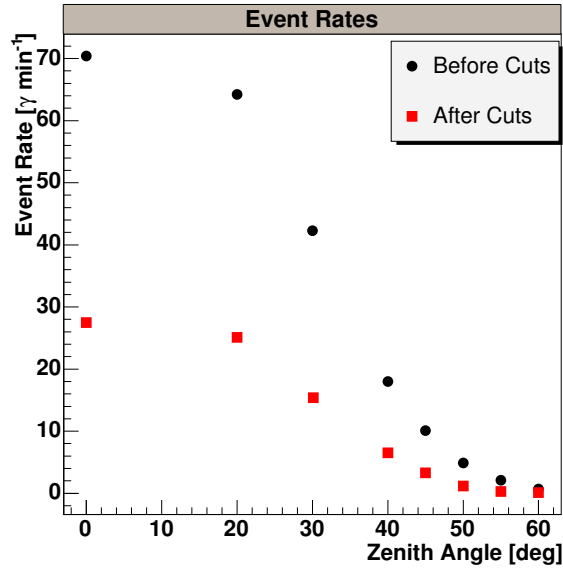
Abbildung 5.19: Rates for events triggered with a telescope multiplicity of $\geq$ 2 before cuts and after cuts for various zenith angles.

The energy threshold, E_{th}, is the energy at which the curve for the detection rate reaches a maximum. Table 5.2 summarizes the energy thresholds found for various zenith angles and telescope multiplicity of $\geq$ 2 before and after cuts. The energy thresholds in Table 5.2 are rough estimations obtained from histograms shown in Figure 5.18. The energy threshold is the center of the bin with the maximum number of entries, and the error on the energy threshold is the half of the width of this bin. The energy bins are logarithmic. One can see that the energy threshold increases with zenith angle. Furthermore, the cuts increase the energy threshold for higher zenith angles.

Using the collection areas calculated here for each zenith angle, the differential spectrum of the Crab Nebula can be reconstructed. This is done in the last chapter. The rough estimations of the detection rates derived from the simulations can be used to compare with the detection rates obtained from the observations.
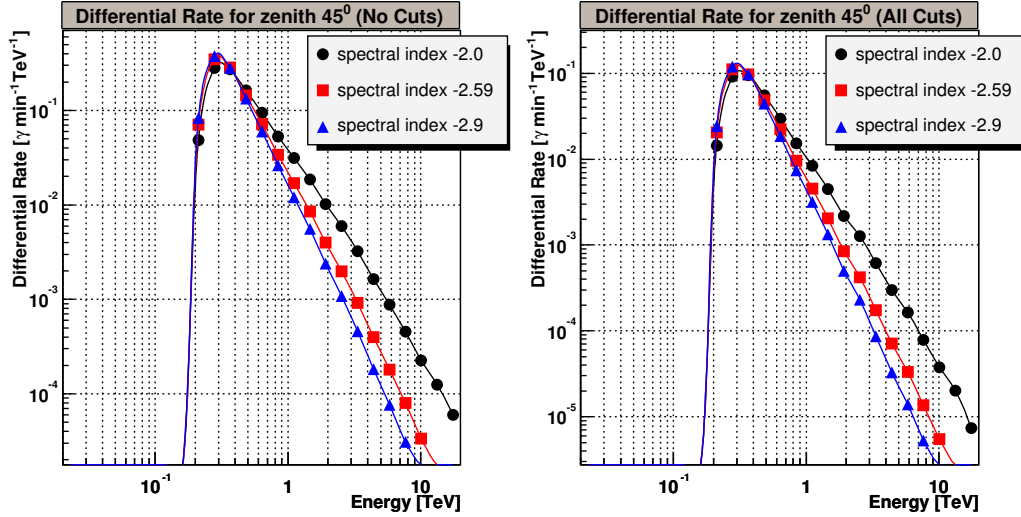
Abbildung 5.20: Detection Rates obtained for different spectral indexes. The left-plot shows rates produced with three different spectral indexes $(-2.0,$ $-2.59, -2.9)$ before cuts for zenith angle 45°. The right-plot shows the rates produced with the same set of spectral indices after cuts.

Tabelle 5.2: Energy thresholds before and after cuts as functions of zenith angles and for a telescope multiplicity ≥ 2 telescopes. The energy threshold values are obtained from histograms shown in Figure 5.18. The energy threshold is the center of the bin that has the maximum number of entries, and the error on the energy threshold is the half of the width of this bin.

Zenith Angle [deg]	Energy Threshold Before Cuts [GeV]	Energy Threshold After Cuts [GeV]
0	121±16	121±16
20	121±16	160±22
30	160±22	160±22
40	211±29	278±38
45	278±38	304±41
50	304±41	400±55
55	461±63	608±83
60	700±96	922±120

Kapitel 6

Analysis Results

The aim of the analysis shown in this Chapter is to establish the energy spectrum of the unpulsed emission of TeV γ rays from the direction of the Crab Nebula using the first stereoscopic data of the Crab Nebula obtained with the central trigger system of the H.E.S.S. telescope array. For the analysis, the implemented tools from Chapter 5 to reconstruct the shower geometry and the energy of showers, as well as collection areas are used. This chapter provides details of the used data set of the Crab Nebula, the signal extraction methods, optimization of the scaled image parameters, and determination of the energy spectrum of the Crab Nebula.

6.1   Data Quality Checks

It is essential to check the quality of the data before the analysis. Most of the parameters of the observation are very well known, i.e. zenith angle of the observation, number of active telescopes, and the calibration parameters of the system. However, there may be still some uncontrollable influences on the data quality, for example, bright stars in the FoV or weather conditions. If there are clouds, the Cherenkov light emitted by the air-showers is mostly absorbed. This can be monitored by the LIDAR, which is placed near the center of the telescope array. So, the bad-quality runs due to bad weather conditions can be determined off-line using these LIDAR-data.

Runs not obeying the criteria listed below are discarded from the analysis:

- Total number of events in a run should be at least 30,000 ,

- the RMS of the deviations of tracking position (in Alt/Az) from the nominal position should be less than 10 arc-seconds,

- the RMS of the fluctuations in the trigger rate must be less than 30%,

- number of broken pixels must be less than 150,

- number of pixels having HV (high-voltage) turned off has to be less than 50.

6.2   Image Cleaning

Before determining the Hillas parameters of an image in the camera, an image cleaning procedure is applied in order to remove the pixels, whose signals are produced by the night sky background or electronic noise.

This procedure works in the following way:

- Two *tail-cut values (L,U)* are set. L is the *lower tail-cut* and U is *upper tail-cut* value. Both of these values are threshold values in units of ph.e. for the individual pixel signals in the camera.

- Pixels with signals above L and below U are accepted under the condition that they have a neighboring pixel with a signal above U.

- Pixels having signal above U are included to the image.

- The signals of all other pixels are zeroed.

In the H.E.S.S. experiment the image cleaning procedure is applied for a specific set of tail-cuts. For the Crab runs the tail-cut values are selected to be 5 for lower tail-cut and 10 for upper tail-cut. Figure 6.1 A) and B) show the image in the camera before and after cleaning.

After Hillas parameters are produced, they are stored in *DSTs (Data Summary Tapes)s*, which only contain information on the Hillas parameters, shower parameters, as well as the telescope tracking information.

6.3   Data Set

Table 6.1 summarizes the DSTs for the Crab Nebula data set that have been used in this analysis. All selected Crab Nebula DSTs were taken in the 3 telescope configuration and with a 2 telescope multiplicity condition for the central system trigger. The trigger threshold required to be 3 pixels with a signal higher than 4 ph.e.. The dead time corrected observation time, which is the so-called *live time*, is used in the analysis. The zenith angle of observations are ranging from 45° to 50° .

a) Before cleaning   b) After cleaning
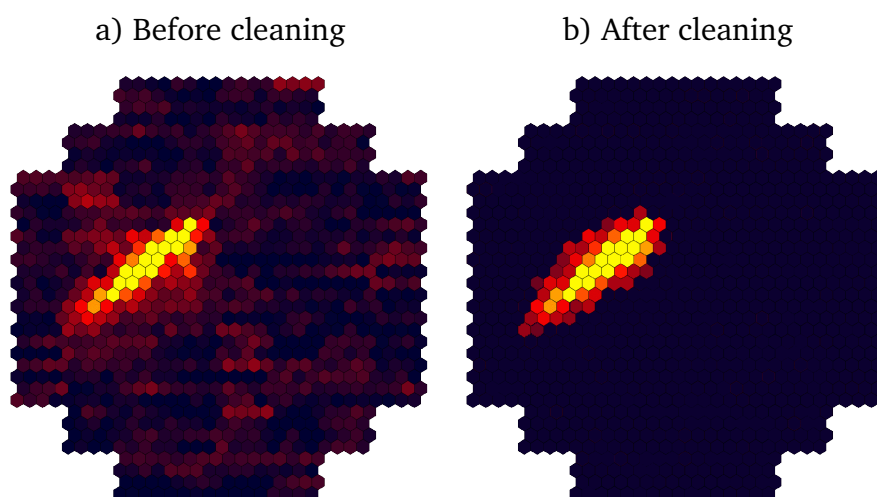
Abbildung 6.1: A shower image in the camera before (left) and after (right) image cleaning, where the signals caused by electronic noise and the NSB are zeroed. Colors give the intensity in units of ph.e. (Black is for zero ph.e.).

Tabelle 6.1: DSTs that passed the quality-check criteria for the Crab Nebula data set are shown in this table. All DSTs are stemming from runs taken in the 3 telescope configuration with 2 telescope multiplicity requirement by the central trigger system. The trigger threshold is taken as 2.5 pixels > 4 ph.e..

Run Number	Date	Start Time [UTC]	Duration [sec]	Telescope ID	Wobble Offset	Total Events
16266	23.10.2003	0:50:52	1672	2,3,4	$\delta+0.5°$	256729
16357	25.10.2003	0:59:16	1673	2,3,4	$\delta-0.5°$	284293
16358	25.10.2003	1:35:53	1673	2,3,4	$\delta+0.5°$	290730
16359	25.10.2003	2:06:57	1673	2,3,4	$\delta-0.5°$	299353
16360	25.10.2003	2:38:06	656	2,3,4	$\delta+0.5°$	115605
16403	26.10.2003	0:50:32	1681	2,3,4	$\delta+0.5°$	283430
16404	26.10.2003	1:21:38	1682	2,3,4	$\delta-0.5°$	298371
16480	28.10.2003	1:26:51	1683	2,3,4	$\delta+1.0°$	383712
16646	01.11.2003	1:34:32	1685	2,3,4	$\delta+1.0°$	379675
16647	01.11.2003	2:05:51	1682	2,3,4	$\delta-1.0°$	388156

6.4 Analysis Cuts

The following optimized quality cuts ([49]) and the selected shower cuts (5.5) are applied in this analysis to clean the sample:

- Image Amplitude $\geq$ 45 ph.e.,

- Distance $\leq 2°$,

- minimum number of pixels in the image ≥ 4,

- minimum number of triggered telescopes with data in an event ≥ 2,

- shower core position ≤ 300 m,

- 50 m $\leq$ shower impact distance ≤ 200 m.

Additionally, to select the γ-ray events out of the background events, two types of *γ-hadron separation cuts* are applied: The *scaled (MSW- and MSL-) cuts*, and the Θ^2-cut, which is the cut on the square of the angular distance (Θ) between the source position and the reconstructed shower direction. By cutting on Θ^2 value, only the reconstructed shower directions from the region around the source position are selected. So, Θ^2 value defines the radius of a circular signal region around the signal position. The set of optimized scaled-cuts (see Section 6.6 for details on the optimization procedure) and a loose cut on Θ^2 used in this analysis are given below:

- $0.05 \leq$ MSW ≤ 0.125,

- $0.05 \leq$ MSL ≤ 0.250,

- $\Theta^2 \leq 0.05°\,^2$.

Figure 6.2 shows the comparison of Width (top-left), Length (top-right), Amplitude (bottom-left) for the on-source events from the Crab Nebula and the simulated γ-ray images.
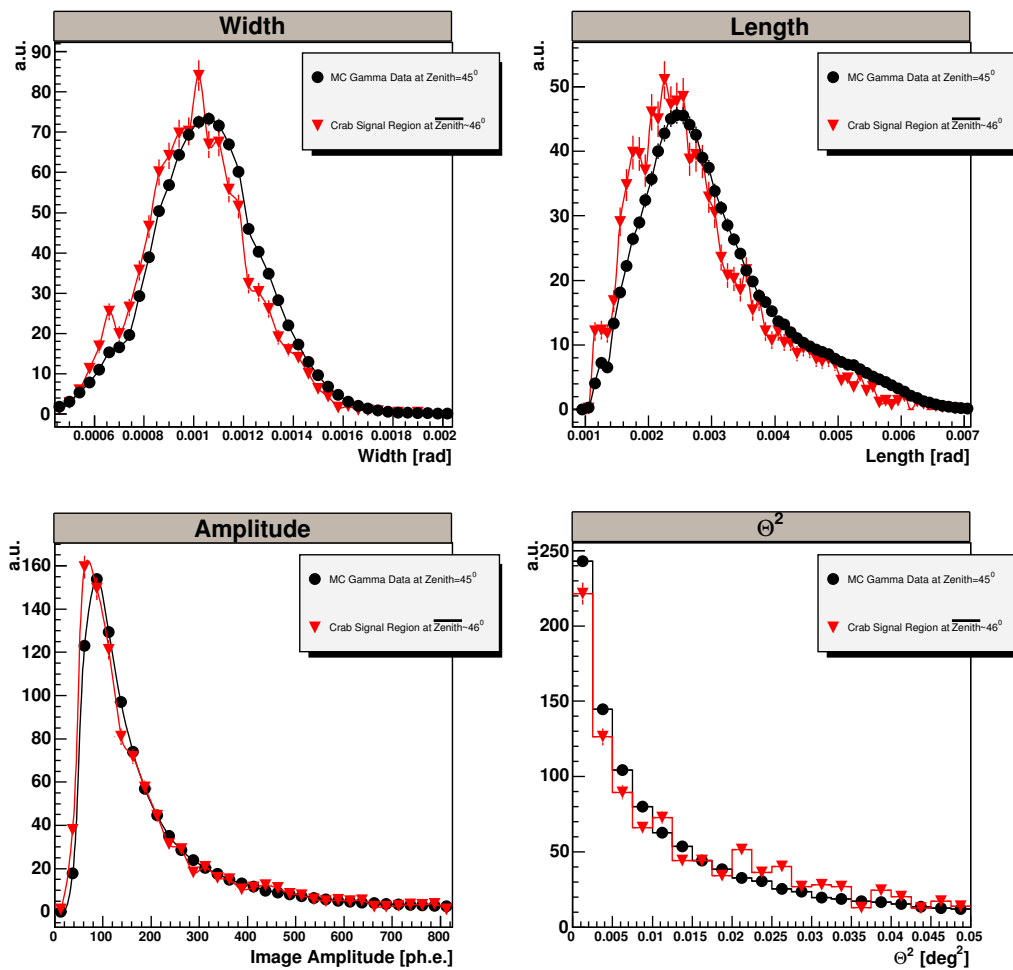

Abbildung 6.2: Distributions of Width, Length, Amplitude, and Θ^2 for the on-source events from the Crab Nebula, as well as for the simulated γ-ray images after all cuts.

6.5 Background Estimation and Signal Extraction

Because the FoV of the camera of the H.E.S.S. telescopes is large enough ($\sim 5°$), it is possible to estimate the signal and background in the same FoV for each wobble run of observing point-like sources or extended sources with limited angular size. To estimate the signal and background in a wobble run a *signal region* and *background region(s)* are selected within the FoV.

The signal region is taken around the source position with a certain radius, which corresponds to a cut on the Θ^2 parameter in a two dimensional representation of the FoV for a given type of coordinates (e.g. nominal-, Alt-Az-, RA-Dec system etc.). The Θ parameter can be found by computing the offset of the reconstructed shower directions in the nominal plane from the tracking position of the source. In order to minimize the error from the background, as many background events (i.e. regions) as possible have to be taken into account. Note that in the selection of the background region(s) the actual camera acceptance at different distances from the center of the field of view should be taken into account. Using signal- and background-regions of similar camera acceptance one can reduce the influence of the possible systematic effects in the background estimation. For that the radial offset of the background region from the camera center has to be the same as for the corresponding signal region. Presently several background models are available in the H.E.S.S. analysis software. They are illustrated in Figure 6.3. Some of them are also discussed in [146].

- *1:1 Signal:Background Regions:* In this background model the center of the background region is chosen as a mirror reflection of the source position in the FoV. This means the background region as well as the signal region is a certain distance, R, (e.g. R = 0.5°) away from the actual tracking position. This method is illustrated in Figure 6.3 (A). The chosen wobble position should not be too far away from the camera center, because of the decrease in the acceptance toward the camera edge. The relationship between the signal and background areas can be found from A_{ON}/A_{OFF}, which is denoted as ν. The value of ν is 1 for this model if the signal and background regions have the same radii. In Figure 6.2 (bottom-right) a distribution of the Θ^2 is used to compare simulated γ-rays with excess events from the signal region from the Crab Nebula after all analysis cuts using the *1:1 Signal:Background regions* method.

- *1:7 Signal:Background Regions:* In this method instead of one back-

ground region, 7 background regions are chosen (Figure 6.3 (B)). Each of these background regions as well as the signal region are located at the same distance, R, from the camera center and they have the same radii. The ν value for this method is $1/7$. In this method depending on the chosen distance R, the radius of the signal region and the background regions are determined. A compromise has to be found between not getting affected by the drop of the camera acceptance as mention above and getting a signal region, which is sufficiently big to collect enough γ-ray events. The maximum value that can be chosen for the Θ^2-cut is $0.02°$ in this model due to the limitations by the geometry. This method is ideal for analysis of point-like sources. It is used to extract the maximum signal from the Crab Nebula data. Table 6.3 summaries the values of significance obtained using this method.

- *Ring-background Method:* In this method the background is determined using a ring region around the inspected source position in the sky. Sky maps (i.e. two dimensional representations of the FoV for RA-Dec-System coordinates) for γ-like events and background events are produced applying the scaled cuts (Section 6.4). To produce the map of γ-like events the signal region is assumed to be a bin in the two dimensional distribution of γ-like events in the FoV or it is selected to be a circle with a certain radius r, center of which is the center of a bin on this distribution. To produce the background map, a ring region around each bin center is selected as the background region in the two dimensional distribution of the background events (Figure 6.3 (C)). The inner radius of the ring, r_1, is chosen to be bigger than that for the signal region, e.g. $r_1 = 0.3°$. The outer ring radius, r_2, is chosen to be $0.5°$. To avoid the source position to be selected as background region, the signal region around the position in the sky, where the γ-ray source is expected to be, is cut out before producing the distribution of background events. The produced maps for the γ-like events and background events are used to produce excess sky maps and significance maps (Figure 6.9) after correcting for the camera acceptance. Detailed information on this method are given in [70].

After applying one of the background estimation methods, the signal can be extracted using the number of events counted from the signal region, i.e. the on-source counts N_{ON}, and from the background region(s), i.e. the off-source counts N_{OFF}. The number of background events included in the signal region can be estimated as:

$$\hat{N}_B = \nu N_{OFF} \ , \tag{6.1}$$
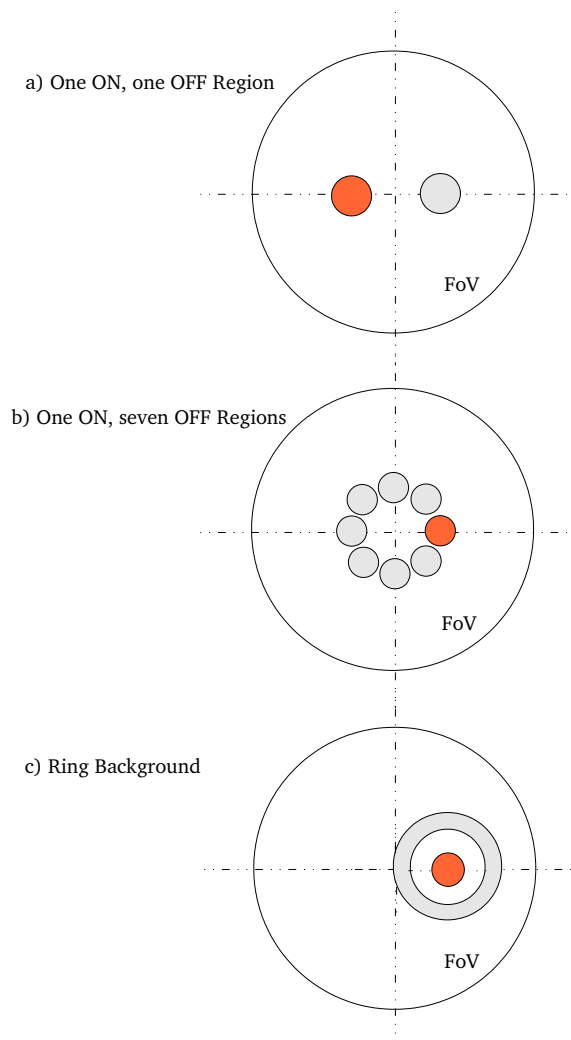
Abbildung 6.3: The three different background estimators are used in various steps of the analysis. The *1:1 Signal:Background Regions* method is shown in plot (A), where the signal region is given as the circle filled with red color, and the background region is the circle filled with gray color. The center of the signal region in positioned 0.5° away from the actual tracking position, and the center of the background region is the mirror reflection of the source position. The method shown in plot (B) is the *1:7 Signal:Background Regions* method. Compared to the method shown in plot (A), there are 7 background regions (circles filled with gray color) instead of only one. The method shown in plot (C) is the *Ring-background* method. In this method the background region is the ring (ring filled with gray color) surrounding the signal region (circle filled with red color).

where $\nu = A_{ON}/A_{OFF}$ with A_{ON} and A_{OFF} giving the total areas of the signal regions and background regions, respectively. The probable number of events that contributed to the signal can be given as

$$N_S = N_{ON} - \hat{N}_B = N_{ON} - \nu N_{OFF} \ , \qquad (6.2)$$

where N_S is also known as the number of excess γ-like events.

A positive observation of a source can also arise from statistical fluctuations. There have been various methods developed to estimate the statistical reliability of the signal. The significance, S, of a signal using the Li & Ma ([118]) approach is given as the following:

$$S = \sqrt{2} \ \left[N_{ON} \ \ln \left(\frac{(1 + \nu)N_{ON}}{\nu(N_{ON} + N_{OFF})} \right) + \right.$$
$$\left. N_{OFF} \ \ln \left(\frac{(1 + \nu)N_{OFF}}{(N_{ON} + N_{OFF})} \right) \right]^{1/2} . \qquad (6.3)$$

This formula is used throughout the thesis to calculate the significance of signals.

6.6   Optimization of the Scaled Cuts

The optimization of the *scaled cuts* is performed to yield the expected maximum significance per hour of observation using the *1:1 Signal:Background* method. The data used for optimization consists of Monte Carlo γ-ray simulations at zenith angle of $45°$ with an energy spectral index of -2.59 and the real off-source data sample, which contains higher statistics compared to simulated background data. Figure 6.4 (left) and (right) shows the MSW- and MSL-distributions before the scaled cuts. The shape of the MSW(MSL)-distribution of the off-source data (black markers) is the same as the one for the simulated background events (red histogram). In this work the optimization procedure is done in three steps as listed below:

- *Optimizing the MSW cut:* A loose Θ^2-cut of $\Theta^2 \leq 0.04°\ ^2$ is used and the upper MSW-cut is optimized, which is found as 1.125. The lower MSW-cut is taken as 0.05. These two cuts used in the data analysis comprise the so-called *MSW box-cuts*, $0.05 \leq MSW \leq 1.125$.

- *Optimizing the MSL cut:* Again using the loose Θ^2-cut of $\Theta^2 \leq 0.04°\ ^2$, and the MSW box-cuts, the upper MSL-cut is optimized yielding 1.250. Likewise, 0.05 is used as the lower MSL-cut, and the *MSL box-cuts* are formed, which are then $0.05 \leq MSL \leq 1.250$.
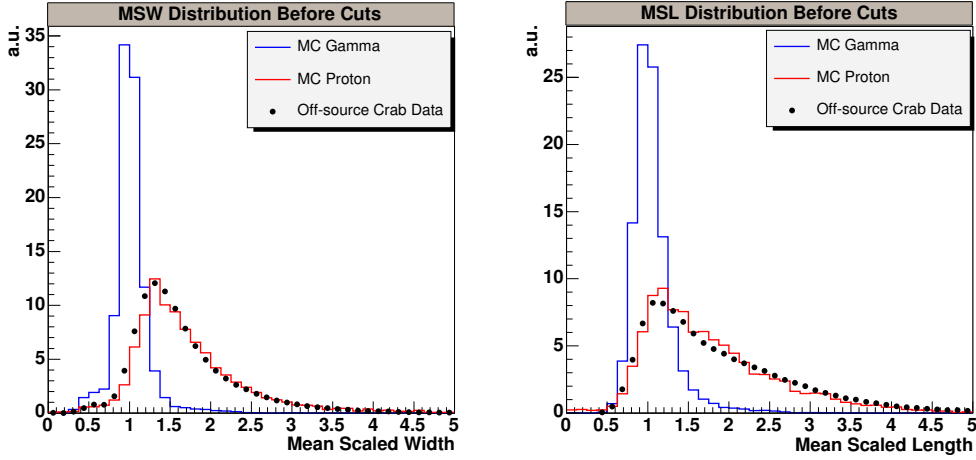
Abbildung 6.4: Mean Scaled Width (left) and Mean Scaled Length (right) distributions before the cuts. The MSW (or MSL) of the simulated γ-ray and background events for 45° zenith angle are shown in blue and red lines, respectively. The black markers are the background events extracted from the Crab Nebula data for a mean zenith angle of $\approx$46°.

- *Optimizing the Θ^2-cut:* Using the MSW box-cuts, and the MSL box-cuts, the optimized Θ^2-cut is found as $0.037°^{2}$.

The usual way to find the optimal sensitivity of the cut or a set of cuts is to maximize the quality factor, Q. Q can be written as

$$Q \; = \; \frac{\varepsilon_S}{\sqrt{\varepsilon_B}} \quad , \tag{6.4}$$

where $\varepsilon_S = N_S^{cut}/N_S$ is defined as the signal efficiency and $\varepsilon_B = \hat{N}_B^{cut}/\hat{N}_B$ is defined as the background efficiency, and N_S^{cut} and $\hat{N}_B^{cut}$ are the number of signal events and background events counted after the cuts and $\hat{N}_B$ and N_S are given in Equations 6.1 and 6.2, respectively.

Equation 6.4 assumes that the standard deviation of the number of background events N_B is used as measure of the statistical error of the observed signal N_S, where the significance S is defined as follows:

$$S \; = \; \frac{N_S}{\sqrt{\hat{N}_B}} \; = \; \frac{N_S}{\sqrt{\nu N_{OFF}}} \quad , \tag{6.5}$$

and for $\nu \neq 1$, $\hat{N}_B$ does not follow a Poisson distribution. So, the variance is evaluated by $\sigma^2(\hat{N}_B) = \nu^2 N_{OFF}$ and the significance is defined as

$$S \; = \; \frac{N_S}{\sigma(\hat{N}_B)} \; = \; \frac{N_S}{\nu\sqrt{N_{OFF}}} \quad . \tag{6.6}$$

However, in both Equation 6.5 and Equation 6.6 only the statistical fluctuations of the background counts N_{OFF} are considered and not that of N_{ON}. Therefore, the statistical error of the signal N_S is underestimated and consequently the significance is overestimated. If the statistical fluctuations of N_{ON} are taken into account, Equation 6.5 can be modified as follows:

$$S = \frac{N_S}{\sqrt{\nu(N_{ON} + N_{OFF})}} \quad . \tag{6.7}$$

In the case that the signal is strong ($N_{ON} >> N_{OFF}$), then $N_S \simeq N_{ON}$, and so Equation 6.7 for $\nu = 1$ (i.e. *1:1 Signal:Background* method is used to obtain the energy spectrum. For this background method $\nu = A_{ON}/A_{OFF} = 1$.) takes the following form:

$$S = \frac{N_S}{\sqrt{\nu(N_S + N_{OFF})}} \quad , \tag{6.8}$$

N_S and N_{OFF} can be rewritten as

$$N_S = \tilde{N}_S \, \varepsilon_S \;\; , \;\; N_B = \tilde{N}_B \, \varepsilon_B \;\; , \tag{6.9}$$

where $\tilde{N}_S$ is the number of excess events expected per hour of live-time from the on-source region and $\tilde{N}_{OFF}$ is the number of background events collected per hour of live-time from the off-source region. Accordingly the quality factor can be rewritten as

$$Q = \frac{\tilde{N}_S \, \varepsilon_S}{\sqrt{\tilde{N}_S \, \varepsilon_S \, + \, \tilde{N}_B \, \varepsilon_B}} \quad \mathrm{hrs}^{-1/2} \quad . \tag{6.10}$$

The background rate derived from the Crab Nebula runs is approximately 1.08×10^6 background-events per hour. The γ-ray rate per hour for a zenith angle of $45°$ is measured as 20.17 γ-ray events per minute.

On the top-right plot in Figure 6.5 the behavior of the quality factor is shown for the cuts applied to the events in each MSW-bin, while optimizing the MSW-cut. The quality factor depends on the γ-ray and proton efficiencies, which are determined after the application of the MSW-cut. The efficiencies for each MSW-bin are calculated and are shown on the bottom-right plot in Figure 6.5. The change in the quality factor and the calculated γ-ray and background efficiencies for MSL-cuts are given on the (top-left) and on the bottom-left plots of Figure 6.5, respectively.

The optimized Θ^2-cut is not used in the spectrum evaluation procedure. It is replaced by a substantially looser Θ^2-cut of $0.05°$ ^{2} in order to achieve a

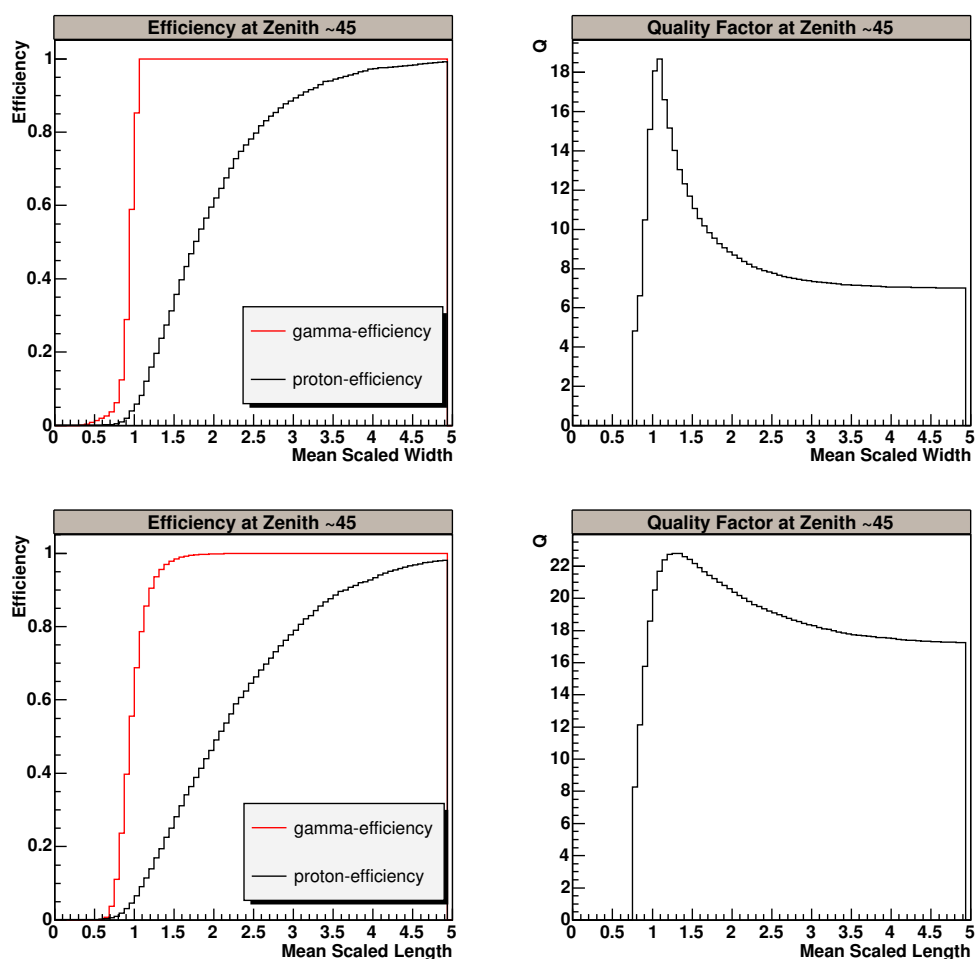Abbildung 6.5: The top-left and the bottom-left plots show the cut-efficiency distributions for γ-events (red line) and background events (black line) used to optimize the MSW- and MSL- cuts, respectively. The top-right and the bottom-right plots show the quality factor distributions used in optimization of the MSW- and MSL- cuts, respectively. Further discussion on optimization is given in the text.

Tabelle 6.2: The signal and background efficiencies after applying the MSW and MSL box-cuts for an event sample with zenith angle of 45°. The efficiency is changing insignificantly with the zenith angle or shower energy.

	ε_S [%]	ε_B [%]
MSW box cuts	87	19
MSL box cuts	92	6

higher acceptance of the γ-ray events. The γ-ray and background efficiency after cuts are shown in Table 6.2. Figure 6.6 (left) shows the separation of the signal from the background events in the MSW-parameter space after the optimized box-cuts for MSL and the loose Θ^2-cut. The black histogram shows the entries from the signal region of the Crab Nebula data, which also may contain background events. The red histogram shows the entries from the selected background region of the Crab Nebula data. The difference between these two histograms gives the green histogram, which contains only the γ-ray excess events. This green histogram is compared with a MSW-distribution of simulated γ-ray events in Figure 6.6 (right). One can clearly see that the distributions overlap onto each other, and both of them are distributed around 1 showing the typical property of γ-like events in MSW-parameter space.

6.7 Detection of the Crab Nebula

In Figure 6.7 (from top to bottom) the on-source and the normalized off-source distributions of Θ^2 for all Crab Nebula data in the 2, 3 and ≥ 2 hardware-stereo configuration are given. The Θ^2-distribution of background is as expected flat, and there is a clear excess in on-source distributions. The red line on the bottom plot shows the Θ^2-cut at $0.05°^2$ and the excess of on-source events corresponds to the observed signal.

Table 6.3 shows the results from all the 10 DSTs on the Crab Nebula obtained with the *1:7 Signal:Background regions* method by applying only the quality cuts. The results are produced for telescope multiplicities of 2, 3, and ≥ 2. The sensitivity drops for lower multiplicity of telescopes. Figure 6.8 gives the rates and significances per observation run. The total background subtracted signal is about 51.3 standard deviations. Figure 6.9 (left) shows the two-dimensional sky map of the excess observed in the direction of the Crab Nebula. On the right plot the two-dimensional sky significance map is given. Both of these maps are produced using the ring-background model,
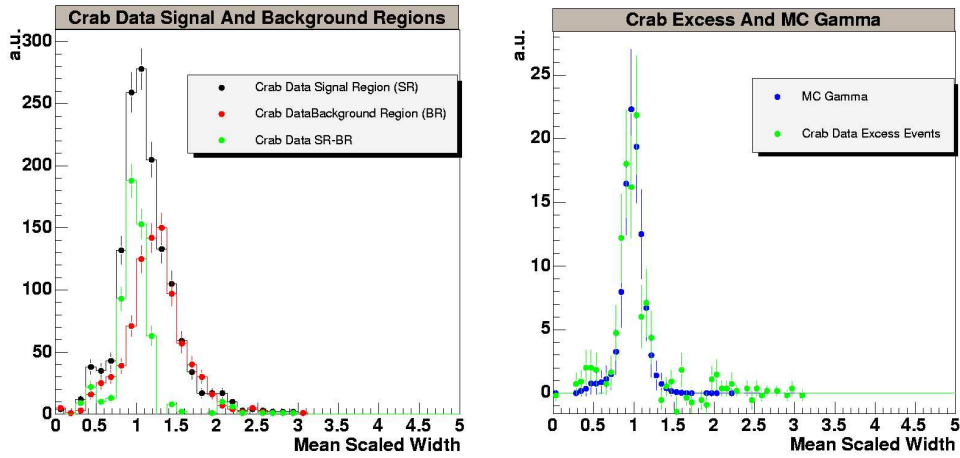
Abbildung 6.6: On the left plot MSW distributions from signal (black markers) and background (red markers) regions of the recorded Crab Nebula data (mean zenith angle of $\approx 46°$) and the γ-ray excess (green markers) distribution resulting from the difference between these two distributions are plotted. On the right plot, MSW distribution produced from the Monte Carlo γ-ray events (blue markers) (at zenith angle of $45°$) is compared with the MSW distribution of the Crab-excess events (green markers).

and in both of the maps the bins are correlated. This means that the signal region is not only one bin but it is a circular region with a small radius r around that bin. The shape of the excess distribution is characteristic for a point source. A fit applied ([126]) to an uncorrelated excess map gives the position of the TeV γ-ray region to be at RA:5h34m32.2s and Dec:22d0'35" .

6.8 Energy Spectrum of the Crab Nebula

For the reconstruction of the energy spectrum of the Crab Nebula, the *1:1 Signal:Background* method is used for the background estimation, because a single background region with a Θ^2-cut of $0.05°^2$ (compared to the other two background methods) provides a high acceptance of the γ-ray events from the source, which is important for the reconstruction of the energy spectrum. Table 6.4 summarizes the cumulative excesses, rates, significances, sensitivities obtained for all the Crab data applying all cuts including shower cuts and without shower cuts. In Figure 6.10 (right), the γ-ray excess events after all cuts are compared with the number of γ-ray events obtained after the same cuts from the Monte Carlo simulations for a zenith angle of $45°$. There is an overall agreement between Crab data and simulated data.
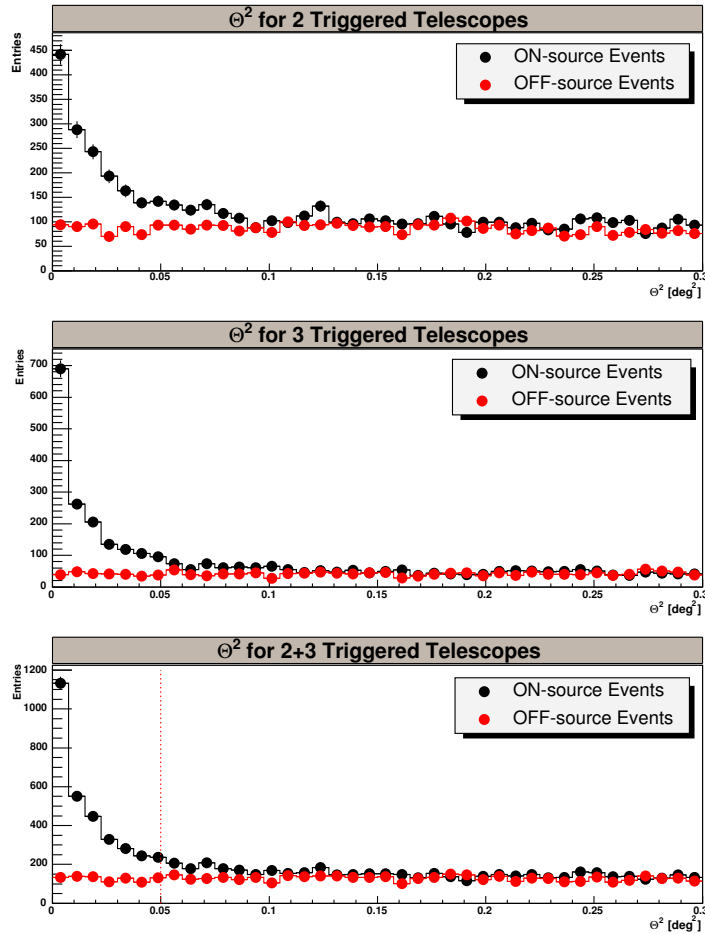
Abbildung 6.7: The *1:1 Signal:Background region method* is used to obtain the Θ^2-distributions from the on-source and off-source events from the observations of the Crab Nebula for 2, 3 triggered telescope events (upper plot and middle plot) and for ≥ 2 triggered telescope events (bottom plot). The line on the bottom plot shows the Θ^2-cut value used in this analysis.
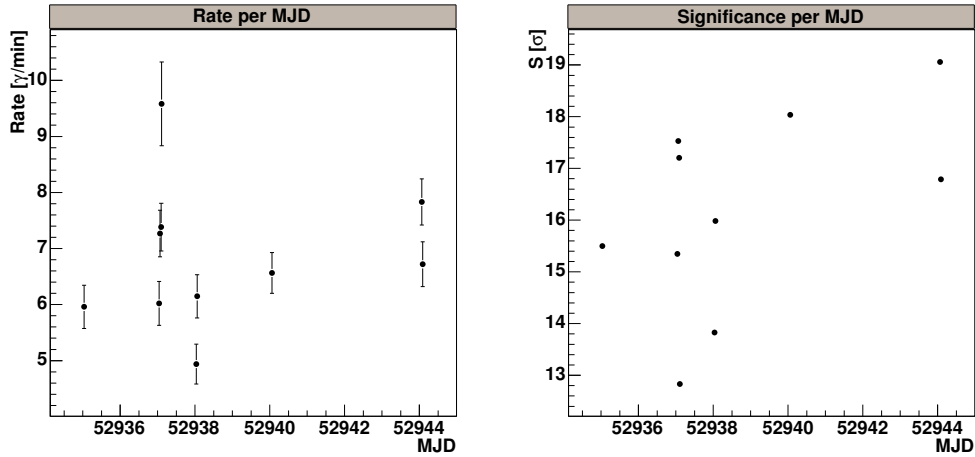
Abbildung 6.8: The rate (left plot) and the significance (right plot) obtained for each observational run using *1:7 Signal:Background regions* method (Section 6.5).
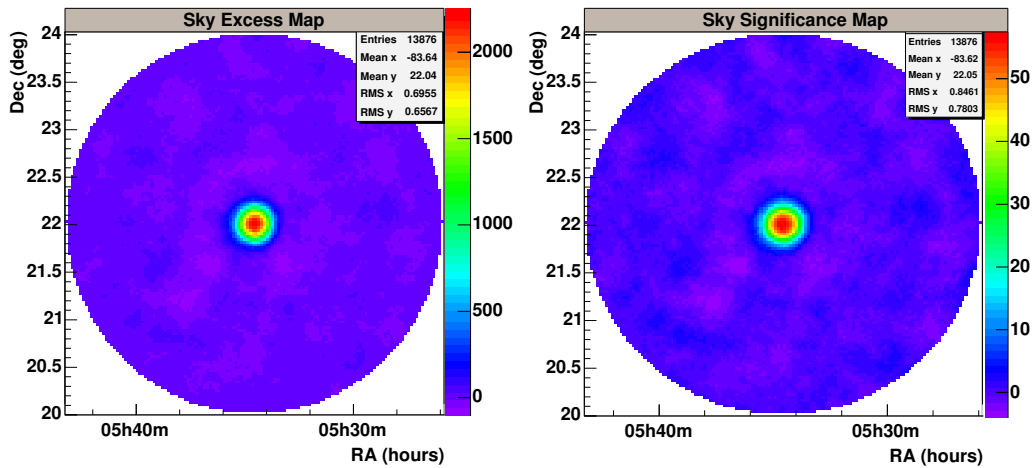
Abbildung 6.9: The two-dimensional excess (left) and significance (right) distributions of the Crab Nebula, produced using the ring-background method implemented into the standard H.E.S.S. analysis software.

Tabelle 6.3: Results obtained with the *1:7 Signal:Background regions* method (Section 6.5) using 10 DSTs taken on the Crab Nebula without applying any shower-cuts. Θ^2-cut value is $0.02°$ ^{2}. The *Ring-background method* gives similar results.

Telescope Multiplicity	Live-time [hrs]	Cumulative Excess	Significance [σ]	Sensitivity [$\sigma/\sqrt{hrs}$]	Rate [γ/min]
2	4.03	631±21	27.4	13.6	2.60±0.09
3	4.03	975±19	46.5	23.1	4.03±0.08
2+3	4.03	1606±29	51.3	25.5	6.63±0.12

Tabelle 6.4: Results given for *1:1 Signal:Background regions* method (Section 6.5) applied to all DSTs and only to those DSTs with a wobble distance of $\pm0.5°$. The cumulative excess events that passed all cuts including shower cuts and without shower cuts, and the corresponding values of significance, sensitivity, and rate are shown.

| Number of Runs; Applied Cuts	Live-time [hrs]	Cumulative Excess	Significance [σ]	Sensitivity [$\sigma/\sqrt{hrs}$]	Rate [γ/min]
$\delta\pm0.5°$ and $\pm1.0°$					
10;no shower cuts	4.03	2549±68	37.4	18.6	10.53±0.28
10;all cuts	4.03	1058±35	29.0	14.4	4.37±0.14
$\delta\pm0.5°$					
7;no shower cuts	2.76	1260±16	28.7	17.2	7.60±0.20
7;all cuts	2.76	700±32	22.7	13.6	4.40±0.19

Figure 6.10 (left) shows γ-ray rates plotted for various wobble angles (e.g. for all DSTs, DSTs only with $\delta \pm 0.5°$ or with $\delta \pm 1.0°$), and with all cuts that contain the shower cuts and that without shower cuts.

The energy threshold values given in Table 6.5 can be compared with the ones obtained from the simulations (in Table 5.2). The energy threshold obtained from the simulated γ-ray events at a zenith angle of $45°$ after all cuts is 367 ± 50 GeV, and the energy threshold for the Crab Nebula data is 480 ± 66 GeV for $\delta\pm0.5°$ and 370 ± 50 GeV for $\delta\pm1.0°$ after all cuts. So, there is a slight shift in the energy threshold compared to the threshold energy for the simulated data.

The differential spectrum for a specific bin of reconstructed energy E_i^{Reco} can be found as

$$\frac{d\Phi}{dE}(E_i^{Reco}) = \frac{\Gamma(E_i^{Reco})}{\Delta E_i^{Reco} A_{coll}(E_i^{Reco})} \ , \tag{6.11}$$

where ΔE_i^{Reco} is the width of the energy bin E_i^{Reco} and $A_{coll}(E_i^{Reco})$ gives the
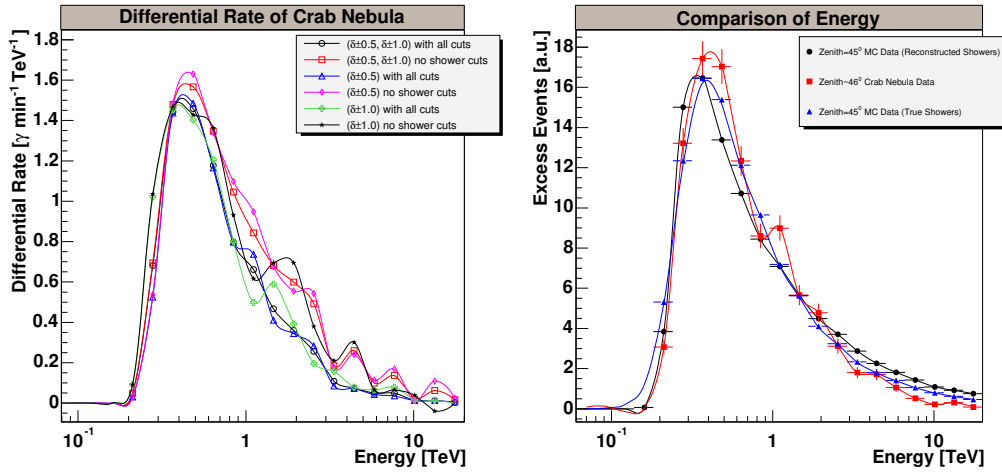
Abbildung 6.10: The differential rates for different samples of the Crab Nebula data and for different analysis cuts are shown on the left plot. The apparent shift of the energy threshold can be noticed (also shown in Table 6.5). On the right plot the number of excess events and the simulated γ-rays are plotted against the energy.

mean collection area for the energy interval ΔE_i^{Reco}. The calculated effective areas, shown in Figure 5.16, are produced after all cuts. The effective areas are calculated for 25 logarithmic bins of reconstructed shower energy. The differential flux values calculated for each energy bin are shown in Table 6.6.

6.9 Spectral Fits and Comparisons with other Measurements

Different types of fits (e.g. simple power-law, broken-power-law etc.) are applied to the calculated differential flux for DSTs with wobble angle of $\delta\pm0.5°$ after all cuts. Various ranges are fitted separately in order to observe the change in the spectral index, as well as to compare the present results with the results from other experiments published earlier.

Figure 6.11 shows *simple power-law (SPL) fits* obtained for various energy ranges in order to check the consistency of present results with other measurements. Let us consider that the spectrum obeys a simple power-law in the form of

$$\frac{d\Phi}{dE} = \Phi_0 \left(\frac{E}{E_0}\right)^\alpha, \tag{6.12}$$

Tabelle 6.5: The energy thresholds for different wobble angles are roughly estimated for a telescope multiplicity higher than 2 after all analysis cuts and by excluding shower-cuts. The energy threshold is the center of the logarithmic bin of the rate histogram (Figure 6.10 left-side) that has the maximum number of entries, and the error on the energy threshold is the half of the width of this bin.

Combination of Runs (Crab Nebula)	Energy Threshold for All Cuts [GeV]	Energy Threshold without Shower-Cuts [GeV]
$\delta\pm0.5°,\delta\pm1.0°$	480±66	480±66
$\delta\pm0.5°$	480±66	480±66
$\delta\pm1.0°$	370±50	370±50

where $E_0 = 1$ TeV. The results of such a fit are given as follows:

- *SPL Fit between 300 GeV and 20 TeV:* (Figure 6.11 (top))

  - $\Phi_0 = (3.36\pm0.47)\times10^{-11}$ cm^{-2}s^{-1}TeV^{-1},
  - $\alpha = -2.58\pm0.12$,
  - $\Phi(>1$ TeV$) = (2.11\pm0.29)\times10^{-11}$ cm^{-2}s^{-1},
  - $\chi^2/$ndf $= 3.8/13$.

Due to the fluctuations in the the energy threshold around 300 GeV, the energy spectrum is also fitted to a simple power-law from an energy of 450 GeV:

- *SPL Fit between 450 GeV and 20 TeV:* (Figure 6.11 (middle))

  - $\Phi_0 = (3.37\pm0.46)\times10^{-11}$ cm^{-2}s^{-1}TeV^{-1},
  - $\alpha = -2.59\pm0.12$,
  - $\Phi(>1$ TeV$) = (2.11\pm0.29)\times10^{-11}$ cm^{-2}s^{-1},
  - $\chi^2/$ndf$= 3.7/12$.

Without taking the last two highest energy bins into account, which contain very low statistics:
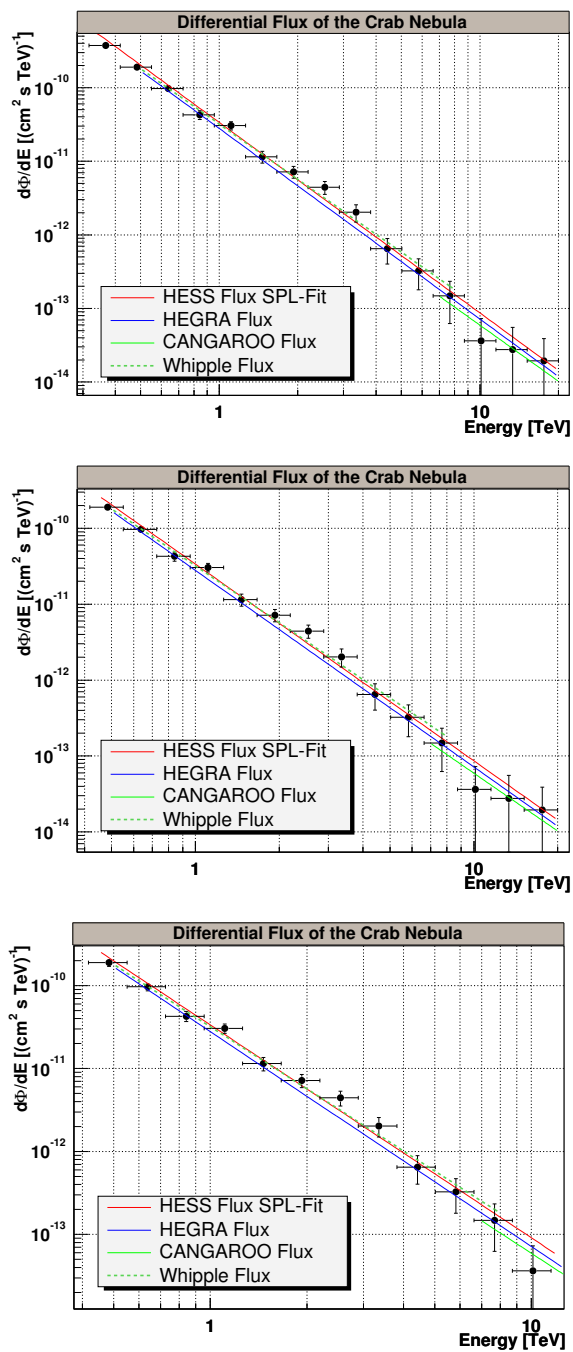
Abbildung 6.11: Energy spectrum fitted with a simple power-law (SPL) in the range between 300 GeV and 20 TeV shown by the upper-plot and between 450 GeV and 20 TeV shown by the plot in the middle and between 450 GeV and 10 TeV shown by the lower-plot. All analysis cuts are included.

Tabelle 6.6: Energy Spectrum extracted from the $\delta\pm0.5°$ data of the Crab Nebula using all analysis cuts. The statistic errors are also given.

Energy [TeV]	$d\Phi/dE$ [photon cm^{-2} s^{-1}]	σ_{stat} [photon cm^{-2} s^{-1}]	Significance $[\sigma]$
0.27	7.60×10^{-10}	1.22×10^{-10}	5.6
0.36	3.73×10^{-10}	0.41×10^{-11}	7.4
0.48	1.89×10^{-10}	0.19×10^{-11}	7.6
0.63	9.70×10^{-11}	0.10×10^{-11}	7.8
0.84	4.26×10^{-11}	0.05×10^{-12}	6.4
1.10	3.05×10^{-11}	3.98×10^{-12}	6.4
1.46	1.14×10^{-11}	2.10×10^{-12}	5.2
1.92	7.17×10^{-12}	1.31×10^{-12}	4.2
2.54	4.43×10^{-12}	8.86×10^{-13}	4.3
3.35	2.02×10^{-12}	5.37×10^{-13}	3.2
4.41	6.46×10^{-13}	2.44×10^{-13}	3.1
5.82	3.25×10^{-13}	1.45×10^{-13}	2.1
7.67	1.47×10^{-13}	8.53×10^{-14}	1.0
10.1	3.63×10^{-14}	3.63×10^{-14}	0.6
13.3	2.77×10^{-14}	2.77×10^{-14}	0.6
17.5	1.95×10^{-14}	1.95×10^{-14}	0.4

- *SPL Fit between 450 GeV and 10 TeV:* (Figure 6.11 (bottom))

    - $\Phi_0 = (3.33\pm0.42)\times10^{-11}$ cm^{-2}s^{-1}TeV^{-1},

    - $\alpha = -2.49\pm0.12$,

    - $\Phi(>1 \text{ TeV}) = (2.23\pm0.28)\times10^{-11}$ cm^{-2}s^{-1},

    - $\chi^2/\text{ndf} = 3.6/10$.

Looking at the χ^2/ndf values of the SPL fit, it can be concluded that the fit characterizes the Crab Nebula data very well. The results found for the simple power-law fits can be directly compared with the results from the previous measurements given by the HEGRA ([5], [9]), and the Whipple ([92]) experiments. The simple power-law fit applied to the Crab data taken by the Whipple experiment in the years 1988-1995 for the energy range from 500 GeV to 10 TeV are summarized as follows:

$$\frac{d\Phi}{dE} = (3.20 \pm 0.17 \pm 0.6) \times 10^{-11} \times$$
$$\left(\frac{E}{1 \text{ TeV}}\right)^{-2.49\pm0.06\pm0.04} \text{cm}^{-2} \text{ s}^{-1} \text{ TeV}^{-1} . \qquad (6.13)$$

The simple-power law fit applied onto the HEGRA data taken in 1997-1999 gives for the energy range from 450 GeV to 20 TeV the following representation:

$$\frac{d\Phi}{dE} = (2.79 \pm 0.02 \pm 0.5) \times 10^{-11} \times$$
$$\left(\frac{E}{1 \text{ TeV}}\right)^{-2.59\pm0.03\pm0.05} \text{cm}^{-2} \text{ s}^{-1} \text{ TeV}^{-1} . \qquad (6.14)$$

So, the H.E.S.S. Crab Nebula data agree very well within the statistical errors with these experiments. In the high energy range, extending up to 20 TeV including the HEGRA experiment's results and in the lower energy range extending up to 10 TeV including the results of the Whipple experiment all data are consistent within given statistical (and systematical) errors.
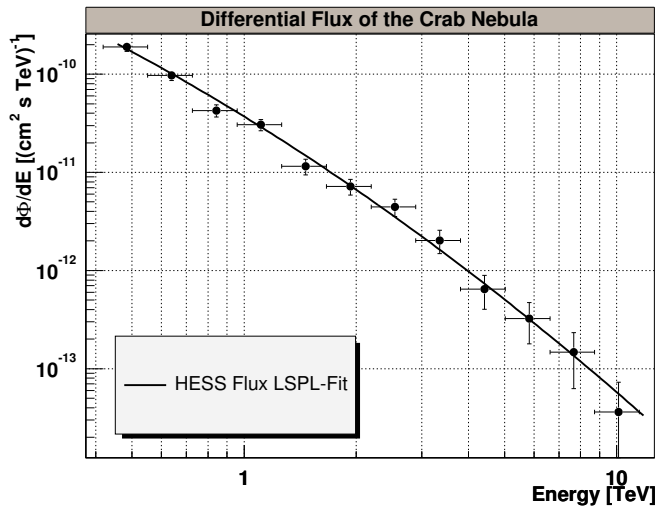
Abbildung 6.12: (Top) Energy spectrum with logarithmically steepening power-law (LSPL) fit between 450 GeV and 20 TeV including all cuts.

If we assume that the spectrum obeys a *logarithmically steepening power-law (LSPL)*, the form of the spectrum is written as follows

$$\frac{d\Phi}{dE} = \Phi_0 \left(\frac{E}{E_0}\right)^{\alpha - \beta \ \log E} , \qquad (6.15)$$

where E_0=1 TeV.

- *LSPL Fit between 450 GeV and 20 TeV:* The best fit is shown in Figure 6.12 (top), and the parameters of the fit are

    - $\Phi_0 = (3.70\pm0.50)\times10^{-11}$ cm^{-2}s^{-1}TeV^{-1},
    - $\alpha = -2.33\pm0.18$,
    - $\beta = 0.47\pm0.52$,
    - $\Phi(>1$ TeV$) = (2.77\pm0.38)\times10^{-11}$ cm^{-2}s^{-1},
    - $\chi^2/\mathrm{ndf} = 1.63/9$.

These results are consistent with the fits made by HEGRA ([5]). Fitting in an energy range of 0.45 - 20 TeV yields

$$
\begin{aligned}
\frac{d\Phi}{dE} &= (2.67 \pm 0.01 \pm 0.5) \times 10^{-11} \times \\
&\quad \left(\frac{E}{1 \text{ TeV}}\right)^{-2.47\pm0.1\pm0.05 \ - \ (0.11\pm0.10)\log E} \text{cm}^{-2} \text{ s}^{-1} \text{ TeV}^{-1} .
\end{aligned}
\tag{6.16}
$$

The LSPL-fit given by the Whipple group ([92]) in an energy range of 0.5 - 20 TeV gives the following

$$
\frac{d\Phi}{dE} = (3.25 \pm 0.14) \times 10^{-11} (E)^{-2.44\pm0.06 \ - \ 0.151\log E} \text{ cm}^{-2} \text{ s}^{-1} \text{ TeV}^{-1}
\tag{6.17}
$$

In the same way, a *broken power-law (BPL) fit* is applied for the energy range of 0.45 - 20 TeV, for which case the spectrum is assumed to be as follows:

$$
\frac{d\Phi}{dE} = \Phi_0 \ E_B^{(\alpha-\beta)} \left(\frac{E}{E_0}\right)^{\beta},
\tag{6.18}
$$

where E_0=1 TeV and E_B is the energy of the point of break in TeV.

- *BPL Fit between 450 GeV and 10 TeV:*

    - $\Phi_0 = (2.02\pm0.61)\times10^{-11}$ cm^{-2}s^{-1}TeV^{-1},
    - $\alpha = -1.38\pm0.34$,
    - $\beta = -2.59\pm0.13$,
    - $\chi^2/\mathrm{ndf} = 3.7/10$.

Figure 6.13 represents the data points of energy spectrum of the Crab Nebula derived in this thesis, which is multiplied by the factor of E^2 ($\nu F(\nu)$ plot) in the energy range between energies of 300 GeV and 20 TeV. Data points for the HEGRA ([5]), Whipple ([92]), CANGAROO ([159]), CAT ([16]) experiments, as well as for the Tibet air-shower detector ([11]) are also shown.
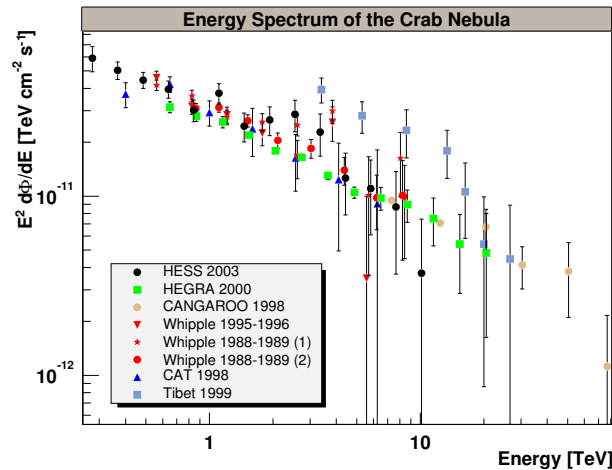
Abbildung 6.13: The data points of energy spectrum of the Crab Nebula folded by the factor of E^2 as derived in this thesis between energies 450 GeV and 10 TeV. The other data points are taken from the HEGRA experiment ([5]), the Whipple experiment ([92]), the Tibet air-shower array ([11]), the CAT Cherenkov-telescope([16])

6.10 Possible Systematic Errors

The accuracy of the measured trigger rate and flux depends on the accuracy of reconstruction of the energy of the shower. In order to measure the shower energy accurately, the simulated intensities of the camera pixels (PMTs) should match the measured intensities very well. To achieve this, the Monte Carlo model used for the air-shower simulations and the parameters used in the simulation of the detector response should be accurately tuned to the data.

The Monte Carlo simulations include atmospheric models, and the local geo-magnetic field properties to describe the physical conditions at the observation site. Using the atmospheric monitoring devices the temperature, pressure, humidity, aerosol level of the atmosphere are routinely measured.

Also light extinction can be determined. However, there are still large uncertainties in the atmospheric measurements. So, the atmosphere is the largest source of systematic errors in energy and flux measurements.

The efficiency profiles of parameters like mirror reflectivity and Winston cone reflectivity, response of the photomultiplier (e.g. quantum efficiencies), and photon-to-photoelectron conversion factor are set to convert the simulated Cherenkov light into intensities. By comparing the efficiencies from the measured parameters with the efficiencies, which are set in the simulations, the contribution to the systematic uncertainty of the measurements of image amplitudes can be studied. But the optical response of the mirrors and Winston cones can also be studied using the muon events [113]. The variation in the photomultipliers' single ph.e. gain due to changes in detector voltages can be regularly measured using the LED system. Also the response of the camera electronics including overall electronic gain and the pedestal levels can be monitored with the help of special calibration runs.

For the observational data, some additional systematic uncertainties can arise due to the possible drift of the system trigger conditions as well as due to the offsets in the FoV, and large zenith angles of observations.

Other possible systematic errors that can influence the determination of the flux are the reconstruction efficiency for a specific zenith angle, telescope multiplicity, and for the applied analysis cuts.

Each of the hardware components like photomultipliers (its quantum efficiency) or effective mirror area (the larger the mirror area the lower the energy threshold) etc., taken along with the trigger conditions determine finally the energy threshold of the telescope system. The systematic errors mentioned above can ultimately increase the actual energy threshold. The overall estimated systematic error for the flux is found to be $\Delta\Phi/\Phi \sim 20\%$ with a shift of the spectral index $\Delta\alpha \sim \pm 0.1$, [124].

6.11 Theoretical Interpretation of the Results

6.11.1 Energy Production Mechanisms

It was mentioned in Section 2.5 that the major source of the power in the Crab Nebula system is the Crab pulsar. It was also explained how the pulsar converts its rotational energy into electromagnetic radiation. It can be studied how the converted energy carried by the pulsar wind is transferred into the relativistic electrons filling the surrounding medium (plerion) independently from the knowledge of the conversion mechanism in the pulsar and the formation of the pulsar wind. The first attempt to understand the details

of the energetics of the Crab complex (the nebula and the pulsar), was the work of Rees and Gunn in 1974 [142]. These ideas were further improved by Kennel and Coroniti [106].

The multi-wavelength energy spectrum of the Crab Nebula is shown in Figure 2.10. It embraces a very broad range of the electromagnetic spectrum. Optical observations of the Crab Nebula showed that 60% of the total surface brightness of the nebula is concentrated in a region with a diameter of 10% of the average diameter of the remnant, and radio observations of the Crab Nebula gave evidence that the Lorentz factor of the bulk flow of the highly relativistic pulsar wind must exceed 10^4 at the edge of the SNR. But the expansion velocity of the Crab nebula was measured to be 5000 km/s. It was concluded that there must be *a strong shock inside the nebula*, which *slows down the bulk flow of the pulsar wind* so that the bulk velocity decreases across the shock and toward the edge of the SNR. The radius of the shock region is found to be ∼0.1 pc (10% of average diameter of the remnant) according to the calculations made by Rees and Gunn.

According to the model of Kennel and Coroniti, the spin-down luminosity of the pulsar is fractionally carried by plasma and magnetic energy densities. To derive the electron and magnetic field distributions in the entire system the wind and the accompanying magnetic field a magneto-hydrodynamic (MHD) model is used. A parameter σ is defined, which is the ratio of the magnetic energy density to the particle energy density upstream of the termination shock to explain the flow of fields and plasma across the shock, and out to the edge of the remnant ([3]). The value of σ varies between 0.001 and 0.01.

The energy range from 100 MeV to 500 MeV of the photon spectrum (Figure 2.10) is explained by the synchrotron emission of the relativistic electrons, which are accelerated to energies above 10^{15} eV through the termination of the stellar wind at the reverse shock in the nebula, in the model of Kennel and Coroniti [106].

The cutoff energy, E_c, of the synchrotron emission is related to the electron energy, E_e, ([99]). E_c is given by

$$E_c \; = \; \frac{3 \, \hbar \, c \, B_e \, E_e^2}{m^3 \, c^6} \quad , \tag{6.19}$$

where B_e is the average magnetic field of the Crab Nebula. Because the electrons are not observed directly, their spectral distribution has to be unfolded from the observed synchrotron spectra, which strongly depends on the magnetic field. A fixed value of the synchrotron luminosity corresponds to high magnetic field and low electron density, or vice versa.
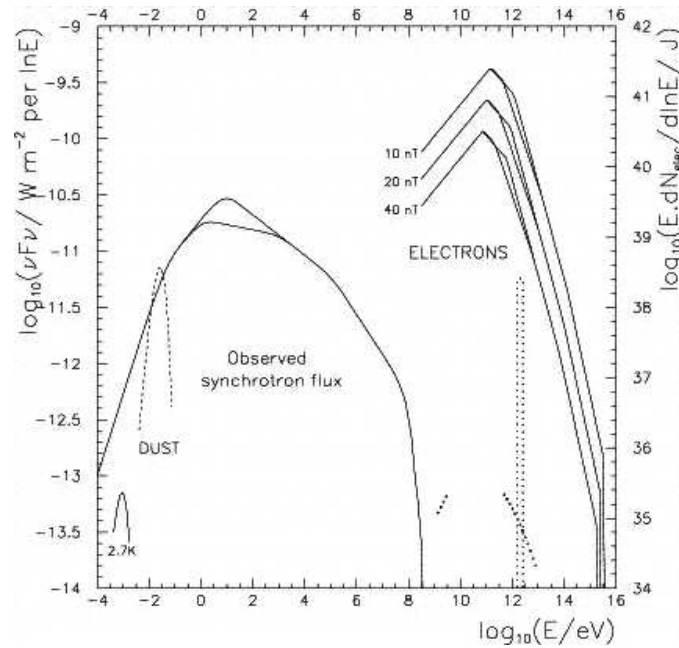
Abbildung 6.14: The measured flux of the synchrotron spectrum of the Crab Nebula (left solid line) and the deduced spectra for electrons (right solid lines) corresponding to the assumed magnetic field values of 10 nT, 20 nT, and 40 nT. The contribution from the far infra-red (FIR) or dust emission (dashed line) and the 2.7 K CMBR are scaled to show photon density relative to synchrotron photon density. For comparison, the non-synchrotron component in the energy range of 10^9 - 10^{13} eV (heavier dotted line) is given. Additional electrons in the relativistic wind before the termination shock (lightly dotted line) are estimated to contribute to the synchrotron spectrum. Figure is taken from [92].

Figure 6.14 shows the measured synchrotron spectrum of the Crab Nebula (left solid line). From the measured synchrotron spectrum and estimated average magnetic field values (10, 20, 40 nT) the electron spectra in Figure 6.14 (right solid lines) can be calculated ([92]). Figure 6.14 also shows the spectra of soft photons of far infra-red (FIR) (dashed line), and CMB radiation scaled to give photon density relative to the synchrotron photon density. The synchrotron photons dominate in density over all energies up to the cutoff energy.

VHE γ-rays are low-energy photons up-scattered by the relativistic electrons through inverse Compton scattering. The synchrotron spectrum of the Crab Nebula implies a presence of electrons with energies up to 10^{15} eV, which are potentially the seed electrons producing the TeV γ rays from the Crab
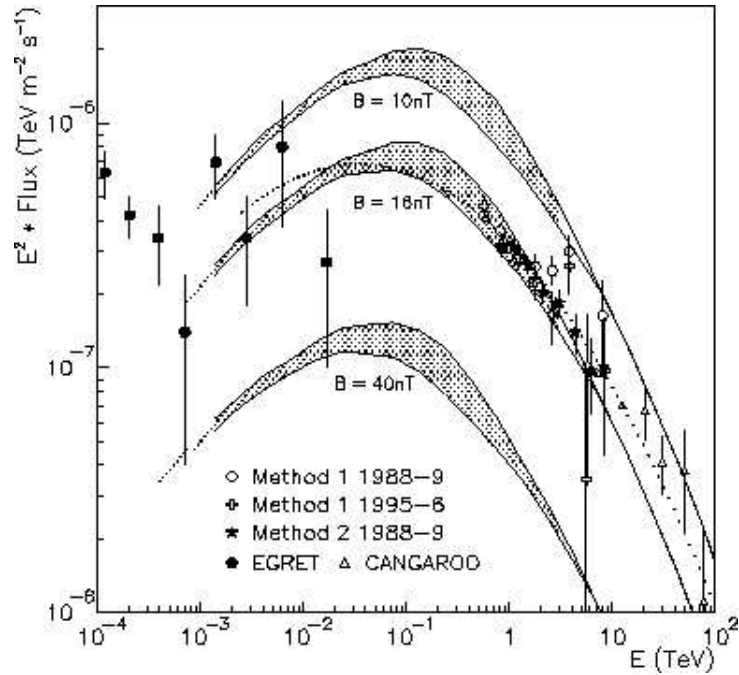
Abbildung 6.15: The inverse Compton component of the Crab spectrum for different magnetic field strengths deduced from the models. Models fitted to the data are from [2] and [54]. Figure is taken from [92].

Nebula. Models called *synchrotron-self-Compton (SSC)* explain the scattering of the synchrotron photons in the Crab Nebula to higher energies by the same electron population that produces the synchrotron photons. Also soft photons of far infra-red (FIR), and CMB radiation contribute at magnetic field values of 2×10^{-4} Gauss of the nebula according to [3], [9]. The VHE γ-ray energy bands correspond to the scattering in the energy range of 2 - 30 TeV for electrons and 0.005 - 0.3 eV for the soft photons ([3]).

Because the IC-flux is proportional to the electron density it follows that a higher magnetic field results in a smaller IC flux. The integral flux of γ rays above 1 TeV is found to vary as follows

$$\Phi_\gamma(> 1 \text{ TeV}) \ \propto \ B^{-\eta} \ , \tag{6.20}$$

where B is the estimated average magnetic field in the X-ray emitting synchrotron region and η is determined from the slope of the energy spectrum of synchrotron X rays. Figure 6.15 shows the IC spectrum predicted by Hillas et al. ([92]) together with various possible values of the magnetic field of the Crab Nebula that are found from the synchrotron spectrum shown in Figure 6.14. VHE γ-ray measurements can be used to constrain the value of

the magnetic field. In Figure 6.15 the data from the VHE γ-ray observations show that the VHE γ rays are scattered from the X-ray nebula close to the pulsar, where the average magnetic field is 0.16 mG and the electrons have energies higher than 1 TeV.

Comparison of HESS Crab Differential Energy Spectrum with Models
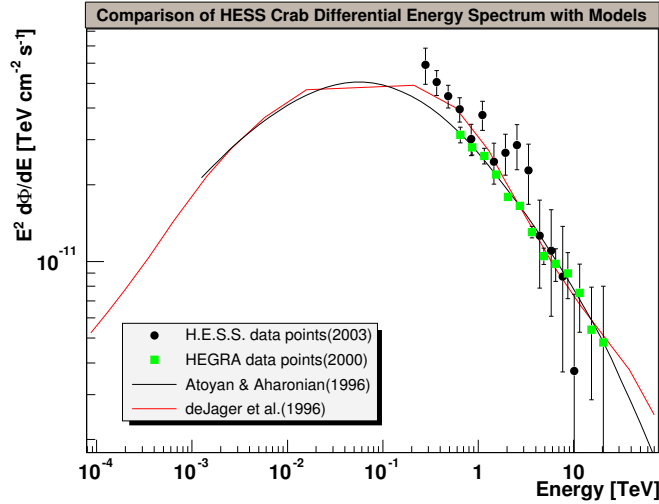
Abbildung 6.16: Energy spectrum shown between 0.1 GeV and 70 TeV for the Crab Nebula. The data points are from the HEGRA experiment (green markers) ([5]), and data of the H.E.S.S. experiment analyzed in this work (black markers). The curves represent the expected spectra from two synchrotron self-Compton (SSC) models of Atoyan and Aharonian (black curve) ([2]) and de Jager et al. (red curve) ([55]), respectively. For the second model the σ value is taken as 0.003.

6.11.2   Estimation of Magnetic Field

The measurements of fluxes in the TeV range can contribute to the accurate estimation of the magnetic field in the nebula. The advantage of measurements in TeV range is that the flux of IC photons around 1 TeV should essentially be constant over time scales of several decades, because the time needed for an electron to loose half of its energy due to synchrotron radiation is $\approx$200 years for a magnetic field strength of 0.2 mG in the nebula.

Figure 6.16 shows the data points for the energy spectrum of the Crab Nebula, as derived in this thesis between energies 300 GeV and 10 TeV, multiplied by the factor of E^2 . Two synchrotron self-Compton (SSC) model predictions are also shown from *Atoyan and Aharonian* ([2]) and *de Jager et al.* ([55]).

The model of *de Jager et al.* is a fit to the data from the EGRET satellite and ground-based VHE observations to the MHD models. This means that the γ-ray flux from the Crab Nebula at TeV energies can constrain the choice of the parameter σ. In Figure 6.16 the de Jager model (red line) assumes a σ value of 0.003, which gives a good agreement with the H.E.S.S. data.

According to Gould ([75]) it is possible to determine the average magnetic field in the nebula by assuming the spatial distribution of the magnetic field in the Crab Nebula. According to the calculations using the model of *Atoyan and Aharonian*, which is based on the MHD model of Kennel and Coronti ([107]), the average magnetic field, $\bar{B}$, can be calculated by

$$\Phi_\gamma(> \ 1 \ \text{TeV}) \ \simeq \ 8 \times 10^{-12} \ \left(\frac{\bar{B}}{0.3 \text{mG}} \right)^{-2.1} \ \text{cm}^{-2}\text{s}^{-1} \ , \qquad (6.21)$$

where the model predicts the mean value of the magnetic field to be 0.16 mG. The integral flux value obtained from the H.E.S.S. energy spectrum can be substituted into Equation 6.21, which gives an average magnetic field strength of

$$\bar{B} \ \simeq \ 0.18 \pm 0.01 \ \text{mG} \ . \qquad (6.22)$$

This value is also consistent with the value found from the Whipple measurements ([92]).

Summary

Data has been collected from the direction of the Crab Nebula in October and November 2003 with a 3 telescope configuration of the H.E.S.S. array. Selected good quality runs at offsets of $\delta\pm0.5°$ and $\delta\pm1.0°$ in the FoV have given a significance of 50 standard deviations in 4 hours.

For the detailed analysis of the Crab data Monte Carlo data sets of γ- and proton-induced air-showers have been produced. Comparing the image parameter distributions of the simulated γ-ray excess events with the on-source events from the Crab Nebula gives agreement between simulated and real data.

The method of reconstruction of the shower geometry and energy of the primary γ rays developed by the HEGRA experiment was implemented into the H.E.S.S. software environment. The algorithms were tested with the simulations produced for various zenith angles. After all analysis cuts, a resolution for the reconstruction of direction of the primary γ rays is found to be $0.15°$ per event, and the energy resolution is found to be around 14% for an energy range from 300 GeV to 20 TeV at zenith angle of $45°$. The energy resolution between 100 GeV and 20 TeV is around 20%. Because of the bias in the energy reconstruction up to energies around 300 GeV, the energies smaller than 300 GeV are excluded from the energy spectrum determination procedure. The events with energies higher than 5 TeV are mainly lost due to the cuts applied to the shower core position at 300 m and shower impact distance at 200 m. It is found that the higher the multiplicity of the triggered telescopes, the better the overall resolution of the direction, core position and energy of the selected γ-ray events.

The reconstruction algorithms were applied to the data obtained for the Crab Nebula. The energy spectrum was reconstructed between 300 GeV and 20 TeV. It was shown that the system of 3 telescopes is able to detect γ-ray showers down to 300-450 GeV. The energy threshold varies for the runs of the Crab Nebula with different values of offset in the FoV, and on different sets of cuts that are applied in the analysis. The differential energy spectrum

of γ rays in the range from 300 GeV to 20 TeV after cuts is found to be

$$\Phi(E) \;=\; (3.36 \pm 0.47) \times 10^{-11} \; E^{-2.58 \pm 0.12} \quad \text{cm}^{-2} \; \text{s}^{-1} \; \text{TeV}^{-1} \quad .$$

Because the energy threshold rises for the set of DSTs with wobble angle $\delta \pm 0.5°$ after all cuts to 480$\pm$66 GeV, the energy spectrum is fitted to a simple power-law over 450 GeV. The dependence of the reconstructed flux Φ to the energy E in an energy range of 450 GeV and 20 TeV is

$$\Phi(E) \;=\; (3.37 \pm 0.47) \times 10^{-11} \; E^{-2.59 \pm 0.12} \quad \text{cm}^{-2} \; \text{s}^{-1} \; \text{TeV}^{-1} \quad .$$

The error bars in the flux calculations only include the statistical errors. The integrated flux above 1 TeV is found as:

$$\Phi(E \; > \; 1 \; \text{TeV}) \;=\; (2.11 \pm 0.29) \times 10^{-11} \text{cm}^{-2}\text{s}^{-1} \quad .$$

These results agree with the results given by the HEGRA experiment and the Whipple experiment in years 1998-1999 within the statistical errors. The estimated systematic error on the flux determination is about $\Delta\Phi/\Phi \sim 20\%$ with a shift in the spectral index of about $\sim \pm 0.1$.

Finally, the energy spectrum of the Crab Nebula is compared with the synchroton self-Compton models in the TeV emission range. The magnetic field of the region, where the TeV γ rays are supposed to be produced, is calculated using the H.E.S.S. data of the Crab Nebula. The mean of the magnetic field within the Crab Nebula is found to be

$$\bar{B} \;=\; 0.18 \; \pm \; 0.01 \; \text{mG} \quad ,$$

which is compatible with the values predicted from the models and obtained from other experiments.

Appendix A

Definition of the Hillas Parameters

Assume that the ith pixel has coordinates $q_i = \{x_i, y_i\}$ (in radians), where the origin of the system is the center of the camera focal plane, and s_i is the intensity of the ith pixel. The summation of pixel intensities over all pixels making up the image in the camera gives the Image Amplitude, which is written as follows

$$\text{Image Amplitude} = \sum_i s_i \quad .$$

The following simple moments can be obtained from the intensity distribution in the camera:

$$\langle x^p \, y^q \rangle = \frac{\sum s_i x_i^p y_i^q}{\sum s_i} \quad ,$$

for $p, q = 1, 2, 3$. Distance from the image centroid of the image to the center of the field of view is the square root of the following expression

$$\langle \text{Distance} \rangle^2 = \langle x \rangle^2 + \langle y \rangle^2 \quad .$$

The second and third moments read

$$\sigma_{x^2} = \langle x^2 \rangle - \langle x \rangle^2 \ , \quad \sigma_{y^2} = \langle y^2 \rangle - \langle y \rangle^2 \ ,$$
$$\sigma_{xy} = \langle xy \rangle - \langle x \rangle \langle y \rangle \ ,$$
$$\sigma_{x^3} = \langle x^3 \rangle - 3 \langle x^2 \rangle \langle x \rangle + 2 \langle x \rangle^3 \ ,$$
$$\sigma_{y^3} = \langle y^3 \rangle - 3 \langle y^2 \rangle \langle y \rangle + 2 \langle y \rangle^3 \quad .$$

Using the definitions

$$k = \sigma_{y^2} - \sigma_{x^2} \quad ,$$

$$l = \sqrt{k^2 + 4\,\sigma_{xy}^2} \;,$$
$$m = \langle y^2 \rangle - \langle x^2 \rangle \;,$$
$$n = \sqrt{m^2 + 4\,\langle xy \rangle^2} \;,$$
$$u = 1 + \frac{k}{l} \;,$$
$$v = 2 - u \;,$$

Length and Width parameters are the RMS spread of the intensity distribution in the image along the major- and minor-axis of the image respectively. Then:

$$\langle \text{Length} \rangle^2 = \frac{\sigma_{x^2} + \sigma_{y^2} + l}{2} \;,$$
$$\langle \text{Width} \rangle^2 = \frac{\sigma_{x^2} + \sigma_{y^2} - l}{2} \;,$$

The Miss parameter of the image is the perpendicular distance between the center of the field of view and the major axis of the image. It is found by taking the square root of the following expression:

$$\langle \text{Miss} \rangle^2 = \frac{u\,\langle x \rangle^2 + v\,\langle y \rangle^2}{2} - \frac{2\,\langle xy \rangle\,\sigma_{xy}}{l} \;,$$

Alpha (α) is the angle between the line connecting the image centroid with the camera center and the major axis of the image (Figure 5.4). This parameter varies within the range from 0° to 90°, and it reads

$$\langle \text{Alpha} \rangle = \sin^{-1}\left(\frac{\langle \text{Miss} \rangle}{\langle \text{Distance} \rangle} \right) \;,$$

Azwidth parameter is the RMS spread of the light along the direction, which is perpendicular to the line connecting the image centroid with the center of field of view. It can be found as follows:

$$\langle \text{Azwidth} \rangle^2 = \frac{\langle x^2 \rangle + \langle y^2 \rangle - n}{2} \;.$$

ϕ in Figure 5.4, which is formulated in Equation 5.5 (Section 5.2.1), can also be written as follows:

$$\phi = \tan^{-1}\left(\frac{(k + l)\,\langle y \rangle + 2\,\sigma_{xy}\,\langle x \rangle}{2\,\sigma_{xy}\,\langle y \rangle - (k - l)\,\langle x \rangle} \right) \;.$$

The Asymmetry of the image can be found from the following equation:

$$\langle \text{Asymmetry} \rangle^3 = \frac{p}{\langle \text{Length} \rangle} \quad ,$$

where

$$p = \sigma_{x^3} \cos^3 \phi + 3 \sigma_{x^2 y} \sin \phi \cos^2 \phi + \\ 3 \sigma_{xy^2} \cos \phi \sin^2 \phi + \sigma_{y^3} \sin^3 \phi \quad .$$

Appendix B

Coordinate Transformations
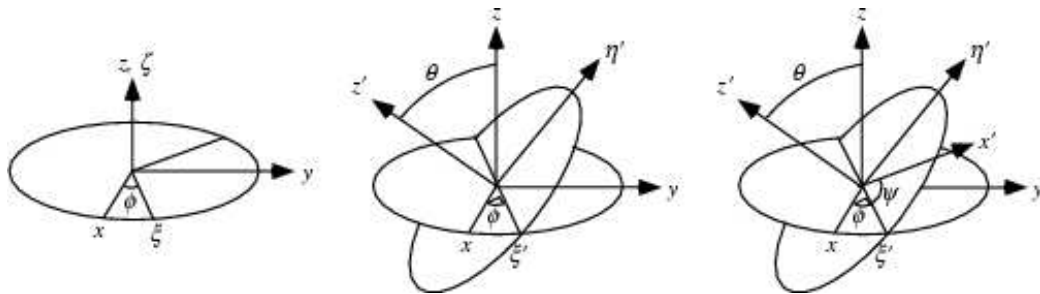
Abbildung B.1: Rotation around z-, x-, and again z-axis with the Euler angles.

The so-called "x-conventionïllustrated above is the most common definition. In this convention the rotation is given by Euler angles, where the first counterclockwise rotation is given by an angle about the z-axis, the second is again a counterclockwise rotation by an angle about the x-axis, and the third is also in counterclockwise direction by an angle about the z-axis, [127].

The convention used to derive the Euler angles in this work is by taking all the rotations of the axes in the clockwise direction. Doing this the following *rotation matrices* are found

$$
\mathcal{R}_{x,\theta} \;=\; \begin{pmatrix} 1 & 0 & 0 \\ 0 & \cos\theta & -\sin\theta \\ 0 & \sin\theta & \cos\theta \end{pmatrix} \;,
$$

$$
\mathcal{R}_{y,\psi} \;=\; \begin{pmatrix} \cos\psi & 0 & \sin\psi \\ 0 & 1 & 0 \\ -\sin\psi & 0 & \cos\psi \end{pmatrix} \;,
$$

$$\mathcal{R}_{z,\varphi} \;=\; \begin{pmatrix} \cos\varphi & -\sin\varphi & 0 \\ \sin\varphi & \cos\varphi & 0 \\ 0 & 0 & 1 \end{pmatrix} \;.$$

Coordinate Systems

The mostly used coordinate systems for reconstruction of the shower axis are the *ground system*, the *telescope system*, the *camera system*, *tilted systems*, the *nominal system*, and the *horizon system*. The transformation routines are set up within the software of the H.E.S.S. experiment. A summary about these coordinate systems and the basic transformations is given in this Section. A detailed description of them can be found in [70].

For all of the following explanations it is assumed that all telescopes of the array are directed to the same position in the sky (i.e. telescope axes are parallel), and that the center of the camera overlaps with the center of telescope's dish.

- **Ground System:** The ground system is a 3-dimensional system (Figure B.2). The center of this system is the center of the array. The positive x-axis is directed towards the geographical north, and the y-axis goes to geographical west, and the z-axis points towards the zenith, where the the axes measure distances. The precise position of a telescope in the ground system is measured from the center of the array to the center of the telescope dish.

- **Camera System and Telescope System:** The telescope system and the camera system are two dimensional systems (Figure B.2). The center of both of these systems are at the center of the camera. When the telescope is directed towards the zenith, the x- and y-axis of the telescope system are directed towards the geographical north and west, respectively. The telescope system represents a telescope with a focal length of 1 meters, and its axes describe any position (in units of meters) on the focal plane of this telescope.

  The orientation of the camera system is given by an angle of ρ with respect to the telescope system. Any position in the camera system can be found by scaling up the telescope coordinates by an amount of focal length of the telescope (15 meters).

  Every pixel in the camera has a certain coordinate in the camera system. If the location of a pixel in camera system coordinates is given by
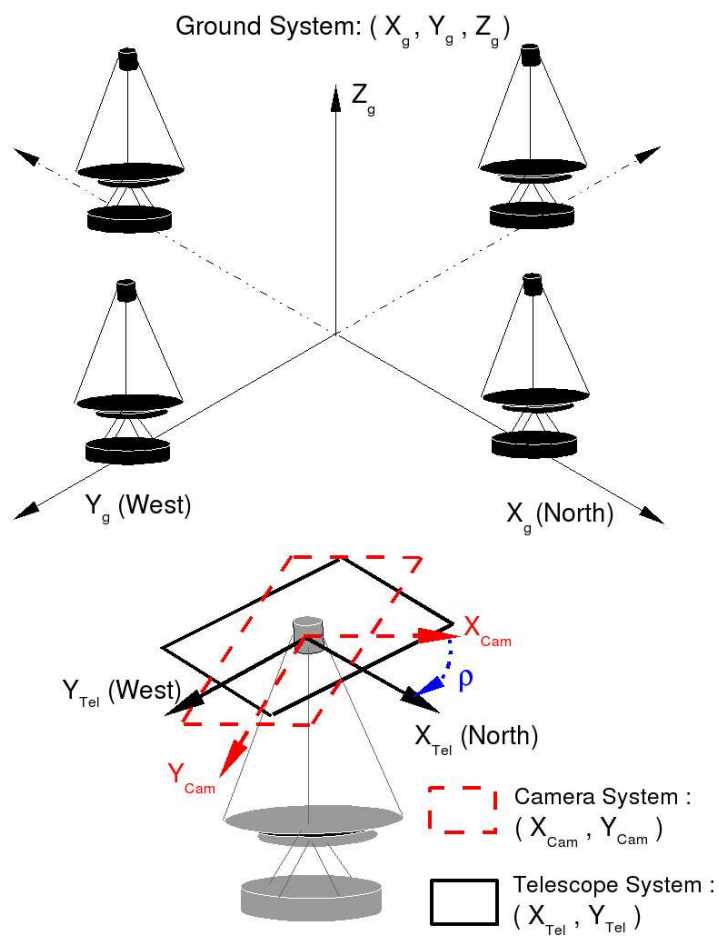
Abbildung B.2: Ground, Camera, and Telescope Systems.

a vector $\vec{c}$ and in telescope coordinates by a vector $\vec{t}$ after multiplying the focal length, F, by the telescope coordinates and rotating around the z-axis with the Euler rotation-matrix $\mathcal{R}_{z,\varphi}$ for $\varphi=\rho$ the camera coordinates can be formulated as follows

$$\vec{c} = \begin{pmatrix} X_{Cam} \\ Y_{Cam} \\ 0 \end{pmatrix} = F \, \mathcal{R}_{z,\varphi} \, \vec{t} \tag{B.1}$$

$$= F \begin{pmatrix} \cos\rho & -\sin\rho & 0 \\ \sin\rho & \cos\rho & 0 \\ 0 & 0 & 1 \end{pmatrix} \begin{pmatrix} X_{Tel} \\ Y_{Tel} \\ 0 \end{pmatrix} \; .$$

For each telescope in the telescope array, there exists a telescope system and a camera system.

- **Horizon System:** The pointing direction of a telescope is given by the two angles *altitude (Alt)* and *azimuth (Az)*. The horizon system gives the directions in spherical coordinates specified by the angles Alt and Az. The altitude angle is defined as 0° when the telescope points to the horizon. It runs from the horizon up to 90°, where it points to the *zenith*. The azimuth angle is measured as the angle in the sky from geographical north over east to south.

- **Tilted Telescope System and Tilted System:** The tilted telescope system is a 3-dimensional system. The center of this systems is at the center of the camera. Like in the telescope system, the x- and y-axis of the tilted telescope system are directed towards the geographical west and east, respectively, when the telescope is directed towards the zenith. The z-axis of the tilted telescope system shows the direction, where the telescope is pointing. So, projecting the tilted telescope system coordinates onto the focal plane with a focal length of 1 meter, the telescope system coordinates are obtained.

For an Alt-Az mounted telescope just two rotations are needed to describe the telescope's movement. So, there are only two independent axes of rotation (z-axis and y-axis (or x-axis)) as it is shown in Figure B.3 (top). If the telescope is pointing towards a direction in the sky with coordinates of (Alt,Az)=(β, λ), the normal vector (z-axis) of the tilted telescope system has a position $\vec{g}$ on the ground system (Figure B.4 (A)) as given below

$$\vec{g} = \begin{pmatrix} X_g \\ Y_g \\ Z_g \end{pmatrix} = \begin{pmatrix} \cos\lambda \, \cos\beta \\ \sin\lambda \, \cos\beta \\ \sin\beta \end{pmatrix} \; , \tag{B.2}$$

The position vector $\vec{g}$ specified in the ground system can be transfor-
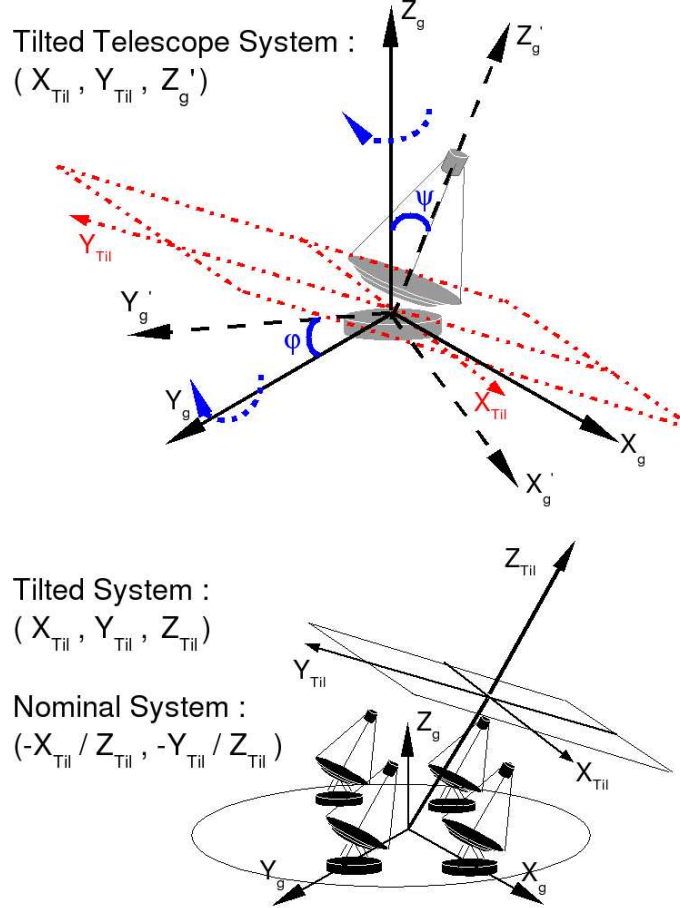
Abbildung B.3: Tilted Telescope System and Tilted System.

med into a pointing vector $\vec{t}$ in the tilted telescope system using the Euler rotation matrices $\mathcal{R}_{y,\psi}$, which is used for the rotation in the z-x plane around y-axis, and $\mathcal{R}_{z,\varphi}$, which is used for the rotation in the x-y plane around z-axis.

$$\vec{t} \; = \; \mathcal{R}_{y,\psi} \; \mathcal{R}_{z,\varphi} \; \vec{g} \;\; , \tag{B.3}$$

The angle ψ is equal to β for the case that the position vector $\vec{g}$ points into the x-y plane in the ground system. To get this vector to point out of the x-y plane ψ is equal to $-\beta - 180°$ (Figure B.4 (B)). Moreover, from Figure B.4 (B) the rotation angle φ is equal to $-\lambda$. So, the rotation

matrices for Equation B.3 are written as

$$\mathcal{R}_{y,\psi} = \begin{pmatrix} \sin\beta & 0 & -\cos\beta \\ 0 & 1 & 0 \\ \cos\beta & 0 & \sin\beta \end{pmatrix} \ ,$$

$$\mathcal{R}_{z,\varphi} = \begin{pmatrix} \cos\lambda & \sin\lambda & 0 \\ -\sin\lambda & \cos\lambda & 0 \\ 0 & 0 & 1 \end{pmatrix} \ .$$

The tilted system (Figure B.3 (bottom)) is a three dimensional system, and its center is at the center of the array. The only difference between the *tilted telescope system* and *tilted system* is that the z-axis of the tilted system is the nominal pointing axis of the array, whereas for the tilted telescope system it is the pointing axis of the specific telescope. So, there are totally four tilted telescope systems and one tilted system in the telescope array.

- **Nominal System:** The nominal system is a two dimensional system, and its center is the center of the camera. It is a projection of the tilted system on the focal plane for a focal length of 1 meters (i.e. the relation between the tilted system and the nominal system is analogue to that between the tilted telescope system and the telescope system). The coordinates defined in the tilted system given with $\vec{t}$, can be written in the nominal system as follows

$$\vec{n} = \begin{pmatrix} -X_{Til}/Z_{Til} \\ -Y_{Til}/Z_{Til} \\ 0 \end{pmatrix} \ , \qquad (B.4)$$

where the minus sign comes from the fact that the light is scattering on the mirrors of the telescope and changing its direction.

To get the pixel location in the nominal system, several transformations should be applied one after the other. The usual transformation chain from the camera system into the nominal system of the array are shown below

Camera System
↓
Tilted Telescope System
↓
Ground System
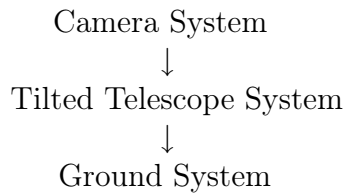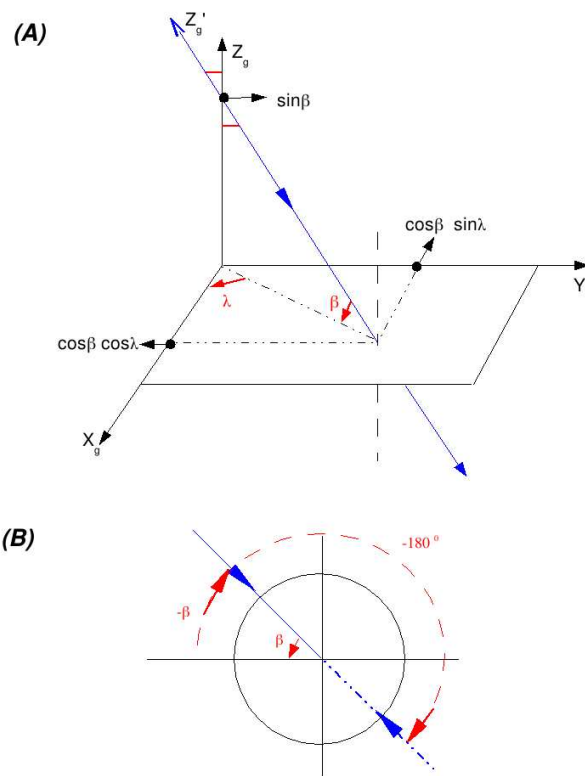
Abbildung B.4: (A) The position of the normal of the tilted telescope system given in the ground system, where the direction vector points into the x-y plane. (B) If the direction vector changes its direction 180°, the angle of rotation around y-axis equals to $-\beta - 180°$.

$$\downarrow$$
Tilted System
$$\downarrow$$
Nominal System
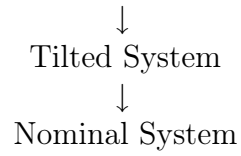
As a result, information about pixel amplitudes and the corresponding pixel positions in the camera system can be transformed into the nominal system, and the Hillas parameters can be calculated, which is done in the data calibration procedure. Furthermore, the shower direction is reconstructed in the nominal system. After shower direction is reconstructed in the nominal system, they can be transformed into the horizon system, and from the horizon system they can be transformed into any other coordinate systems like *Alt-Az system*, or *RA-Dec-J2000 system* etc.. More detailed information on astronomical terminology can be found in [105], and [70].

Transforming the telescopes' coordinates from the ground system into the tilted system, the shower core position is reconstructed in the tilted system. The reconstructed shower core position is then transformed from the tilted system back into the ground system.

Appendix C

Astronomical Time Systems

Since atomic clocks started to be used, accurate time measurements have been made it possible to control universal time related to Earth's rotation. *Coordianted universal time (UTC)* was adopted in 1972 and all currently time signals are synchronized with UTC, ([105]).

Calendars

Due to the variable length of years and months, it is difficult to calculate time diffferences. So, astronomers have employed various methods to give each day a running number. The most widely used numbers are the *Julian dates* ([105]). Given a date with years (Y), months (M), days (D), hours (H), minutes (M), and seconds (S), the julian date can be calculated as follows:

$$
\begin{aligned}
JD \quad &= \quad \frac{\left[1461 \cdot \left(Y \ + \ 4800 \ + \ \frac{M-14}{12}\right)\right]}{4} \\
&+ \ \frac{\left[367 \cdot \left(M - 2 \ - \ 12\frac{M-14}{12}\right)\right]}{12} \\
&- \ \frac{\left[3 \cdot \left(Y \ + \ 4900 \ + \ \frac{M-14}{12} \cdot \frac{1}{100}\right)\right]}{4} \\
&+ \ d \ - \ 32075 \ + \ \frac{H}{24} \ + \ \frac{M}{1440} \ + \ \frac{S}{86400} \quad .
\end{aligned}
$$

The conversion between JD and *modified Julien date (MJD)* is given as follows:

$$
MJD \quad = \ JD \ - \ 2400000.5 \quad .
$$

JD starts the next day at 12:00 UTC, MJD starts it at 24:00 UTC.

Literaturverzeichnis

[1] F. A. Aharonian and A. M. Atoyan. *Astroparticle Physics*, 3:275, 1995.

[2] F. A. Aharonian and A. M. Atoyan. *Monthly Notices of the Royal Astronomical Society*, 278:525, 1996.

[3] F. A. Aharonian and A. M. Atoyan. *astro-ph/9803091*, 1998.

[4] F. A. Aharonian et al. H.e.s.s. letter of intent. http://www.mpi-hd.mpg.de/hfm/HESS/public/hessloi3.ps.gz, 1997.

[5] F. A. Aharonian et al. *Astrophysical Journal*, 539:317–324, 2000.

[6] F. A. Aharonian et al. *Astronomy & Astrophysics*, 370:112, 2001.

[7] F. A. Aharonian et al. *Astronomy & Astrophysics*, 373:293–300, 2001.

[8] F. A. Aharonian et al. *Astronomy & Astrophysics*, 417:973–979, 2004.

[9] F. A. Aharonian et al. *Astrophysical Journal*, 614(2):897, 2004.

[10] F. A. Aharonian and A. Konopelko. Towards the major atmospheric cherenkov detector v. In *TeV Gamma-ray Astrophysics Workshop*, page 329, Kruger Park, South Africa, 1997.

[11] M. Amenomori et al. *Astrophysical Journal*, 525:L93–L96, 1999.

[12] P. Armstrong et al. *Experimental Astronomy*, 9:51–80, 1999.

[13] P. Auger. *Reviews of Modern Physics*, 11:288, 1939.

[14] M. Aye et al. In *28th International Cosmic Ray Conference*, page 2975, Tsukuba, Japan, 2003. Univ. Academy Press Tokyo.

[15] G. Barbiellini et al. Gamma2001: Gamma-ray astrophysics. In *AIP Conference*, volume 587, page 774, 2001.

[16] A. Barrau. PhD thesis, 1998. In the CAT Experiment.

[17] J. A. Barrio. The magic telescope, design study, 1998. MPI-PhE 98-5.

[18] M. C. Begelman, R. D. Blandford, and M. J. Rees. *Reviews of Modern Physics*, 56:255, 1984.

[19] M. Beilicke. Investigation of the psrb1259-63 field of view h.e.s.s. In *International Symposium on High Energy Gamma-Ray Astronomy*, Heidelberg, Germany, 2004.

[20] A. R. Bell. *Monthly Notices of the Royal Astronomical Society*, 182:147, 1978.

[21] D. Berge. Master's thesis, Humboldt Universität zur Berlin, 2002. Diplom in the H.E.S.S. Experiment.

[22] K. Bernlöhr. URL `http://www.mpi$-$hd.mpg.de/hfm/$\sim$bernlor/HESS`.

[23] K. Bernlöhr. Corsika and sim_telarray - simulation of the imaging atmospheric cherenkov technique for the h.e.s.s. experiment, 2002. H.E.S.S. internal note 2, 4.

[24] K. Bernlöhr. Simulation of the imaging atmospheric cherenkov technique for the h.e.s.s. experiment, 2002. H.E.S.S. internal note 3, 1.

[25] K. Bernlör. *Space Science Review*, 75:185, 1996.

[26] K. Bernlör. *Astroparticle Physics*, 20:111–128, 2003.

[27] G. F. Bignami et al. *Space Science Instr.*, 1:245, 1975.

[28] D. J. Bird et al. *Astrophysical Journal*, 441:114, 1995.

[29] R. D. Blanford and J. D. Ostriker. *Astrophysical Journal*, 221:L29, 1978.

[30] J. Bolton, G. Stanley, and O. Slee. *Nature*, 164:101, 1949.

[31] O. Bolz. Master's thesis, MPI-Heidelberg, 1999. Diplom in the HEGRA Experiment.

[32] O. Bolz. PhD thesis, MPI-Heidelberg, 2004. In the H.E.S.S. Experiment.

[33] C. Borgmeier et al. In *27th International Cosmic Ray Conference*, pages 2896–2899, Hamburg, Germany, 2001.

[34] C. Borgmeier et al. In *28th International Cosmic Ray Conference*, page 2891, Tsukuba, Japan, 2003. Univ. Academy Press Tokyo.

[35] W. Bothe and Kohlhörster, W. *Zeitschrift für Physik*, 56:751, 1929.

[36] C. C. G. Bowden et al. In *23th International Cosmic Ray Conference*, volume 1, page 294, Calgary, 1993.

[37] S. M. Bradbury. In *26th International Cosmic Ray Conference*, volume 5, page 280, Salt Lake City, USA, 1999.

[38] R. Browning, D. Ramsden, and P.J. Wright. *Nature Physical Science*, 232:99, 1971.

[39] A. Buckley et al. *Astronomy & Astrophysics*, 329:639, 1998.

[40] M. F. Cawley. In *18th International Cosmic Ray Conference*, page 118, Bangalore, India, 1983.

[41] P. M. Chadwick et al. In *25th International Cosmic Ray Conference*, volume 3, page 189, Durban, 1997.

[42] P. M. Chadwick et al. In *Workshop on GeV-TeV Gamma-Ray Astrophysics*, volume 512, pages 210–214, Snowbird, USA, 2000.

[43] Cheng, Ho, and M. A. Ruderman. *Astrophysical Journal*, 300:500, 1986.

[44] Cheng, Ho, and M. A. Ruderman. *Astrophysical Journal*, 300:522, 1986.

[45] J. Chiang and R. W. Romani. *Astrophysical Journal*, 436:754, 1994.

[46] G. Cocconi. In *International Cosmic Ray Conference*, volume 2, page 309, Moscow, Russia, 1959.

[47] AGASA Collaboration. In *26th International Cosmic Ray Conference*, volume 3, page 252, Salt Lake City, USA, 1999.

[48] H.E.S.S. collaboration (F. A. Aharonian et al.). *Nature*, 432:75, 2004.

[49] H.E.S.S. collaboration (F. A. Aharonian et al.). *Astronomy & Astrophysics*, 430:865–875, 2005.

[50] R. Cornils et al. In *28th International Cosmic Ray Conference*, pages 2875–2878, Tsukuba, Japan, 2003. Univ. Academy Press Tokyo.

[51] R. Cornils et al. *Astroparticle Physics*, 20:129–143, 2003.

[52] A. Daum et al. *Astroparticle Physics*, 8:1, 1997.

[53] J. Davies and E. Cotton. *Solar Energy*, 1:16, 1957.

[54] O. C. de Jager et al. *Astrophysical Journal*, 457:L203, 1996.

[55] O. C. de Jager et al. *Astrophysical Journal*, 457:253, 1996.

[56] O. C. de Jager and A. K. Harding. *Astrophysical Journal*, 396:161, 1992.

[57] M. de Naurois et al. *Astrophysical Journal*, 566:343, 2002.

[58] S. M. Derdeyn et al. *NIM*, 98:557, 1972.

[59] A. Djannati-Atai. In *28th International Cosmic Ray Conference*, page 2575, Tsukuba, Japan, 2003. Univ. Academy Press Tokyo.

[60] P. Doll, J. Engler, P. Gabriel, et al. *Nuclear Physics B*, 14:336, 1990.

[61] L. O'C. Drury, F. A. Aharonian, and Völk, H. J. *Astronomy & Astrophysics*, 287:959, 1994.

[62] R. Enomoto et al. *Nature*, 416:823, 2002.

[63] S. Fegan. *astro-ph/0102324*, 2001.

[64] J. M. Fierro, P. F. Michaelson, P. L. Nolan, and D. C. Thompson. *Astrophysical Journal*, 494:734, 1998.

[65] S. Funk et al. *Astroparticle Physics*, 22/3-4:285–296, 2004.

[66] T. Gaisser. *Cosmic Rays and Particle Physics*. Cambridge University Press, 1990.

[67] N. Gehrels and P. Michelson. *Astroparticle Physics*, 11:277, 1999.

[68] N. Gehrels and the GLAST Collaboration. In *AIP Conference: High Energy Gamma Ray Astronomy*, volume 220, page 3, 2001.

[69] S. Gillessen. In *28th International Cosmic Ray Conference*, pages 2899–2902, Tsukuba, Japan, 2003. Univ. Academy Press Tokyo.

[70] S. Gillessen. PhD thesis, MPI-Heidelberg, 2004. In the H.E.S.S. Experiment.

[71] V. L. Ginzburg and S. I. Syrovatskii. *The Origin of Cosmic Rays.* Pergamon Press, Oxford, 1964.

[72] T. Gold. *Nature*, 221:25, 1969.

[73] P. Goldreich and W. H. Julian. *Astrophysical Journal*, 157:869, 1969.

[74] P. Goret et al. In *26th International Cosmic Ray Conference*, volume 3, page 496, Salt Lake City, USA, 1999.

[75] R. J. Gould. *Physical Review Letters*, 15:557, 1965.

[76] K. Greisen, 1956. Prog. Cosmic Ray Physics 02/04.

[77] P. K. F. Grieder. *Cosmic Rays at Earth.* Elsevier Science B.V., 1st edition, 2001.

[78] D. E. Groom et al. *The European Physical Journal*, C15:1, 2000.

[79] T. Hara et al. *NIM A*, 332:300, 1993.

[80] R. C. Hartman et al. *Astrophysical Journal S.*, 123:79, 1999.

[81] R. C. Hartman et al. The third egret catalog of high-energy gamma-ray sources. *Astrophysical Journal S.*, 1999.

[82] S. Hayakawa. *Prog. Theoretical Physics*, 8:571, 1952.

[83] D. Heck et al. URL `http://www-ik.fzk.de/~heck/corsika`.

[84] D. Heck, J. Knapp, J. Capdevielle, et al. Corsika: A monte carlo code to simulate extensive air showers, thech. report,forschungszentrum, wissenschaftliche berichte, 1998. FZKA 6019.

[85] W. Heitler. *Quantum Theory of Radiation.* Oxford University Press, 1954.

[86] V. Hess. *Physikalische Zeitschrift*, 13:1084, 1912.

[87] H.E.S.S. collaboration (F. A. Aharonian et al.). *Astronomy & Astrophysics*, 425:L13–L17, 2004.

[88] H.E.S.S. collaboration (F. A. Aharonian et al.). *Astroparticle Physics*, 22(2):109–125, 2004.

[89] A. Hewish, S. J. Bell, J. D. Pilkington, P. F. Scott, and R. A. Collins. *Nature*, 217:709, 1968.

[90] D. Hill and N. Porter. *Nature*, 191:690, 1961.

[91] A. M. Hillas. In *19th International Cosmic Ray Conference*, volume 3, page 445, La Jolla, 1985.

[92] A. M. Hillas et al. *Astrophysical Journal*, 503:744, 1998.

[93] Hipparcos. Space astronomy mission. URL `http://astro.estec.esa.nl/Hipparcos/`.

[94] C. M. Hoffman, I. Jung, A. Konopelko, H. Krawczynski, H. Lampeitl, and Pöhlhofer. *Astroparticle Physics*, 12:135, 1999.

[95] C. M. Hoffman, C. Sinnis, P. Fleury, and M. Punch. *Rev. Mod. Phys.*, 71:897–936, 1999.

[96] W. Hofmann. In *Workshop: TeV γ-ray Astrophysics*, page 405, Kruger Park, 1997.

[97] W. Hofmann. In *28th International Cosmic Ray Conference*, pages 2811–2814, Tsukuba, Japan, 2003. Univ. Academy Press Tokyo.

[98] W. Hofmann, H. Lampeitl, A. Konopelko, and H. Krawczynski. *Astroparticle Physics*, 12:207–216, 2000.

[99] J. D. Jackson. *Classical Electrodynamics*. John Wiley and Sons, New York, 1975.

[100] W. S. Johns et al. In *Workshop: Imaging in High-energy Astronomy*, page 329, Anacapri, 1993.

[101] I. Jung. PhD thesis, MPI-Heidelberg, 2003. In the H.E.S.S. Experiment.

[102] C. Köhler. PhD thesis, MPI-Heidelberg, 1998. In the HEGRA Experiment.

[103] G. Kanbach. *astro-ph/0209021*, 2002.

[104] G. Kanbach et al. *Space Sci. Rev.*, 49:69, 1988.

[105] H. Karttunen, P. Kröger, H. Oja, M. Poutanen, and J. K. Donner. *Fundamental Astronomy*. Springer-Verlag Berlin, Heidelberg, 1987.

[106] C. F. Kennel and F. V. Coroniti. *Astrophysical Journal*, 283:710, 1984.

[107] C. F. Kennel and F. V. Coroniti. *Astrophysical Journal*, 283:694, 1984.

[108] M. Kertzman and G. Sembroski. *NIM A*, 343:629, 1994.

[109] T. Kifune et al. *Astrophysical Journal*, 438:L91, 1995.

[110] J. Kildea. PhD thesis, University College Dublin, 2002. In the Whipple Experiment.

[111] A. Konopelko et al. *Astrophysical Journal*, 10:275, 1999.

[112] A. Konopelko, F. Lucarelli, H. Lampeitl, and W. Hofmann. *Nucl. Part. Phys.*, 28:2755, 2002.

[113] N. Leroy. Using muons for calibration of the h.e.s.s. telescopes., 2002. H.E.S.S. internal note 02/20.

[114] N. Leroy et al. In *28th International Cosmic Ray Conference*, page 2895, Tsukuba, Japan, 2003. Univ. Academy Press Tokyo.

[115] R. W. Lessard et al. In *26th International Cosmic Ray Conference*, volume 3, page 488, Salt Lake City, USA, 1999.

[116] R. W. Lessard et al. *Astrophysical Journal*, 531:942, 2000.

[117] D. Lewis. volume 1. 1990.

[118] TP. Li and YQ. Ma. volume 272. 1983.

[119] M. Longair. *High Energy Astrophysics, Vol. 1*. Cambridge University Press, 1992.

[120] M. Longair. *High Energy Astrophysics, Vol. 2*. Cambridge University Press, 1992.

[121] G. A. Lyne and F. Graham-Smith. *Cambridge Astrophysics Series 31: Pulsar Astronomy*. Cambridge University Press, 1998.

[122] K. Mannheim. *Astronomy & Astrophysics*, 269:67, 1993.

[123] L. Maraschi, G. Ghisellini, and A. Celotti. *Astrophysical Journal*, 397:L5, 1992.

[124] C. Masterson, 2003. private communications.

[125] C. Masterson et al. In *28th International Cosmic Ray Conference*, Tsukuba, Japan, 2003. Univ. Academy Press Tokyo.

[126] C. Masterson et al. In *AIP Conference: Gamma 2004*, volume 745, page 617, Heidelberg, Germany, 2004.

[127] MathWorld. Euler angles. URL `http://mathworld.wolfram.com/EulerAngles.html`.

[128] J. A. Miller. *Geophys. Rev.*, 102:A7, 14631, 1997.

[129] P. Morris. *Nuovo Cimento*, 7:858, 1958.

[130] H. Muraishi et al. *Astronomy & Astrophysics*, 354:L57, 2000.

[131] M. Nagano and A. A. Watson. *Modern Physics*, 72:689, 2000.

[132] OmniORB. URL `http://omniorb.sourceforge.net`.

[133] R. A. Ong. The status of vhe astronomy. *astro-ph/0304336*, 1998.

[134] S. Oser et al. *Astrophysical Journal*, 547:949, 2001.

[135] J. P. Ostriker and J. E. Gunn. *Astrophysical Journal*, 547:1395, 1969.

[136] W. S. Paciesas et al. *Astrophysical Journal S.S.*, 122:465, 1999.

[137] F. Pacini. *Nature*, 216:567, 1967.

[138] E. Pare. *NIM*, A490:71–89, 2002.

[139] C. Prosch et al. *Astronomy & Astrophysics*, 314:275, 1996.

[140] R. J. Protheroe, A. Mastichiadis, and C. D. Dermer. *Astroparticle Physics*, 1:113, 1992.

[141] H.-J. Röser and K. Meisenheimer, editors. *Jets in Extragalactic Radio Sources*, page 534. Springer, New York, 1991.

[142] M. J. Rees and J. E. Gunn. *Monthly Notices of the Royal Astronomical Society*, 167:1, 1974.

[143] O. Reimer and M. Pohl. *Astronomy & Astrophysics*, 390:L43, 2002.

[144] R. W. Romani. *Astrophysical Journal*, 470:469, 1996.

[145] Root. Analysis package. URL `http://root.cern.ch`.

[146] G. P. Rowell. *astro-ph/0310025*, 2003.

[147] M. A. Ruderman and P. G. Sutherland. *Astrophysical Journal*, 196:51, 1975.

[148] V. Schönefelder, editor. *The Universe in Gamma Rays*, page 27. Springer-Verlag Berlin, Heidelberg, 2001.

[149] V. Schönefelder, editor. *The Universe in Gamma Rays*, page 185. Springer-Verlag Berlin, Heidelberg, 2001.

[150] V. Schönefelder et al. *Astrophysical Journal S.S.*, 86:657, 1993.

[151] S. Schlenker. Master's thesis, Humboldt Universität zur Berlin, 2001. Diplom in the H.E.S.S. Experiment.

[152] S. Schlenker. Discovery of the binary pulsar psrb1259-63 in vhe gamma rays with h.e.s.s. In *International Symposium on High Energy Gamma-Ray Astronomy*, Heidelberg, Germany, 2004.

[153] U. Schwanke. Usage of importance sampling methods for efficient monte carlo simulation of sohwer core distances., 2004. H.E.S.S. internal note.

[154] I. S. Shklovsky. *Dok. Akad. Nauk USSR [Sov. Phys. Dokl.]*, 90:983, 1953.

[155] STACEE. URL `http://www.astro.ucla.edu/~stacee`.

[156] D. H. Staelin and E. C. Reifenstein. *Science*, 162:1481, 1968.

[157] P. A. Sturrock. *Astrophysical Journal*, 164:529, 1971.

[158] T. Tanimori et al. *Astrophysical Journal*, 497:L25, 1998.

[159] T. Tanimori et al. *Astrophysical Journal*, 492:L33, 1998.

[160] D. J. Thompson et al. *Astrophysical Journal S.S.*, 101:259, 1995.

[161] M. Tluczykont. PhD thesis, MPI-Heidelberg, 2003. In the HEGRA Experiment.

[162] M. Ulrich. PhD thesis, MPI-Heidelberg, 1996. In the HEGRA Experiment.

[163] C. M. Urry and P. Padovani. *PASP*, 107:805, 1995.

[164] P. Vincent et al. In *28th International Cosmic Ray Conference*, page 2887, Tsukuba, Japan, 2003. Univ. Academy Press Tokyo.

[165] T. Weekes and K. Turver. In *12th Eslab Symposium*, volume ESA SP-124, page 279, Frascati, Italy, 1977.

[166] T. C. Weekes. In *17th International Cosmic Ray Conference*, volume 8, page 34, Paris, France, 1981.

[167] T. C. Weekes. *Very High Energy Astronomy*. IoP Publishing, 2003.

[168] T. C. Weekes et al. *Astrophysical Journal*, 342:379, 1989.

[169] T. C. Weekes et al. In *25th International Cosmic Ray Conference*, volume 5, page 173, Durban, 1997.

[170] B. Wiebel et al. Chemical composition in high energy cosmic rays, 1994. preprint WUB.

[171] B. Wiebel-Sooth et al. *astro-ph/9709253*, 1997.

[172] D. A. Williams. Astrophysics around 100 gev with stacee. In *2nd VERITAS Symposium on TeV Astrophysics*, Chicago, USA, 2003.

[173] T. Yoshikoshi et al. *Astrophysical Journal*, 487:L65, 1997.

Acknowledgements / Danksagungen

I would like express my gratitude to my mother and father because of their endless love, support, and trust on me. Especially to my mother for encouraging me to study the laws of nature. I thank to my sister Emel for her support and care throughout my work.

I thank to Dr. Kristal Mauritz, whose enthusiastic introduction to the H.E.S.S. project in year 2001, helped me to quickly make up my mind to work in this project.

I thank to Prof. Thomas Lohse for accepting me as a member of H.E.S.S. Berlin group, which gave me the opportunity to do research on this very interesting field, and supporting me financially through the fellowship of "Graduate College for High Energy Physics of Humboldt University of Berlin". I take this opportunity to thank to the committee of "Graduate College for High Energy Physics of Humboldt University of Berlinfor providing me this scholarship for 3 years.

I thank Dr. Konrad Bernlör for his explanations on the shower reconstruction algorithms used in the HEGRA experiment and helpful suggestions and explanations on Monte Carlo simulation algorithms. I also thank Dr. Stefan Gillesen for giving me a hand on implementing the coordinate systems into the shower reconstruction algorithms.

I thank to my dear office-mate Frank Breitling. I appreciated his help and practical suggestions especially on computers and programming. I thank him for readiness to help.

I am thankful to Dr. Conor Masterson, who gave me the opportunity to stay one month at Heidelberg Max-Planck Institut für Kernphysik to work with him and Dr. Wystan Benbow. I appreciated their guidance and help throughout my analysis on the Crab Nebula.

I would like to express my sincere gratitude to Dr. Alexander Konopelko. I benefited a lot from his expertise and guidance in most of the stages of my work. Discussions with him helped me especially to understand various

aspects of γ-ray astronomy in detail. I also thank him for taking time to read and revise my thesis and giving me very useful suggestions about it.

I would like to thank Dr. Conor Masterson, Dr. Ulli Schwanke reading parts of my thesis and giving me possibility to improve it further with their suggestions.

I thank to my flat mates in Siegmunds Hof, Haus-11, 1st Floor (SiHo) for their support, especially in my very stressing days by being ready to listen and talk or just by being there. Anna, Alvaro, Christoph, Fatma, Greg, Javet, Johanna, Juliane, Marta, Sabri, Ting and all other friends that I know through SiHo connection.

I am also thankful to all Berlin group members for the technical support and alternating subjects on computers, programming, and everyday life in our coffee breaks.

I also thank to all other friends that I met though working in this field, whose good wishes helped me enormously to accomplish this work.

Vita

Name:	**Tülün Ergin**
Date of Birth:	29th April 1975
Place of Birth:	Wuppertal, Germany

University Education:

2005, Ph.D.	High Energy Astrophysics (Gamma-Ray Astronomy) Physics Department Humboldt University of Berlin, Berlin/Germany (Summer 2001 - Spring 2005) *(Supervisor: Prof. Dr. T. Lohse)*
2001, Graduate Studies	High Energy Experimental Physics Physics Department Middle East Technical University, Ankara/Turkey (Autumn 2000 - January 2001) *(Supervisor: Prof. Dr. P. Tolun)*
2000, M.Sc.	High Energy Experimental Physics Physics Department Middle East Technical University (Autumn 1997 - Summer 2000) *(Supervisor: Prof. Dr. P. Tolun)*
1997, B.Sc. (Major)	Physics Department Middle East Technical University, Ankara/Turkey (Autumn 1993 - Spring 1997)
1997, B.Sc. (Minor)	Biology Department

162

Middle East Technical University, Ankara/Turkey
(Autumn 1994 - Spring 1997)

Publications:

- *Calibration of Cameras of the H.E.S.S. Detector*
  H.E.S.S. collaboration, Aharonian, F.A. et al.
  Astroparticle Physics Vol. 22/2, 109-125 (2004)

- *Very high energy gamma rays from the direction of Sagittarius A**
  H.E.S.S. collaboration, Aharonian, F.A. et al.
  Astronomy & Astrophysics Vol. 425, L13-L17 (2004)

- *High-energy particle acceleration in the shell of a supernova remnant*
  H.E.S.S. collaboration, Aharonian, F.A. et al.
  Nature 432, 75-77 (2004)

- *H.E.S.S. Observations of PKS2155-304*
  H.E.S.S. collaboration, Aharonian, F.A. et al.
  Astronomy & Astrophysics, Vol. 430, 865-875 (2005)

- *Very high energy gamma rays from the composite SNR G0.9+0.1*
  H.E.S.S. collaboration, Aharonian, F.A. et al.
  Astronomy & Astrophysics, Vol. 432, L25-L29 (2005)

- *Search for TeV emission from the region around PSR B1706-44 with the*
  H.E.S.S. experiment
  H.E.S.S. collaboration, Aharonian, F.A. et al.
  Astronomy & Astrophysics, Vol. 432, L9-L12 (2005)

- *A new population of very high energy gamma-ray sources in the Milky Way*
  H.E.S.S. collaboration, Aharonian, F.A. et al.
  Science 307, 1938-1942 (2005)

References:

- Prof. Dr. Thomas Lohse

  Humboldt University of Berlin

Department of Physics

Experimental Elementary Particle Physics

Newton str. 15, Raum:2'416

D−12489 Berlin, Germany

e-mail: lohse@ifh.de

tel: (49) 30 2093 7820

fax: (49) 30 2093 7642

- Prof. Dr. Nicolaj Pavel

  Humboldt University of Berlin

  Department of Physics

  Experimental Elementary Particle Physics

  Newton str. 15, Raum:2'414

  D-12489 Berlin, Germany

  e-mail: pavel@physik.hu-berlin.de

  tel: (49) 30 2093 7817

  fax: (49) 30 2093 7642

- Prof. Dr. Stefan Wagner

  Landessternwarte Heidelberg-Koenigstuhl

  D-69117 Heidelberg, Germany

  e-mail: S.Wagner@lsw.uni-heidelberg.de

  tel: (49) 6221 509 212

  fax: (49) 6221 509 202

Erklärung

Ich erkläre, dass ich diese Arbeit selbständig angefertigt und keine weitere als die angegebene Literatur verwendet habe.

Mit der Auslage dieser Arbeit in der Bibliothek der Humboldt-Universität zu Berlin bin ich einverstanden.

Berlin, den 15. November 2004   Tülün Ergin